Technische Universität München

Fakultät für Medizin

TLM

Whole body optoacoustic tomography for high resolution functional and molecular imaging in mice

Avihai Ron

Vollständiger Abdruck der von der Fakultät für Medizin der Technischen Universität München zur Erlangung des akademischen Grades eines

Doktors der Naturwissenschaften (Dr. rer. nat.)

genehmigten Dissertation.

Vorsitzende: Prof. Dr. Gabriele Multhoff

Prüfer der Dissertation: Prof. Dr. Susanne Kossatz

Prof. Dr. Bernd Reif

Die Dissertation wurde am 09.06.2020 bei der Technischen Universität München eingereicht und durch die Fakultät für Medizin am 29.12.2020 angenommen

Munich, May 23, 2020   Avihai Ron

Abstract

Murine models have long been used to study human biology and disease and have become instrumental to understand pathophysiological changes involved at the molecular and cellular levels. Minimally invasive technologies are required to efficiently follow longitudinal biological processes within live animals. Particularly, the adaptation (downscaling) of established imaging technologies for the purpose of small-animal imaging has been the focus of many research efforts. In addition, new types of optical imaging techniques were developed to provide superior functional and molecular contrast at the expense of poor resolution. Optoacoustics tomography (OAT) has also emerged as a molecular imaging technology synergistically combining rich optical contrast with a high ultrasonic resolution and is gaining maturity as a preclinical research tool. Its molecular sensitivity is derived from the distinctive light absorption profiles of different substances. These unique characteristics foster OAT as a promising technology for molecular and functional imaging and motivate the development of new OAT techniques for preclinical settings. Most OAT systems produce 2D cross-sectional images with either linear or curved ultrasound arrays. Such acquisition geometries lack the capability to provide accurate volumetric images, which is essential for whole-body visualization and accurate quantification of biological parameters. In this thesis, we designed and developed a new small-animal OAT scanning approach, named flash scanning OA tomography (FlashOT), based on a spherical ultrasonic transducer array that is capable of imaging fast dynamic processes at the whole-body scale.

FlashOT grants high-throughput imaging capacity, which is essential for studying the kinetics and biodistribution of contrast agents at the whole-body level. For this, we designed a new scanning scheme based on continuous scanning at high velocity (up to 80 mm/sec) and position monitoring of the array. The new system grants whole-body imaging under 1 minute, which was exploited to demonstrate the feasibility of the system to track fast distribution of nanoparticles in multiple organs. We additionally designed a dedicated motion rejection algorithm based on frame clustering that can be readily implemented during the image acquisition process, thus averting heavy computational demands of 3D rendering.

The developed imaging system was exploited in this thesis for several biological applications. Volumetric rendering of large regions was exploited for improved segmentation and quantification. This led to accurate quantification of hemodynamic parameters at the whole organ level, which is not possible by 2D analyses of cross-sectional images. We performed imaging of brown adipose tissue of diabetic mice to demonstrate the capacity of the OAT system for accurate delineation and improved quantification of vessel density and tissue metabolism over the entire tissue. The developed OAT approach was shown to further facilitate functional and dynamic imaging by capitalizing on high frame rate acquisition. Here, we utilized a high-resolution (100 µm) spherical transducer to capture dynamic processes in tumors at 100 frames per second. Subsequently, frequency analysis of local blood oxygen saturation (sO2) trends enabled identifying, for the first time with OAT, periodical variations of sO2 level (also known as cyclic hypoxia) in distinct regions of tumors.

All in all, we introduce a small-animal OAT scanner that promotes a unique spatio-temporal resolution for molecular and functional imaging. Its volumetric nature permits panoramic visualization and accurate quantification of molecular contrast. Furthermore, its capacity to capture a whole organ or rapidly scan the entire body grants functional imaging of multiscale dynamic processes.

Zusammenfassung

Maus Modelle werden seit langem zur Untersuchung der menschlichen Biologie und Krankheiten eingesetzt und sind entscheidend für das Verständnis pathophysiologischer Veränderungen auf molekularer und zellulärer Ebene. Es sind jedoch minimal-invasive Technologien erforderlich, um biologische Längsschnitte innerhalb lebender Tiere effizient zu verfolgen. Daher stand die Miniaturisierung etablierter Bildgebungstechnologien zum Zweck der Bildgebung bei Kleintieren im Mittelpunkt vieler Forschungsanstrengungen. Darüber hinaus wurden neuartige optische Techniken weiterentwickelt, um einen funktionellen und molekularen Kontrast zu erzielen, trotz der schlechten Tiefenauflösung. Die Optoakustik-Tomographie (OAT) ist eine ausgereifte molekulare Bildgebungstechnologie, die einen hohen optischen Kontrast mit einer hohen Ultraschallauflösung kombiniert. Ihre molekulare Empfindlichkeit ergibt sich aus den ausgeprägten Lichtabsorptionsprofilen der verschiedenen Substanzen. Diese Eigenschaften machen die OAT zu einer vielversprechenden Technologie für die molekulare und funktionelle Bildgebung und fördern die Entwicklung neuer OAT-Techniken für präklinische Bereiche. Bislang wird bei den meisten OATs einringförmigerUltraschallwandlerarray verwendet, der 2D-Schnittbilder erzeugt. Einer solchen Geometrie fehlt aber die volumetrische Eigenschaft, die für die Ganzkörper-Visualisierungen und die genaue Quantifizierung biologischer Parameter unerlässlich ist. In dieser Arbeit entwerfen wir einen OAT-Scanner für Kleintiere, der auf einem sphärischen Ultraschallwandlerarray basiert und 3D-Bilder in verschiedenen Maßstäben und räumlich-zeitlichen Auflösungen erzeugen kann. Anschließend setzen wir spezialisierte Analysen und Algorithmen ein, um eine qualitativ hochwertige Visualisierung und Quantifizierung für verschiedene biologische Anwendungen zu erhalten.

Standardmethoden zur Segmentierung und Analyse von 2D-Schnitten können die genaue Quantifizierung hämodynamischer Parameter im Zielgewebe erschweren. Hier wird die volumetrische Darstellung großer Regionen für die Untersuchung solcher Parameter im braunen Fettgewebe diabetischer Mäuse genutzt. Folglich erleichtert sie die genaue Abgrenzung und verbesserte Quantifizierung der Gefäßdichte und des Gewebestoffwechsels über das gesamte Organ. Eine weitere große Herausforderung der in-vivo-Bildgebung ist die Unterdrückung von Bewegungsartefakten, die die Bildqualität beeinträchtigen und eine genaue Quantifizierung

erschweren. Im Falle der volumetrischen Bildgebung sind die bestehenden Lösungen ineffizient und führen zu einer übermäßigen Datenerfassung und langen Nachbearbeitungszeiten. Um diese Problematik zu umgehen entwickeln wir einen speziellen Bewegungsunterdrückungs-Algorithmus, der auf Frame-Clustering basiert und der bereits während des Bildaufnahmeprozesses implementiert werden kann, wodurch hohe Rechenanforderungen vermieden werden können.

Zusätzlich zur "statischen" Bildgebung kann OAT auch die funktionelle und dynamische Bildgebung erleichtern, indem es sich die hohe Bildfrequenz bei der Bildaufnahme zunutze macht. Die meisten OAT-Techniken sind jedoch auf die Wiedergabe von 2D-Bildern mit hoher Bildrate bei relativ geringer Auflösung beschränkt. Um dies zu lösen, verwenden wir einen hochauflösenden Schallkopf, um die gesamte Tumorregion mit einer Auflösung von 100µm abzutasten und dynamische Prozesse mit 100 Bildern pro Sekunde zu erfassen. Anschließend führen wir eine Frequenzanalyse der Trends der lokalen Sauerstoffsättigung des Blutes (sO2) durch, um erstmals mit der OAT periodische Schwankungen des sO2-Spiegels (auch als zyklische Hypoxie bekannt) in bestimmten Regionen des Tumors zu identifizieren. Schließlich erweitern wir die dynamische Bildgebung auf die Ganzkörperskala. Eine schnelle Bildgebung ist wesentlich für die Erhöhung des Durchsatzes eines Systems und für die Verfolgung der Kinetik und der Biodistribution von Kontrastmitteln auf der Ganzkörperebene. Bei der OAT wird das Scannen durch ein Standard-Schritt-für-Schuss-Protokoll verlangsamt. Um diese Beschränkung zu überwinden, entwerfen wir ein neues Scanning-Schema, das auf kontinuierlichem Scannen mit hoher Geschwindigkeit (bis zu 80 mm/s) beruht, während die Position des Detektors durch feine Wegsensoren überwacht wird. Das neue System ermöglicht Ganzkörperaufnahmen unter 1 Minute. Anschließend demonstrieren wir die Machbarkeit des Systems zur Verfolgung der schnellen Verteilung von Nanopartikeln auf Ganzkörperebene.

Allem in allem stellen wir einen OAT-Scanner für Kleintiere vor, der hochauflösende molekulare und funktionelle Bildgebung ermöglicht. Sein einzigartiger volumetrischer Charakter ermöglicht eine Panoramavisualisierung und eine genaue Quantifizierung des molekularen Kontrasts. Darüber hinaus ermöglicht seine Fähigkeit, ein ganzes Organ zu erfassen oder den gesamten Körper schnell zu scannen, die funktionelle Bildgebung von dynamischen Prozessen auf mehreren Ebenen.

Publication record

This publication-based dissertation is based on the following first-author publication in peer-reviewed journals, which are reproduced in chapters 5,6,7 respectively:

Ron, A., Davoudi, N., Deán-Ben, X. L., & Razansky, D. (2019). Self-gated respiratory motion rejection for optoacoustic tomography. *Applied Sciences*, *9*(13), 2737.

Ron, A., Deán-Ben, X. L., Reber, J., Ntziachristos, V., & Razansky, D. (2019). Characterization of brown adipose tissue in a diabetic mouse model with spiral volumetric optoacoustic tomography. *Molecular Imaging and Biology*, *21*(4), 620-625.

Ron, A., Deán-Ben, X. L., Gottschalk, S., & Razansky, D. (2019). Volumetric optoacoustic imaging unveils high-resolution patterns of acute and cyclic hypoxia in a murine model of breast cancer. *Cancer research*, *79*(18), 4767-4775.

- In addition to authoring various proceedings, I also published as a contributing author in peer-reviewed journals (not part of this dissertation):

Kimm, M. A., Gross, C., Déan-Ben, X. L., **Ron, A**., Rummeny, E. J., Lin, H. C. A., ... & Wildgruber, M. (2019). Optoacoustic properties of Doxorubicin–A pilot study. PloS one, 14(5).

Littmann M, Selig K, Cohen-Lavi L, Frank Y, Hönigschmid P, Kataka E, Mösch A, Qian K, **Ron A**, Schmid S, Sorbie A. Validity of machine learning in biology and medicine increased through collaborations across fields of expertise. Nature Machine Intelligence. 2020 Jan 13:1-7.

List of abbreviations

OAI	Optoacoustic imaging
HbO	Oxy-hemoglobin
HbR	Deoxy-hemoglobin
NIR	Near-infrared
AuNR	Gold nanorods
OPO	Optical parametric oscillator
FOV	Field of view
OAT	Optoacoustic tomography
CT	Computed tomography
BP	Back-projection reconstruction
MB	Model-based reconstruction
GPU	Graphical processing unit
PET	Positron emission tomography
MRI	Magnetic resonance imaging
BOLD	Blood oxygen level depended
FDG	Fluoro-deoxy-glucose
BAT	Brown adipose tissue
GFP	Green fluorescent protein
RSOM	Optoacoustic mesoscopy
MIROM	Mid-infrared optoacoustic microscopy
MSOT	Multispectral optoacoustic tomography
HbT	Total hemoglobin

TBV	Total blood volume
sO_2	Blood oxygen saturation
pO_2	Oxygen partial pressure
NA	Numerical aperture
SVOT	Spiral volumetric optoacoustic tomography
VOT	Volumetric optoacoustic tomography
FlashOT	Flash scanning optoacoustic tomography

Contents

1. Introduction

1.1. Motivation and objectives

Current OAT imaging technologies are restricted to functional analyses of cross-sectional images. Nevertheless, to reflect realistic physiological processes, an ideal system must grant multiscale imaging of high spatio-temporal resolution, at a whole organ and body scales. Thus, the incentive for my work is to engineer a small animal optoacoustic scanner that encompasses such a unique and versatile "tool-box" for preclinical research. This is realized by mounting a high-resolution spherical transducer on motorized stages in conjugation with fast acquisition hardware and wavelength-tuned laser. Assisted by designated reconstruction algorithms, high-resolution functional and molecular imaging is obtained. Yet, a couple of gaps must be still bridged: (GAP 'A') a scanning-time / volume trade-off (namely, long scanning times for whole-body imaging) impedes fast imaging at a whole-body scale. Overcoming this gap would facilitate analyses of dynamics of contrast agents over entire organs and organ systems, which are not possible in single cross-sectional images acquired by standard optoacoustic systems. To this point, visualization of bio-distribution of optoacoustic contrast agents within the entire body at high spatial and temporal resolutions, has never been achieved. (GAP 'B') respiratory motion artifacts suppression algorithm must be designed such that it doesn't impose heavy computational burden on the system at any stage of the workflow.

All in all, this work consists of two main aspects. The first is to engineer and develop the scanning concept and system that would satisfy 'GAP A' and the algorithm to satisfy 'GAP B'. Then there is the biological applications aspect, where I apply my engineering solutions for functional and molecular imaging. An overview of these preclinical applications in presented in Figure 1-1. Each application specifically exploits a unique characteristic of the new imaging system:

(Figure 1-1a,b) Large scale (entire organ), molecular imaging. This technique was employed for the characterization of brown adipose tissue (BAT) in diabetic mice.

(Figure 1-1c,d) Local, high resolution molecular imaging. This method was employed for rendering high resolution maps of acute hypoxia in tumors.

(Figure 1-1e,f) Local, functional (dynamic) imaging. This method was employed to track cyclic (dynamic) hypoxia events in tumors.

(Figure 1-1g,h) Large scale (whole body), functional imaging. This method was employed to increase the throughput of whole-body imaging and to track biodistribution of nano-agents in the whole-body scale.

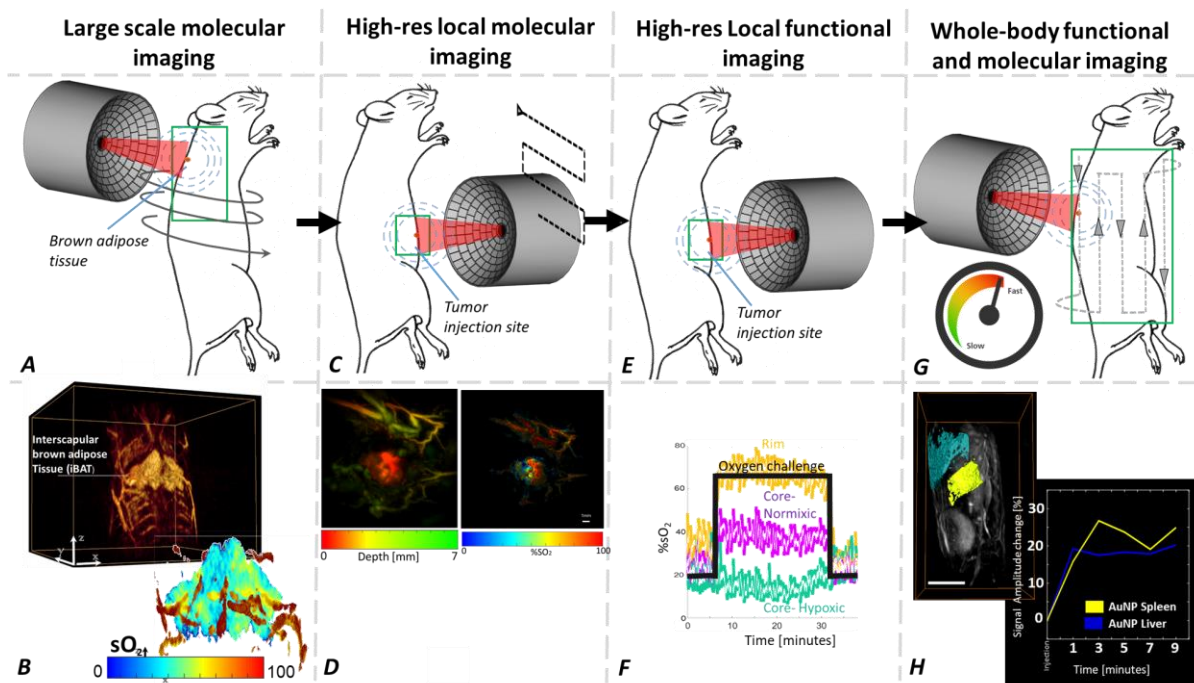*Figure 1-1 Overview of preclinical studies. (A) Imaging of BAT region and (B) quantification of hemodynamic parameters. (C) High resolution (static) scanning of breast tumors and (D) quantification of hemodynamic parameters. (E) functional (dynamic) imaging of the same tumor and (F) Dynamic analysis of hemodynamic parameters. (G) Fast and continuous whole-body imaging and (H) quantification of contrast agents biodistribution.*

1.2. Current state of research

1.2.1. Small-animal optoacoustic tomography techniques

The majority OAT systems are typically configured based on two chief approaches, namely ring-array and scanning transducer.

- Ring array:

  A ring array detector is based on a circular ultrasonic elements' geometry, which provides a complete 2π detection angle and produces a 2D cross-section image. A better coverage angle (circumference of the ring) and higher ultrasonic elements density promote large FOV and higher in-plane resolution [1]. The illumination source should provide a homogeneous illumination coverage around the ring, which may be realized by fiber bundles [1] or by lensing [2]. A 3D tomographic image can be achieved by scanning the array in the elevation direction and stacking up the slices, as employed by other tomographic modalities as well. OAT ring-arrays scanners present high-quality cross-sections of high isotropic in-plane resolution and good sensitivity for deep structures [3-5]. Yet, proper 3D rendering is hindered by the slice thickness. Thickness is governed by the acoustic focusing of the ultrasonic elements in the elevation direction. Focusing is depended upon the numerical aperture (NA) of the "acoustic lensing" and requires larger elements in the elevation axis in order to acquire thinner slices [6], which in turn leads to physical constraints in the design of the system. As a result, slice thickness is typically limited to a few millimeters and provokes an anisotropic spatial resolution in the image and low sensitivity to the boundaries of structures which are bigger than the FOV. Eventually, forming a 3D whole-body image by stacking up slices, impedes the visualization and the quantification of volumetric objects.

- Scanning transducer:

  Scanning transducer is the approach of choice for this work. In preclinical OAT imaging, this approach is less common than the ring array approach. Early implementations utilized linear or linear curved arrays, which were scanned around the object to achieve a larger

FOV. In fact, to facilitate accurate reconstruction of arbitrarily oriented structures, a large number of pressure signals around the object must be acquired, which significantly extends the acquisition time [7]. On the other hand, linear arrays (such as hand-held arrays) are widely available. Notice that an important disadvantage of small-animal OAT and ultrasound imaging is the requirement for an acoustic coupling medium. In most imaging technologies, the animal is positioned horizontally on a designated bed (bed artifacts are pre-known and can be corrected), which moves through a ring geometry detector. Yet, a solution in the form of a bed for OAT is unworkable as it would not match the acoustic and optical properties of the medium and the animal. In fact, to achieve a whole-body OAT scan, the animal and the ultrasonic transducer are immersed in water. Positioning the animal horizontally is practically impossible as water level exceeds the nose and mouth level. Therefore, solutions for horizontal positioning are scarce and impractical (in fact, there is only one commercial system which supports horizontal imaging). Subsequently, animal holders are restricted to a vertical orientation, which may not reflect the natural pose of the animal and may affect physiological parameters.

1.2.2. Motion rejection methods in OAT

Various systems acquire and average multiple frames per transducer position, to enhance SNR and eliminate (respiratory) motion artifacts. Acquisition of multiple volumetric frames at multiple transducer's positions produces an excessive amount of data (roughly tens of gigabytes). Importantly, simple data averaging approaches hinder efficient motion rejection and SNR enhancement. Thus, averaging of multiple time-resolved signals (raw data) during early an acquisition stage is common but not as effective (as demonstrated in this work). In addition to certain "gated" acquisition methods which can be applied (e.g. synchronizing acquisition to physiological triggers, such as electrocardiogram (ECG) signal [8]), motion artifacts can be effectively rejected at the post-processing stage by "prospective self-gated" techniques, where the physiological trigger is extracted from the image data itself (also applied in other imaging modalities [9,10]). "Prospective self-gated" techniques are particularly convenient since any further "gating" instrumentation become obsolete. Nevertheless, they once again require saving excessive

amount of data for post-processing. Moreover, the analysis of image data requires reconstruction of the many acquired frames, which is a heavy process.

1.2.3. Imaging metabolism with OAT

Oxygen consumption is an indirect measure of aerobic metabolism, characterized by an increase in blood flow following oxygen demand [11]. This relationship between oxygen consumption and metabolic activity specifically facilitates the increasing use of "label-free" OAT hemodynamic measurements for metabolism research. So far, OAT imaging of metabolic-related processes has been dominantly exploited for (a) functional neuroimaging, because cerebral hemodynamic changes are closely linked to neuronal activity by neurovascular coupling [12] (b) tumor metabolism [13], as will be elaborated in the next chapter. In addition, OAT hemodynamic-related measurements are exploited in the physiological research of other tissue types, e.g. muscle tissue [14] and tendons [15] .Yet, the scope of the existing work is limited, particularly regarding research of diseases such as obesity and diabetes. It is worth mentioning that other OA techniques are also exploited for studying metabolic-related processes, e.g. optoacoustic mesoscopy (RSOM) used employed for the assessment of dermatological conditions [16,17] and mid-infrared optoacoustic microscopy (MIROM) for label-free metabolic imaging [18].

1.2.3.1. Brown adipose tissue imaging with OAT

White adipose tissue (that is, "normal fat") stores triacylglycerides in its cellular fat droplets. In contrast, BAT serves as a heat producing tissue, which essentially burns calories to regulate body temperature [19,20]. The study of BAT is important since it is closely related to various human diseases such as diabetes and obesity [21]. Briefly, OAT observations on diabetes can be made by: (a) studying changes in tissue oxygenation which is indirectly linked to tissue metabolism. (b) studying structural changes of blood vessels, since diabetes causes angiopathy which in turn, leads to deterioration of vasculature [22]. Thus, utilizing OAT for tracking such phenomenon in diabetic mice models may contribute to a better understanding of metabolic alterations in patients. So far,

the most substantial study on BAT metabolism with OAT [23] proved strong correlation between oxygenation measurements and indirect calorimetry (which serves as the gold standard for the analysis of energy expenditure in mice [24]) and with PET measurements (which can detect high glucose-uptake rates by employing FDG tracer, see next chapter). Conclusively, the researchers demonstrated the feasibility of multispectral optoacoustic tomography (MSOT) to observe BAT activation (where BAT is manipulated to increase metabolic activity).

1.2.3.2.   PET imaging and metabolism

PET a dominating technique in the field of molecular imaging for preclinical research, particularly in the context of metabolism. In terms of radiation, PET employs radioactive tracers which impede longitudinal studies. Therefore, non-ionizing radiation is an important advantage of OAT over PET. Current PET technology provides inferior spatial resolution in comparison to OAT. For instance, a standard Micro-PET (an animal imaging scanner) provide a resolution of 1-2 mm [25,26]. More recent developments push the resolution to below 1 mm [27]. Normally, PET is depended on multimodality approaches (e.g. PET-CT [28,29]) to facilitate anatomical localization. In regard to acquisition time, the low counts rate (rate of true coincidence events on the detector) of PET (for example, in comparison to CT) promotes long acquisition times [30]. Subsequently, a whole-body scan of a small-animal may last ~20 minutes [31] (similar to the time scales of a whole-body OAT imaging). The contrast of PET is typically depended on exogeneous radioactive tracer, *e.g.* 18F-Fluoro-deoxy-glucose (FDG). The conjugation of glucose as part of the FDG tracer makes it an ideal tracer for metabolism imaging. It positions PET as a prominent technology for such metabolism related applications. The sensitivity of PET to the very minimal concentration of tracer (10-12 moles/l) is extremely high and can compete with the most sensitive optical techniques [32]. Some common applications of PET are: (1) Metabolism imaging (*e.g.* detection of the presence of metabolically active cervical, supraclavicular, and paravertebral BAT in adult humans has been discovered by the detection of high glucose-uptake rates by utilizing FDG-PET[33]). Note that OAT also demonstrates promising capabilities for metabolism imaging based on the fact that oxygen consumption is an indirect measure of aerobic metabolism and that measurements of sO_2 have shown good correlation with gold standard calorimetry measurements [34]. (2) Pharmacokinetics

(*e.g.* the determination of drug concentration in tissue by direct labelling of the drug with a radioisotope). As mentioned, PET's "label-depended" imaging may impede longitudinal experiments (for instance, by depending on the half-life time constraints of an isotope [35]). (3) Cancer research (*e.g.* tumor metabolism, angiogenesis or hypoxia imaging can be studied via different radiolabeling methods [36-38]).

1.2.4. Cancer imaging

1.2.4.1.　Cancer imaging with OAT

OAT is being increasingly adopted for cancer research, due to its unique capability for "label-free", noninvasive and non-radiating monitoring of hemodynamic parameters. OAT offers several approaches to look at tumors:

a. By imaging at the structure and morphology of the tumor's micro-vasculature, it is possible to follow tumor growth and vascular development [39-41]. Moreover, quantification of HbT signals may further supports perfusion related findings.

b. Quantification of sO_2 grants insights on tumor oxygenation [42-45]. Furthermore, sO_2 measure is clinically relevant since it can be directly translated to oxygen partial pressure (pO_2) according to the Kelman and Severinghaus model of the oxygen dissociation curve [46]. Notice that sO_2 is not directly relate to tissue perfusion, since perfusion is also depended on blood flow.

c. By exploiting a number of specific contrast agents have been further devised to sense cancer bio-markers [47,48].

d. By administrating of non-specific contrast agents which circulate through the tumor vasculature, a technique referred to as dynamic contrast enhancement (DCE), and observing the wash-in and wash-out kinetics [42]. In addition, by observing at the accumulation of these contrast agents in the tumors as a result of "leaky vessels" [49].

1.2.4.2.　MRI and cancer imaging

MRI benefits from both functional and molecular properties. From a functional point of view, MRI obtains molecular sensitivity by paramagnetic contrast. Moreover, is capable of tracking functional dynamic responses of local events. In terms of radiation, MRI (and OAT) utilizes non-ionizing radiation, and hence, do not affect long term, longitudinal preclinical studies. The resolution MRI grants ranges from tens up to a few hundreds of µm, similar to OAT. MRI's acquisition time is primarily dictated by long relaxation times (for instance, Longitudinal (T1) relaxation time for blood, by 1.5 Tesla MRI equals ~1400 milliseconds [50,51]). Hence acquisition is significantly longer than the single ns-laser pulse durations in OAT. Mechanistically, the signal contrast-dependency in both technologies benefit from molecular sensitivity to hemoglobin: MRI employs blood oxygen level depended (BOLD) signal [52,53] and OAT employs optical absorption of hemoglobin. Therefore, both modalities are capable of spectroscopic observations derived from variations in oxygenation. Common applications of MRI include: (1) Neuroimaging, *e.g.* Functional "label-free" hemoglobin measurements of cerebral hemodynamics in response to different stimuli [54]. (2) Cancer research, *e.g.* Oxygen-enhanced MRI, which is used for quantifying the spatial distribution and extent of tumor oxygen delivery *in-vivo* [55]. Notably, this technique is also adopted by OAT (3) Cardiac imaging, *e.g.* Pulmonary transit time and hypertension imaging [56,57]. Notice that OAT is valuable for cardiac imaging in animal models, due to its unique capacity of imaging hemodynamics parameters at video rate [58,59].

2. Theoretical background

This section consists of an overview of the principles of optoacoustic tomography (OAT). I relate this introduction directly to the scope of my work, the developed system and the research topic. The interested reader may also refer to these two comprehensive articles which cover the theory of optoacoustic imaging [60,61].

2.1. The optoacoustic effect

Optoacoustic imaging (OAI) rely on irradiating a tissue by a short-pulsed laser beam to achieve a thermal and acoustic impulse response. The light penetrating the tissue, is scattered and absorbed, where local absorption results in local heating of biological substances.

If the light energy is efficiently converted into heat (T), it can be written as follows:

$$T = \frac{A_e}{p C_v} \qquad (1.1)$$

Where A_e is the volumetric optical absorption, p is mass density and C_v is the heat capacity at a constant volume.

Due to the short-laser pulse (typically $t_L < 10$ nanoseconds), the illuminated target volume (at distance r) undergoes negligible volume expansion if the following condition is fulfilled:

$$t_L < \frac{d_C}{v_s} < \frac{d_C^2}{4\alpha_{th}} \ (1.2)$$

Where d_C is the length of the absorbing target (e.g. blood vessel), v_s is the speed of sound in the specific medium, α_{th} is the thermal diffusivity of the target. Intuitively, the pulse duration should be shorter than time for the acoustic signal to escape the illuminated region in the target. This in turn should be shorter than the thermal relaxation time of the target, e.g. the time heat diffuses away.

Instead, the thermal energy is immediately converted into pressure, as follows:

$$p_0(r) = \frac{\beta T(r)}{k} \ (1.3)$$

Where β denotes the thermal coefficient of volume expansion and k denotes the isothermal compressibility.

2.2. The optoacoustic equation

Briefly, the conversion of local heat into an acoustic propagating wave is described by the following "optoacoustic equation":

$$\left(\nabla^2 - \frac{1}{v_s^2}\frac{\partial^2}{\partial t^2}\right)p(r,t) = -\frac{\beta}{C_p}\frac{\partial H(r,t)}{\partial t} \quad (1.4)$$

Where v_s denotes speed of sound. β denotes the thermal coefficient of volume expansion. C_p denotes the specific heat capacity at constant pressure. H is the heating function defined as the thermal energy converted per unit volume and per unit time; it is related to the absorption coefficient μ_a and fluence rate Φ by H = μ_aΦ. If the heating function would be a constant (time invariant), then the derivative of the heat function would yield 0, meaning that heat transients are essential to produce the pressure wave.

2.3. Contrast

Contrast in OAI is derived from the incident light wavelength at the distinctive light absorption profiles of chromophores. In this work I look at both endogenous and exogenous chromophores. Regarding endogenous chromophores, I mainly observe at oxy-hemoglobin (HbO), deoxy-hemoglobin (HbR) contrast in the near-infrared (NIR) window, a range of wavelengths from 650 to 1350 nm where light has its maximum depth of penetration in the tissue [62]. More specifically, around the isosbestic point of hemoglobin at ~800 nm. Regarding exogenous chromophores, in this work I exploit gold nanorods (AuNR) as optical contrast agents [63,64] (these are administered intravenously to the body). AuNR benefit from high optical contrast and their peak absorption wavelength can be tuned by controlling their aspect ratio [65]. I employ AuNR absorbing at 1064 nm. This wavelength lies within the spectral regime referred to as the "second NIR window", where it

is said that the tissue generates lower and more robust optoacoustic (OA) signal amplitude (relative to the signal that is generated by the exogeneous chromophores) [65,66].

2.4. Light fluence

Based on Eq. 1.1-1.3, the pressure signal is linearly dependent on the molecular optical absorption A_e as well as additional parameters (mass density and heat capacity) which can be assumed homogeneous inside the region of interest. We now define a set of parameters as a Grüneisen parameter Γ, where:

$$\Gamma = \frac{\beta}{kpC_v} \qquad (1.5)$$

Combining Eq. 1.3 and 1.4, we find the following expression:

$$p_0(r) = \Gamma A_e \quad (1.6)$$

Meaning that the reconstructed image linearly corresponds to the optical absorption image. Hence, we can apply corrections related to the light source and light distribution already over the reconstructed image. Such corrections are essential for achieving well quantifiable results.

Firstly, it is necessary to correct for the power output of the laser. The laser may fluctuate in time but also bear different energy levels per different wavelengths. Corrections can be done by splitting the light path into a reference path which is monitored by some sort of a power-meter (in the work presented here I employ an integrated photodiode inside the Optical parametric oscillator (OPO) laser unit). Then, each reconstructed frame is normalized accordingly.

Secondly, a fluence correction should be applied. Due to the effective light attenuation in a turbid medium (e.g. biological tissues), the light is not scattered and absorbed homogenously in the volume, but rather decays in space. This results in a pressure signal $p_0(r)$, which does not reflect the true density of different chromophores in the medium. This is a significant challenge in OA imaging where accurate quantification of chromophores is desired, within extremely heterogeneous biological tissues. Accurately modeling the light propagation in the volume is practically impossible because of the unknown and constantly changing underlying anatomy. The modeling problem is usually simplified into a homogeneous medium or a medium consisting of

limited segments of different tissues. Moreover, it should be noted that optical properties are also wavelength depended. In my work I segment different regions of specific tissue types, and correct the fluence of each individual region for exponential light attenuation (with depth) according to:

$$e^{-\sqrt{3\mu_a(\lambda)\left(\mu_a(\lambda)+\mu'_s(\lambda)\right)}z} \qquad (1.7)$$

Where μ_a is the absorption coefficient, μ'_s is the reduced scattering coefficient and z is distance from animal's surface. The wavelength-dependent $\mu'_s(\lambda)$ and $\mu_a(\lambda)$ coefficients, which belong to the optical properties of a specific tissue are taken from the literature.

2.5. Multispectral imaging and unmixing

Each specific volume within the body consists of multiple chromophores at different concentrations. Therefore, the optical absorption (A_e) within a finite volume in tissue is the result of a weighted summation of the concentration and the optical density of each chromophore. In order to quantify the concentration or proportion of each chromophore, it is necessary to decompose the individual contributions to the total absorption. This spectroscopic method is referred to as unmixing and is required for multispectral imaging. To this end, I employed a pulse to pulse tunable OPO laser, to sweep along a predefined wavelength range at a pulse rate of up to 100 Hz, thus acquiring images at multiple wavelengths.

Here, I use linear unmixing to extract chromophore content. Further information on this method is available elsewhere [67]. We now look at optical absorption A_e :

$$A_e(\lambda_i) = \phi_i * \mu_{a_i} \qquad (1.8)$$

Where λ_i is the wavelength i. ϕ is the light fluence distribution (see 2.4), μ_{a_i} is the wavelength-dependent absorbance coefficient. Note that fluence correction is applied prior to unmixing, therefore the absorption is already independent of ϕ:

$$A_e(\lambda_i) = \mu_{a_i} = \sum_{j=1..S} \varepsilon_{j_i} * C_j \qquad (1.9)$$

Where S in the number of chromophores, ε_{j_i} is the corresponding molar extinction coefficient of chromophore j at wavelength i. C_j in the chromophores' concentrations. The goal is to find the value of C_j for each voxel. Equation 1.9 can be rewritten in the following form:

$$A = CE \qquad (1.10)$$

Where A represents the optical absorption values per wavelength λ_i at every voxel of distance r in the volume:

$$A = [A(\lambda_1, r) \ldots A(\lambda_{,i}, r)] \qquad (1.11)$$

C (in Equation 1.10) is the concentration vector of j number of chromophores $C = [C_1 \ldots C_j]$ (which are unknown). E is the matrix of extinction coefficients $E = [\varepsilon_1 \ldots \varepsilon_j]^T$ (which are known).

By solving the least-square problem we can find the concentrations C':

$$C' = \arg min_C \left\| CE - H' \right\| \qquad (1.12)$$

With the solution:

$$C' = H'E^+ \qquad (1.13)$$

where H' is the reconstructed optical absorption at all wavelengths and E^+ is the pseudoinverse of E.

2.6. Resolution

The resolution of the system is derived from the characteristics of the ultrasonic elements. The detectors are composed, in this case, of piezoelectric elements which are distributed on a spherical surface (in 3D). The normal to each element faces the center of the sphere, such that the effective field of view (FOV) and optimal sensitivity are around the center of the sphere (Figure 2-1).
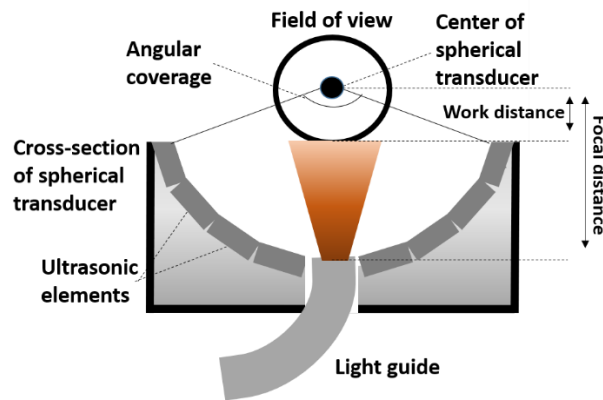
Figure 2-1 – Schematics of a cross-section of the transducer, consisting of a spherical array of ultrasonic elements, illustrating the angular coverage and field of view of such a transducer's design.

In addition to the central frequency of the transducer's elements, the spatial resolution is also depended on the combined effect of the number of transducer elements and their size. These two properties also dictate geometrical constraints and the physical design of the transducer, which subsequently affects the angular coverage and working distance of the detector.

2.7. Image compounding

To further increase the FOV, scanning and compounding of volumes (volumetric frames) are implemented. Scanning is accomplished by mounting the transducer on motorized stages. Following reconstruction of each volume, an image can be compounded. This normally requires a knowledge of the exact position and orientation of the transducer in space during acquisition of each volume (but could also be executed without such previous knowledge [68]). Depending on the scanning technique, neighboring volumes often share overlapping regions. Various compounding approaches which optimize this compounding problem exist, yet straight-forward approaches such as averaging or summation of overlapping volumes prove to yield satisfactory results, even if compared to the more computational demanding methods [69].

In this work, the transducer must be translated and rotated, to cover a large sample (e.g. a mouse). When translating the transducer, the step size is dictated by the effective FOV of the transducer; for instance, a large FOV allows larger sampling steps and results in shorter scan times. To achieve a complete angular coverage, it is necessary to rotate the transducer, around the animal (Figure 2, left). In practice, rotation can be restricted by a short working distance between the transducer and the animal. For that reason, transducers of higher angular coverage (which are normally afflicted
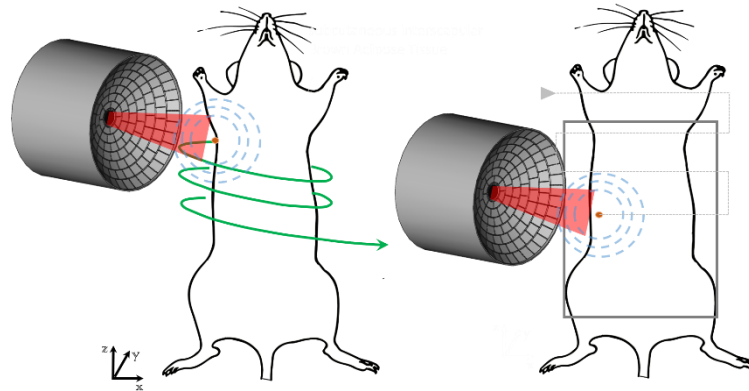

Figure 2-2 – Illustrations of different scanning schemes: (left) Rotational (spiral) scanning of the detector around the animal (right) traditional raster scanning scheme of a single plane.

by a shorter working distance) cannot be rotated around a mouse. In such cases, targets can be alternatively raster-scanned on a single plane (x-z plane, Figure 2-2, right). Raster scanning would be ideal under the following circumstances: (1) high resolution is required (2) target is relatively superficial (3) target is either small enough or flat. For instance, imaging subcutaneous solid tumors models require high resolution in order to observe heterogeneity (also elaborated in 7). The tumors are implanted superficially, and they are small enough (< 10mm) to be considered flat. Therefore, raster scanning such tumors by a high-resolution transducer would be beneficial.

2.8. Acquisition time

2.8.1. Acquisition time in OAT

Due to the inherent capacity of OAI to collect image data from the entire imaged region following a single ns-laser pulse, OAI acquisition times are generally short. The system commonly employs a 256 elements transducer with a limited angular coverage of 90°, achieving imaging depth of over

1.5 cm in living tissues without signal averaging [70-72]. The fact that averaging is dispensable, significantly shorten the total number of acquired frames and therefore, the total scan time. Nevertheless, to further enhance the SNR of deeper structures, acquisition and averaging of multiple frames may be necessary (where signal increases in relation to the number of acquired frames, and noise by the square root of acquired frames). Subsequently, scan times are often extended.

As mentioned above, step size is another factor which affects scan times. Step size determines the number of total scanning positions in the scan, which subsequently dictates the number of acquired frames. Here it should be noticed that the number of the transducer positions governs the overall number of translation and rotation events. For such a "step by step" scanning protocol, each movement involves acceleration and deceleration, which are highly time consuming. In most imaging technologies, the "step by step" scanning protocol is unavoidable, due to long integration time of each individual frame acquisition.

2.8.2. Acquisition time in CT

Computed tomography (CT) benefits from short integration times which facilitate continuous scanning protocols (For example, 3D C-arm CT scanner [73,74], or a continuous bed motion acquisition CT[75,76]) and fast scanning of a whole animal. Since OAI also benefits from fast acquisition, this motivates the adaptation of CT continuous scanning protocols into OAT (see chapter 4).

Even though CT doesn't fall under neither one of the categories of molecular or functional imaging, it shares some important technological concepts with OAT, which are essential for the understanding of this work. In terms of radiation, CT employs ionizing x-ray source (which may impede longitudinal preclinical studies). CT detectors designed for Micro-CT (small animal imaging systems) offer excellent spatial resolution (<10 micrometer [77]). The temporal resolution (meaning, the acquisition time of a single frame) of CT is in the range of tens of milliseconds [78] where the total acquisition time for a CT scan depends on various factors (*e.g.* the number of acquired projections, number of skipped images and the detector's integration time) but generally, a whole-body scan system lasts about a few minutes [79] (which serves as a motivation to my work on fast scanning OAT, see chapter **Error! Reference source not found.**). The contrast of CT is

based on tissue density. This constitutes high contrast to dense tissues such as bony structures (which affirms CT as the ideal modality for anatomical reference) but lacks the separation power between different soft tissues (On the contrary, OAT lacks the contrast of bony structures, but can differentiate well between soft tissues, *e.g.* muscle, tendon, fatty tissue, brown adipose tissue). For the visualization of the vascular system, CT requires the administration of a radio-opaque contrast agent (e.g. Iodine) intravascularly. In comparison, OAT can achieve good vascular contrast based on endogenous contrast agent imaging. In addition, exogeneous contrast agents may be exploited in OAT for super-resolution techniques [80] which may significantly enhance resolution.

2.9. Notes on image reconstruction

The objective of image reconstruction is to recover the initial pressure distribution in the medium from a finite number of time-resolved pressure signals. In OAT this is implemented by either one of the following methods: back-projection reconstruction (BP) or model-based reconstruction (MB). BP is based on the analytical solution to the optoacoustic acquisition in the time-domain and its most used description and implementation can be found elsewhere [81]. Instead, MB applies inversion of a discretized version of the optoacoustic equation in time or frequency domains [82-84]. Since our imaging system engages volumetric information, it requires 3D reconstruction. Such reconstruction is supported by both BP and more recently, by MB [82,85]. BP boasts a straightforward implementation and low computational resources, hence fast processing time. On the other hand, Model-based involves iterative algorithms and heavy calculations of matrices inversions which requires heavy computation and favor graphical processing unit (GPU) implementations. MB is commonly utilized for reconstruction of cross-sectional (2D) images, e.g. in systems which operate cylindrical array traducers. In such cases, MB demonstrates improvement in image quality and elaborated details [4,86]. Recent 3D MB works also suggested some advantage over 3D BP [85], which was particularly demonstrated by improved SNR and visibility of vascular structures in *in-vivo* images. The high SNR of MB may unveil deeper structures in the image, where noise dominates. Yet, our evaluation found a minor contribution of the 3D MB to the image quality, therefore I chose to utilize 3D BP for reconstruction chiefly due to the rather short processing-time.

3. Technological aspects of small-animal optoacoustic imaging system development

3.1. Design of continuous motion scanning

In this work I tackle the issue of long scan times. Briefly, accelerating scan times is essential for increasing the throughput of a system. Throughput is an immanent matter in preclinical imaging, particularly in the field of pharmaceutical research, where a very large sample number of animals is required for each study, and time is of the essence. Moreover, visualization of fast pharmacokinetics and biodistribution at the whole-body level is desired (namely, acquiring a whole-body image at high temporal resolution). In practice, a major bottleneck in tomographic imaging is the translation of motors in discrete steps (also referred to as "step by step" or "step and shoot" scanning), which demands repeated acceleration and deceleration of the motors. Hence, much like the concept of "helical CT", a continuous motion of the scanner (or alternatively, the "patient's bed") is required in order to eliminate such "inter-scans delays" [87]. In this regard, both CT and OAT benefit from fast acquisition times. OAT has the capacity for collecting image data from the entire imaged region following a single pulse from the ns-laser. I therefore hypothesized that by combining its fast frame acquisition (dictated by a 100 Hz pulse rate of the OPO laser) with the isotropic resolution of the spherical detector, continuous motion of the scanner could be realized. This is made possible by continuously translating the motor. Here, continuous motion is bounded to a single direction, the vertical axis, which scans the animal from head to tail. In this direction the motor covers long distances while effectively eliminating many unnecessary steps. The rotation is constrained by the power supply wires of the transducer (in CT, this is solved by a "slip ring" design), and by the optical fiber bundle. In practice, once the transducer is turned 360°, it must be turned back to its starting position to uncoil the wires. I therefore drive the transducer in turns – continuous motion in the axial direction followed by a step in the angular direction, and so forth (as depicted in Figure 3-1. The exact disposition of the vertical motor is monitored with a high-resolution time of flight position (distance) sensor. The criteria for choosing such a sensor is (a) the position sampling rate should comply to the laser pulse rate (at least doubled, following the sampling theory) (b) the measurement resolution should be higher than the spatial resolution of

the transducer (the 4 MHz central frequency transducer that I used, provided a spatial resolution of ~200 µm) (c) the working distance's range of the sensor should be sufficient to cover the animal's height. Notably, time of flight distance sensors excel at high resolution (~15 µm for our model) at short distances (work distance of a few tens of cm with a range of ~ ±5 cm for our model, enough to cover a whole mouse) at sampling rates which are much higher than the laser pulse rate. The fixed distance sensor measures reflectance from a plate at the bottom of the vertical motor (see Figure 3-2). It is triggered in sync with the DAQ by the laser pulse trigger signal from the OPO laser.
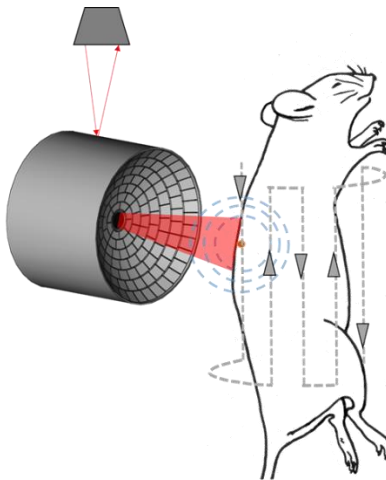

Figure 3-1 - Illustration of the trajectories of the continuous scanning scheme. A distance sensor is continuously sampling the disposition of the transducer in the vertical axis.

Subsequently, the compounding of consecutive frames (volumes) should be considered. Owing to the isotropic resolution of the spherical transducer in all directions, accurate frames compounding in the vertical direction is permitted. Here, certain concepts associated with continuous scanning are somewhat different from those of the "step by step" scanning. In the latter, the step size should be maintained below the width of the frame in the vertical axis (or below slice-thickness, In the case of a ring transducer). In "step by step" scanning, multiple frames are acquired at each step, to increase SNR and eliminate motion artifacts (see chapter 1.2.2). Obviously, continuous motion does not permit averaging of multiple frames at a fixed position of the transducer. Also note that

the motion rejection algorithm that I propose (see chapter 5) cannot be applied to this system. An alternative solution would be to use "gated" methods, but this is not covered in the scope of this work. Here, instead of acquiring multiple consecutive frames in times, we now acquire closely overlapping frames in space. Consecutive frames partially overlap due to the high frame rate. Next, we denote pitch as the distance between two neighboring frames (very similar to "step size"):

$$pitch = velocity/(frame\ rate)$$

For example, if the motor is translated at maximal velocity of 80 mm/s and acquire at the maximal laser pulse rate (100Hz), then pitch would be equal to 0.8 mm. If we assume that FOV equals 10 mm in the vertical axis, we find that 92% of the volume of all consecutive volumetric frames, overlaps. Thereupon, by compounding volumetric frames in space (by shifting them according to the position measurement), we essentially average frames and thus increase the SNR of the image. Likewise, lower motor velocities correspond to higher SNR levels, as I demonstrated by phantom experiments. Note that SNR is also related to other factors, particularly to laser energy and energy density. The maximal motor velocity that has been tested is 80 mm/s (limited by the specification of the specific motor), which facilitated high quality whole-body images and accurate quantification. At such velocity, a single sweep of ~1 sec is required to scan the transducer from head to tail. In the angular direction, I apply 24 rotational steps at 15° separation, thus covering a complete angular FOV (each step also last ~1 sec). Altogether, ~2400 volumetric frames are captured during a whole-body scan. Currently, the transfer of the data to hard drive is time consuming (~ 1 min). Such a delay can cause delay between consecutive whole-body scans. This bottleneck could be overcome by faster compression schemes or by paralleling scanning and saving.
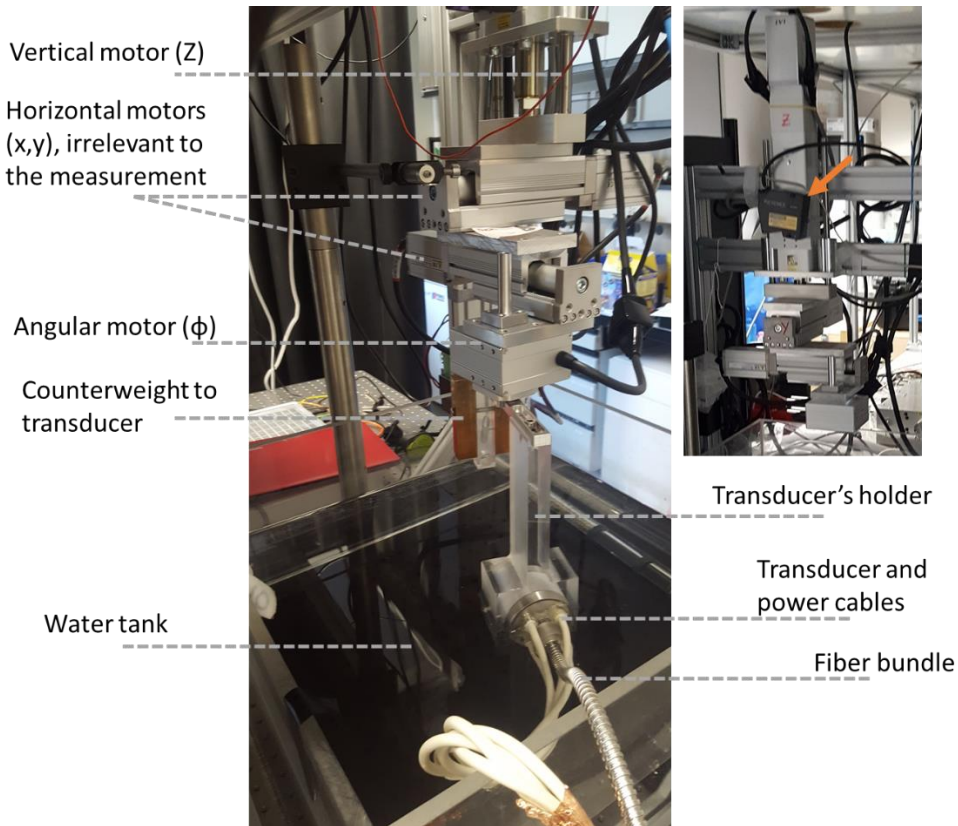
Figure 3-2 – (left) Image of the flash optoacoustic tomography setup. The animal is immersed inside the water tank by a designated holder. The transducer is translated and rotated around the animal. (right) image of the distance sensor (red arrow) mounted on the vertical axis (z).

Here, it is worth mentioning the difficulty of imaging at a full angular coverage of 360° (a full rotation around the animal). Unlike other imaging modalities, bed-like designs are not practical in OAT. In fact, any kind of object that stand between the animal and the transducer would interfere with the measurement. In previous implementations (such as in the spiral volumetric optoacoustic tomography (SVOT) system (see chapter 6), the design of the animal was such that a metallic rod blocked about 60° of the angular view (see Fig. 1 in [88]). In my new design, a full angular coverage is obtained by eliminating any object that stand between the upper and lower plates (see Figure 3-3). Alternatively, the upper plate is fixed by a rod which is concentric to the rotation axis. This rod in position inside a shaft that goes through the transducer arm and the angular motor. It is fixed to a construction at the top of the system. That way the upper plate is held in place is independent of the lower plate. Likewise, the angular and vertical motors can move freely.
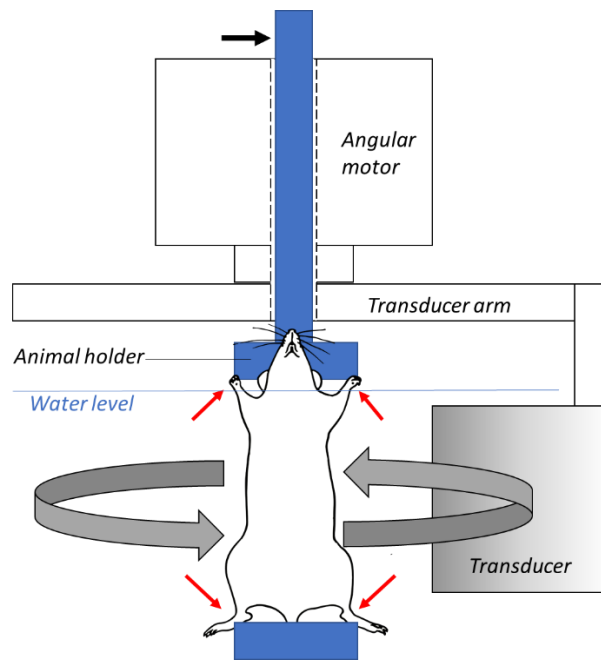
Figure 3-3 - Schematics of the animal holder. The animal is secured to the upper and lower plates of the holder by the paws (red arrows). The lower plate is fixed to the water tank floor. The upper plate in fixed through a shaft in the motor at a fixture point (black arrow) above the system. Thereby, the transducer is free to rotate around the animal, and FOV is widely open.

3.2. The concept of motion correction algorithm

Here, our main motivation is to come up with a "self-gating" technique which is lighter and quicker. A very useful and straightforward technique in the image domain is to look at the autocorrelation matrix of all consecutive frames (at a certain position of the transducer) [88]. If I assume that a mouse respirates at a rate of 60 Hz, then acquisition of multiple frames over 1 sec would capture an entire breathing cycle (inhale and exhale). I typically acquire at high frame rates (10-100 Hz) such that multiple frames are acquired during an event, and later reconstructed into images. The autocorrelation matrix of these images can be divided into two groups: "Static" (between breathing cycles) images reveal high correlation coefficient; "Motion" (within breathing cycles) images reveal low correlation. Thus, by grouping the

22

images, it is possible to reject the "motion" group and maintain the "static" group exclusively for averaging. Notably, I was able to demonstrate that a very similar method can be implemented on the time-resolved signals domain. Intuitively, one can think of each frame as a 2D image of time-resolved signals (corresponding to samples in times per channels of ultrasonic elements). In a similar fashion, it is feasible to effectively cluster their autocorrelation matrix into two groups by a 2nd order k-means. As a result, the computation time is significantly reduced, since reconstruction of multiple frames is avoided. In conclusion, this algorithm is useful in two scenarios:

(a) At the acquisition stage, following the acquisition of multiple frames at a specific transducer position, the algorithm can evaluate these frames on-line, reject the "motion" frames and average only the "static" frames. Eventually, data size is significantly reduced since only a single frame is saved per transducer position. Furthermore, any motion rejection operations at post-processing stage is redundant

(b) At the post-processing stage, the algorithm is applied in a similar fashion to the image domain method but eliminating an unnecessary reconstruction step.

3.3. Quantification of hemodynamic parameters

In chapter 6, I use the scanner to image the subcutaneous interscapular BAT (iBAT) in mice, which is located in the upper back region. The fact that the iBAT is relatively superficial and highly perfused assists in acquiring hemoglobin signals of high SNR. The two most widely used "label-free" OAT hemodynamics parameters are:

(a) The OA signal amplitude at the isosbestic point of hemoglobin (wavelength = ~800nm). This signal (denoted as total hemoglobin (HbT) and sometimes also referred to as total blood volume (TBV)) reflects on changes in vessels density or changes in vessels volume (such in the case of vasoconstriction and vasodilation) or hemoglobin concentration.

(b) The spectrally unmixed HbO and HbR components and the calculated blood oxygen saturation (sO_2):

$$Blood\ oxygen\ saturation\ (sO_2) = \frac{HbO}{HbO+HbR} \qquad (3.1)$$

This type of oxygenation measurement reflects on oxygen consumption in the tissue and consequently, is linked to tissue metabolism (as will be elaborated in the next chapter).

Our objective is to demonstrate the advantage of 3D imaging over cross-sectional imaging (such as with the MSOT system) for the visualization of BAT and quantification of hemodynamics parameters. For that purpose, I take advantage of the good angular coverage of scanner and its high molecular optical contrast. The scanner is equipped with a spherical transducer which facilitates a FOV of 10 x 10 x 10 mm^3 and central frequency of 4 MHz (corresponding to a resolution of 200 µm). It allows a relatively limited angular coverage (90°) but a very practical working and focal distance (40 mm).

Our results demonstrate that the scanner could render high-resolution (~200µm) 3D views of the distribution of BAT and its intricate microvasculature. We suggest that the true volumetric nature of the spherical transducer and the large angular coverage provided by the scanner enable accurate 3D reconstructions not afflicted by limited-view effects. This facilitates enhanced visibility of the 3D tissue morphology and physiologically relevant, quantitative readings of HbT and sO$_2$. Clearly, the fact that information is analyzed and quantified over the entire BAT volume (instead of individual 2D slices which are subjectively chosen), contributes to the accuracy and objectivity of the measurements. In addition, owing to the high sensitivity to blood contrast, robust sO$_2$ maps could be produced. I use these sO$_2$ maps to segment large arteries from tissue vasculature. This is achieved by accounting for the high sO$_2$ values of arterial blood and the relative lower oxygenation of the highly metabolic BAT tissue. Notably, the fact that I can employ sO$_2$ maps for segmentation should increase our quantification quality, by separating BAT from its interwoven supplying vessels. Consequently, this work demonstrates significant differences in sO$_2$ and HbT levels between healthy and diabetic mice.

3.4. Tracking hemodynamic parameters

In this work, I study the two types of hypoxia, namely acute hypoxia and cyclic hypoxia [89]. To achieve accurate localization of hypoxia, increased resolution is demanded. To push the resolution

higher to the order of 100 µm, I replaced our default 256 elements transducer (central frequency of 4 MHz, as installed in the previously mentioned SVOT system) and mount 512 elements transducer (central frequency of 10 MHz) on a set of motorized stages. The new transducer grants better angular coverage of 140° but a smaller FOV of 6 x 6 x 6 mm^3 and a shorter focal distance of 30 mm. The short focal and work distance of this transducer hamper the rotation of the transducer around the animal. Nevertheless, the target breast tumor is superficial, and has a diameter of 6-8 mm, therefore I can conduct a raster-scan (where the transducer is facing the tumor) to obtain a larger FOV of the entire tumor environment. In fact, we can also contain a large portion of tumor within the FOV, even without scanning.

Acute hypoxia is the typical hypoxia condition, which is the long-term state of low oxygenation in some regions of the tumor [90,91]. Here, I wish to employ high resolution imaging in order to map heterogeneous hypoxic regions within the tumor. In addition to the available "static" measurements of HbT and sO_2 (similar to the produced sO_2 and HbT maps of the BAT, as described in 6), I employ a dynamic, oxygen-enhanced technique, where changes in respiratory gas are applied, from air to 100% oxygen (a protocol adopted from MRI [55]). These changes directly reflect on vascular maturity and function and previously showed better correlation than "static" sO_2 with histological validations of hypoxia state [43]. Here It is worth to discuss the limitations of spectral unmixing and sO_2 quantification: Accurate sO_2 quantification is impeded by the heterogeneity of biological substances, which causes a wavelength-depended distortion in light fluence. For that reason, even though sO_2 serves as an absolute and clinically relevant measure, its values should be used with caution. Hence, the proposed oxygen manipulation could assist in reducing errors of sO_2 quantification. A subtraction of two sO_2 values (from the same pixel) at distinct oxygenation states (air and 100% oxygen), derives a differential measure (denoted as ΔsO_2), which can reject some common errors related to local light fluence. We demonstrate that the calculated ΔsO_2 map of the tumor matches to three distinct functional regions in the tumor (rim, hypoxic region and normoxic region).
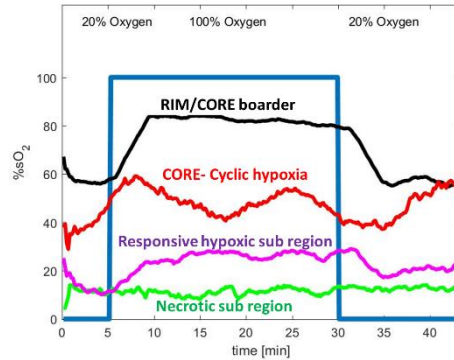
Figure 3-4 - Example of the sO2 trends of individual pixels in response to an oxygen stress challenge.

Next, I exploit the capability of system to capture the entire tumor volume at high frame rate. This time I look at a different dynamic phenomenon named cyclic hypoxia, which refers to local periodical fluctuations in the tumor between hypoxic and non-hypoxic states. Cyclic hypoxia is associated with increased tumor aggressiveness, resistance to treatments and metastasis [92,93]. Hence, the ability to map and characterize the dynamics of cyclic heterogeneities may eventually contribute to improving treatment outcomes [94]. By taking advantage of the high sensitivity of the transducer to hemoglobin contrast, it was possible to unveil these cyclic events. Notably, the sensitivity of the system is so practical, that periodical sO_2 trends in time can be observed even at a single pixel level without any additional processing (Figure 3-4 in red). Unlike earlier MRI studies of cyclic hypoxia imaging which capitalize on a single cross-section analysis at lower resolution, the proposed method is able to map the distribution of cyclic regions of the entire tumor mass. Moreover, MRI offers contrast which is limited to HbR and may not reflect a "complete" and true oxygenation state such as sO_2.

4. Implementation of a fast scanning optoacoustic tomographic system for whole-body imaging of nano-particles kinetics and biodistribution

4.1. Introduction

Pre-clinical imaging plays an indispensable role in studies of disease pathophysiology and monitoring of treatments. Broad availability of transgenic, knock-out/in mouse models have fostered the adaptation (downscaling) of clinical imaging modalities for small animal imaging applications, including computed tomography (CT), positron emission tomography (PET), single-photon emission computed tomography (SPECT) and magnetic resonance imaging (MRI)[32]. New types of techniques were further developed to provide superior functional and molecular optical contrast relying on fluorescence or optoacoustic (OA) excitation[95,96]. High spatio-temporal resolution is of particular importance for the characterization of toxicity, biodistribution, and metabolic clearance of drugs and contrast agents[97]. To this end, pharmacokinetic studies assisted with targeted contrast agents have greatly facilitated the evaluation of new therapies, accelerated drug discovery and enabled optimizing the administration routes for effective treatment of diseases[98].

In the cancer research field, gold nanoparticles (AuNP) have shown to offer promising theranostic properties[99,100], yet safety concerns related to accumulation and elimination from the body call for a better understanding of their pharmacokinetics and potential toxic effects[101]. Studies involving large numbers of animals are commonly required to assess toxicity of nanoparticles and other exogenously administered agents, turning imaging throughput into a key factor for determining their efficiency[102]. Acceleration of the scanning time is further essential for properly assessing the dynamic bio-distribution of the administered agents. However, total-body scan times of most small animal molecular imaging modalities remain in the 20-30 min range[102,10], greatly hindering their applicability for efficient visualization of biological dynamics at the whole body level.

OA tomography (OAT) has recently matured into a highly versatile molecular imaging technology for preclinical research[103]. It capitalizes on its rich optical contrast and ultrasound-based image formation to resolve a myriad of endogenous and exogenous substances featuring distinctive light

absorption profiles[49]. Small-animal OA scanners based on different acquisition geometries are growingly employed in multitude of biological applications[23,104]. Whole-body tomographic imaging of mice is typically achieved via scanning of ultrasound arrays with the imaging speed and image quality mainly determined by the array configuration and scanning geometry. For example, concave arrays of cylindrically-focused transducers provide cross-sectional (2D) views in real time, but lack the angular coverage required for accurate volumetric (3D) imaging[86,105,106]. Ideally, a large number of pressure signals should be acquired around the imaged object in order to achieve accurate reconstruction of arbitrarily oriented vascular structures[107,108]. Recently, spiral volumetric OA tomography (SVOT) achieved unprecedented image quality by capitalizing on the large angular coverage of a custom-made spherical array[88]. SVOT further enabled scaling the effective temporal resolution to the desired field of view (FOV), greatly improving the throughput capacity for studying biological dynamics and biodistribution of agents. Yet, fast imaging was restricted to relatively small areas[109], hampering the visualization of kinetics at the whole-body level.
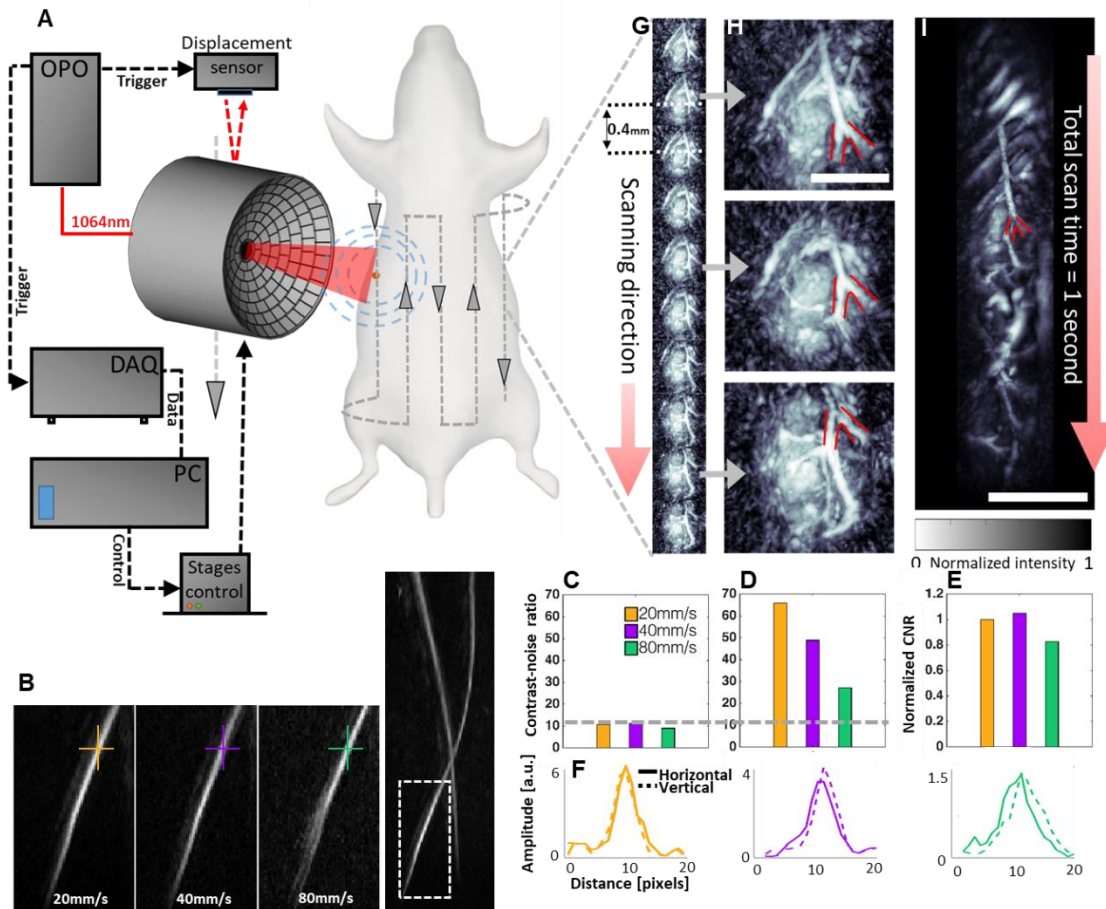
Figure 4-1 The flash scanning optoacoustic tomography (FlashOT) approach. (A) Schematics of the imaging system. The spherical matrix ultrasonic transducer array is translated and rotated 360° around the animal in an overfly scanning mode. Light is transmitted through an aperture in the center of the array. Data acquisition is triggered by the OPO laser source and synchronized with a displacement sensor, which continuously samples the detector position. (B) 3D rendering (maximal intensity projection (MIP)) of a phantom containing two sutures. The effect of the different scanning velocities on the image contrast is shown in the three zoom-ins. (C) Contrast-to-noise ratio (CNR) values of an individual volumetric image frame of the phantom at the three scanning velocities. (D) CNR analysis of a larger compounded volume of a phantom. (E) CNR values after normalizing by the square root of scanning velocity. (F) One-dimensional OA signal profiles along the vertical and horizontal directions, as marked in B. (G) Consecutive OA image volumes acquired from a mouse at vertical scanning velocity of 40 mm/sec, corresponding to 0.4 mm separation between the consecutive frames. (H) Zoom-ins on 3 representative frames from panel G sharing the same anatomical structure (marked in red). (I) Rendering of a larger FOV acquired by a 1 sec vertical sweep of the scanner. The same anatomical structure from H is also visible (marked in red). Scale bar – 1 cm.

4.2. Methods

Experimental setup

The layout of the experimental system is depicted in a. The spherical matrix transducer array (Imasonic SaS, Voray, France) is mounted on motorized stages (IAI Inc., Japan) that are continuously rotated and vertically translated around the sample. The vertical motor provides load capacity of up to 8 kg and can cover a range of up to 15 cm, reaching a scanning velocity of 80 mm/sec. The rotation motor was programmed to complete a full 360° rotation in 15° steps. The sample was placed in a custom-made holder and immersed in a water tank to facilitate efficient propagation and detection of the optoacoustically-generated pressure waves. OA signals were generated with a short-pulsed (<10 ns) laser source (SpitLight, Innolas Laser GmbH, Germany) operating at 1064 nm. The pulse repetition frequency of the laser was set to 100 Hz. Light was guided via a custom-made fiber bundle through a central aperture of the array, thus creating a Gaussian illumination profile with a size of ~10 mm at the FWHM. The per-pulse energy at the fiber output was kept below 15 mJ. The array consists of 256 elements (element area of 9 mm^2) arranged on a hemispherical surface with a radius of 4 cm and 90°angular coverage[110]. The elements have central frequency of 4 MHz and −6 dB bandwidth of ~100%, resulting in nearly isotropic imaging resolution in the 150 µm range [88]. The recorded time-resolved OA signals were digitized at 40 megasamples-per-second by a custom-made data acquisition system (DAQ; Falkenstein Mikrosysteme GmbH, Germany). The precise vertical position of the array was sampled by a sensitive (16 µm resolution, sampling cycle- up to 3 µs) laser displacement sensor (Keyence GmbH, Germany). The DAQ and displacement sensor were simultaneously triggered by the Q-switch output of the laser. The data recorded by all the 256 channels was transmitted to the PC via 1 Gb Ethernet connection for further processing. Data acquisition and motor positioning were computer-controlled using MATLAB (Mathworks, MA, USA).

System Characterization

Calibration of the relative position and orientation of the array with respect to the rotation axis was performed by scanning at multiple angular locations around a single 100 μm polyethylene microsphere (Cospheric Inc, Santa Barbara, USA) embedded in an agar phantom. The exact time delay between the signal acquisition and readings of the laser displacement sensor was calibrated by vertically scanning the same microsphere phantom. To further examine the effect of different scanning velocities on the image quality, I molded an agar phantom containing two black 125 μm diameter surgical sutures (Ethicon, USA) forming a cross shape. The phantom was scanned in continuous motion at velocities of 20, 40 and 80 mm/sec. CNR analysis was performed on individual frames as well as the fully rendered images. Next, vertical and horizontal amplitude profiles along the suture were compared. Data analysis was executed in MATLAB.

Whole-body and biodistribution imaging

All animal *in-vivo* experiments were performed in full compliance with the institutional guidelines of the Helmholtz Center Munich and approved by the government of Upper Bavaria. Hairless NOD.SCID mice (Envigo, Germany) were anesthetized (2% isoflurane (v/v)) and placed in a custom-made holder, which was used to maintain the mice in a stationary position along the center of rotational scanning. The fore and hind paws were attached to the holder during the experiment. The mice were then immersed inside the water tank with their head remaining outside the water. The temperature of the water tank was maintained at 34°C with a feedback-controlled heating stick. A breathing mask with a mouth clamp was used to fix the head in an upright position and supply anesthesia and oxygen. Injections of 150 µl gold nanorods (10x67 nm, SPR=1064 nm, 2.5 mg/mL PBS, Nanopartz Inc., USA) as well as 150 µl of clean PBS for control experiments were done intravenously via a tail-catheter, while the animals were positioned inside the imaging setup.

Image reconstruction and analysis

The time-resolved signals from the 256 detection elements of the array were band-pass filtered (between 0.25–6 MHz) and deconvolved with the impulse response of the array elements. The filtered signals were used to reconstruct volumetric images covering ~1 cm^3 FOV for each laser pulse using GPU implementation of a 3D back-projection algorithm [111]. The image intensity values in the individual reconstructed volumes were normalized with an exponential decay function to compensate for light attenuation with depth. In the next step, the individual volumes were combined together to arrive at the whole-body mouse image. This was particularly done by mapping the transducer elements' coordinates onto volumetric image grid (100 µm pixel resolution) using known positions of the stages retrieved from the displacement sensor's readings. Three-dimensional visualization of the OA images was done with Amira (Visual Sciences Group).

To quantify the changes in biodistribution of contrast agents across different organs, a volumetric mask of each organ was manually delineated. Next, the OA signal amplitude within each organ was quantified. Finally, the ratios between the baseline signal (prior to injection) and the signals at different time points following the injection were calculated. The differences between AuNP injections (n=5 mice) and control PBS injections (n=3 mice) were compared by an unpaired t-test (* $p < 0.05$). Analyses were carried out using MATLAB.

4.3. Results

The flash scanning optoacoustic tomography (FlashOT)

The concept of FlashOT relies on continuous overfly scanning of a spherical matrix array transducer, which captures individual volumetric OA images covering ~1 cm^3 field-of-view after every excitation laser pulse (Figure 4-1a). Following full translation and rotation cycles, the individual volumes are combined together to arrive at the whole-body mouse image. In this way, a 3D total-body scan with ~200 µm spatial resolution is accomplished within 45 seconds without relying on signal averaging (see Methods for details). To investigate the effect of scanning velocity on the resolution and contrast of the images rendered by the system, a sutures phantom was

scanned at velocities spanning 20-80 mm/sec range (Figure 4-1b). As expected, the contrast-to-noise ratio (CNR) of individual frames corresponding to single-shot emission of the laser is similar and independent of the scanning velocity (Figure 4-1c). However, analysis of a larger FOV, reconstructed by combining multiple frames, reveals a decrease in CNR with increasing imaging speed (Figure 4-1d). This is consistent with the fact that the scanning speed influences the effective number of frames used for rendering the compounded image and hence the basic noise level. Dividing the CNR values of the compounded images by the square root of the corresponding scanning velocity renders comparable normalized values (Figure 4-1e). This reveals the effect of noise reduction by frame averaging. Further analysis of the horizontal and vertical amplitude profiles (Figure 4-1f) confirms that the spatial resolution, i.e. the full-width at half maximum (FWHM) of the line profiles, remains unaltered irrespective of the scanning velocity.

Whole-body FlashOT

Figure 4-1g shows a sequence of volumetric frames acquired from a mouse scanned at 40 mm/sec velocity, yielding a separation of 0.4 mm between consecutive frames. Owing to the large FOV of the detector, neighboring frames share overlapping regions and anatomical structures (Figure 4-1h). By adding up frames acquired by a single vertical sweep, a large FOV spanning 4.5 cm length can be readily acquired within just 1 second (Figure 4-1i), where the effect of CNR enhancement via spatial integration of multiple volumetric frames is clearly visible. FlashOT is then capable of full-body imaging in less than 1 minute.
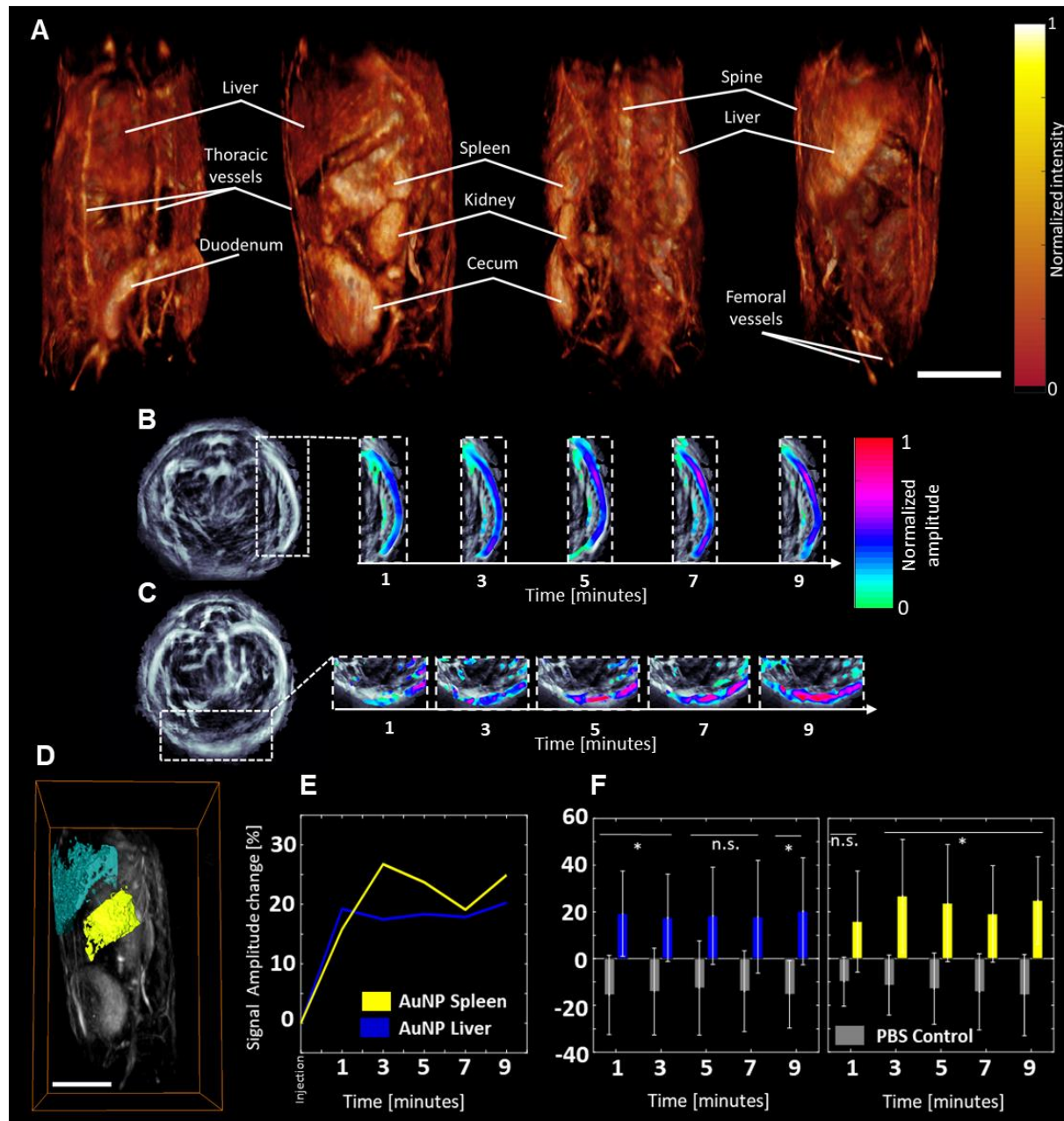
Figure 4-2 Rapid high-resolution 3D anatomical scans and tracking of agent kinetics in whole mice with FlashOT. (A) Whole-body 3D rendering acquired non-invasively from a mouse in-vivo using 40 mm/sec scanning velocity (45 sec total scan time). Maximal intensity projections (MIPs) of the rendered volume are shown from the front, left, back and right views. Selected anatomical structures are labeled with legends. Scale bar – 1 cm. (B) Cross-section images revealing part of the spleen and (C) liver. Zoom-in images display the OA signal amplitude changes over time in response to AuNP administration (with 1 SD). (D) Illustration of the masks for liver and spleen regions used for quantitative biodistribution analyses. Scale bar - 1 cm. (E) Volumetric signal amplitude change as measured over the whole liver and spleen following injection of AuNP (n=5 mice) (F) OA signal variations in the liver and spleen for AuNP versus PBS control injections (n=3 mice with 1 SD, * p < 0.05, n.s. = non-significant).

The maximum intensity projections (MIPs) of the 3D whole-body mouse acquired within a 45 sec scan are shown in Figure 4-2a, offering detailed anatomical information of the thorax and abdominal regions. Main organs like the kidney or the spleen as well as the spine and the surrounding vascular system are clearly discernible with high resolution and contrast. Finer structures such as thoracic and femoral vessels can also be observed. Notably, the full 360° angular coverage of the system facilitates visualization of deep anatomical structures, which are concealed by the MIP views that usually emphasize superficial signals.

Bio-distribution imaging

I subsequently exploited the unique spatio-temporal resolution properties of FlashOT to track fast kinetics and bio-distribution of AuNP at the whole-body scale. Specifically, I focused the analysis on the spleen and liver areas, regarded as the two main sites of AuNP accumulation *in vivo* [101]. Flash scanning at 80 mm/sec allowed for full 360° coverage between the thorax and abdominal regions within ~45 sec scanning time. In this way longitudinal responses in multiple anatomical locations could be simultaneously tracked with high spatial and temporal resolution. Agent accumulation in the spleen and liver are illustrated in Figure 4-2b,c, exhibiting a gradual increase in the local signal amplitudes. The high contrast of the OA signal in these regions was further exploited to segment the spleen and liver, which enabled accurate signal quantification over the entire organs (Figure 4-2d). Such volumetric quantification revealed an early diffusion of AuNP into the organs. The liver accumulation leveled off at 19% above the baseline signal at 1 min after the agent administration, whereas the spleen signal plateaued at 27% above the baseline, 2 min post injection (Figure 4-2e). The control experiments using phosphate buffered saline (PBS) injections (n=3 mice) further confirmed negative to no-response in both liver and spleen (Figure 4-2f).

4.4. Discussion

It was shown that high-resolution whole-body scans can be performed in less than a minute, achieving imaging speed comparable to state-of-the-art anatomical micro-CT scanners[112] and greatly outperforming whole-body scan times of other tomographic imaging techniques such as MRI or PET[113]. Furthermore, when the spherical matrix array is kept at a stationary position, the system can be used for real-time visualization at the whole organ scale at unmatched volumetric frame rates in the kilohertz range[114], thus providing unique scalability across different spatial and temporal dimensions not achievable with other imaging modalities. System characterization suggests that the CNR of the compounded volumes is exclusively dependent upon scanning velocity, which enables scaling the imaging speed to the desired image quality. Note that respiratory motion suppression algorithms[115] and gated acquisition approaches[116,117] may be further employed to enhance image quality.

FlashOT achieved dynamic monitoring of agents in 3D at the whole-body level while simultaneously tracking early accumulation of AuNP across the liver and spleen. AuNP are known to allow for multiplexed targeting, diagnostic and therapeutic functionalities[63] and particularly suited for OAT due to their strong absorption properties[49]. In previous works, OA tracking of AuNP in mice has been accomplished with typical total-body scanning times of several hours[118], or, alternatively, by confining detection to a single cross-section[119,120]. Owing to its fast scanning times, differences in settling times between the two organs could readily be discerned with FlashOT, in agreement with previous reports that employed cross-sectional imaging systems[119]. At present, only micro-CT was shown to render similar throughput, yet it provides significantly lower sensitivity to AuNP and other extrinsic agents[121] and is further afflicted by the use of ionizing radiation.

The capacity for fast tracking of agent kinetics is of particular importance in cancer research, e.g. to assess vascular perfusion function or study accumulation and retention of nano-drug formulations in tumors[33-122]. The true volumetric nature of FlashOT thus has the potential to refine quantitative readings as compared to the commonly employed cross-sectional OA imaging approaches[123]. Note that continuous exposure of AuNP to nanosecond pulsed laser illumination is known to lead to significant OA signal degradation[65], primarily attributed to their poor thermal

stability. This may hamper quantification of time-lapse dynamics and biodistribution[124]. Constant motion of the detection array and light illumination elements in our implementation helps mitigating AuNP photodegradation by reducing light exposure to a single laser pulse or a small number of pulses.

5. Self-gated Respiratory Motion Rejection for Optoacoustic Tomography

5.1. Summary and Author Contribution

This work presents an algorithm solution for self-gated respiratory motion rejection. Self-gated algorithms are commonly based on post-processing of consecutive image reconstructions of the breathing animal, where motion is indicated by changes in position or shape of anatomical structures. In case of my imaging setup, multiple images are acquired across many scanner positions and result in a large dataset. The problem is that such datasets require long data transfer times and moreover, heavy computational resources and time, to reconstruct all images and apply self-gated algorithms. My idea was to examine whether such breathing changes may also be directly observed in the raw time-resolved signals. This is manifested by cross-correlation between consecutive images and grouping into "motion" and "static" groups. Subsequently, the motion frames could be rejected even during scanning, and the relevant raw data could be saved in a manner that would save x50 disk space and require 2% of the computational reconstruction time, comparing to our previous approach.

This work combined animals imaging work, understanding of preclinical image artifacts, and physiology, and algorithm research. The outcome was a straight-forward and useful algorithm which also found a good use in several other projects. All in all, that work may serve as a useful tool for optoacoustic users, across different images systems (as we also demonstrate in this work) and may perhaps be adapted to ultrasound imaging systems.

My contribution to the presented manuscript was the following:

Conception and design: I designed the experiment together with Dr. Dean-Ben (DB) and Dr. Razansky.

Development of methodology: I designed and implemented the motion filtering algorithm.
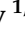
Acquisition of data: I executed the animals imaging with the support of a lab technician Mr. Reiss and Ms. Davoudi.

Analysis and interpretation of data: I reconstructed the data. I executed my algorithm on the data. I designed and implemented the data analysis tools. I implemented the visualization tools.

Writing, review and revision of the manuscript: I drafted the manuscript and collaboratively revised it with all the participants. The same goes for the revisions.

Article

Self-Gated Respiratory Motion Rejection for Optoacoustic Tomography

Avihai Ron [1,2], **Neda Davoudi [3,4]**, **Xosé Luís Deán-Ben [3,5]** and **Daniel Razansky [1,2,3,5,*,†]**

1   Institute for Biological and Medical Imaging, Helmholtz Center Munich, 85764 Neuherberg, Germany
2   Faculty of Medicine, Technical University of Munich, 81765 Munich, Germany
3   Institute for Biomedical Engineering and Department of Information Technology and Electrical Engineering, ETH Zurich, 8093 Zurich, Switzerland
4   Department of Informatics, Technical University of Munich, 85748 Garching, Germany
5   Faculty of Medicine and Institute of Pharmacology and Toxicology, University of Zurich, 8057 Zurich, Switzerland
*   Correspondence: daniel.razansky@uzh.ch; Tel.: +41-44-633-34-29
†   Current Address: Institute for Biomedical Engineering, University of Zurich and ETH Zurich, HIT E42.1, Wolfgang-Pauli-Strasse 27, CH 8093 Zurich, Switzerland.

check for
updates

Abstract: Respiratory motion in living organisms is known to result in image blurring and loss of resolution, chiefly due to the lengthy acquisition times of the corresponding image acquisition methods. Optoacoustic tomography can effectively eliminate *in vivo* motion artifacts due to its inherent capacity for collecting image data from the entire imaged region following a single nanoseconds-duration laser pulse. However, multi-frame image analysis is often essential in applications relying on spectroscopic data acquisition or for scanning-based systems. Thereby, efficient methods to correct for image distortions due to motion are imperative. Herein, we demonstrate that efficient motion rejection in optoacoustic tomography can readily be accomplished by frame clustering during image acquisition, thus averting excessive data acquisition and post-processing. The algorithm's efficiency for two- and three-dimensional imaging was validated with experimental whole-body mouse data acquired by spiral volumetric optoacoustic tomography (SVOT) and full-ring cross-sectional imaging scanners.

Keywords: optoacoustic imaging; photoacoustic tomography; respiratory gating; motion artifacts

1. Introduction

Motion during signal acquisition is known to result in image blurring and can further hinder proper registration of images acquired by different modalities [1–4]. Respiratory motion compensation in tomographic imaging methods is often based on a gated acquisition assisted by physiological triggers, e.g., an electrocardiogram (ECG) signal. In prospective gating, the data is acquired during a limited time window when minimal, or no motion occurs. Alternately, retrospective gating correlates between the acquired images and physiological triggers during post-processing [5]. More advanced retrospective approaches are based on self-gated methods where the physiological trigger is extracted from the image data itself [6–8]. An alternative solution consists in motion tracking of specific points and subsequent correction with rigid-body transformations [9]. In some parts of the body, such as the thoracic region, non-rigid motion is further produced. Thus, more sophisticated models are generally required to estimate and correct for the effects of respiratory motion [10].

High-frame-rate imaging modalities can avoid motion if sub-pixel displacements are produced during the effective image integration time. Particularly, optoacoustic tomography (OAT) can render 2D and 3D images via excitation of an entire volume with a single laser pulse [11]. This corresponds to

an effective integration time in the order of the pulse duration, typically a few nanoseconds. This way, the tissue motion can be "frozen" much more efficiently than most other imaging modalities. OAT has found applicability in biological studies demanding high-frame-rate imaging, such as characterization of cardiac dynamics [12], mapping of neuronal activity [13], monitoring hemodynamic patterns in tumors [14] or visualization of freely-behaving animals [15]. Moreover, real-time imaging has been paramount in the successful translation of OAT to render motion-free images acquired in a handheld mode [16]. While motion correction in OAT might not be relevant for images rendered with a single laser pulse, acquisition of multiple frames is still required in many applications, e.g., for rendering volumetric data from multiple cross-sections or for extending the effective field of view (FOV) of a given imaging system [17]. Multiple frames are also required for multi-spectral optoacoustic tomography (MSOT) applications, where mapping of intrinsic tissue chromophores or extrinsically administered agents is achieved via spectral or temporal unmixing [18–21]. Cardiac and breathing motion could readily be captured by OAT systems running at frame rates of tens of hertz [22,23], and several approaches have been suggested to mitigate motion artefacts in applications involving multi-frame data analysis. For instance, respiratory motion gating was suggested by simultaneously capturing the animal's respiratory waveforms [24]. Motion correction was alternatively performed with 3D rigid-body transformations [25] and with free-form deformation models [26]. Models of body motion have also been suggested for other types of scanning-based systems [27,28]. Additionally, motion suppression could be achieved by reducing the delay between consecutive pulsed light excitations [29,30], which requires dedicated laser systems.

In this work, we demonstrate that motion rejection in OAT can effectively be performed on-the-fly, before image reconstruction. The suggested approach consists in clustering a sequence of OAT frames that employs the raw time-resolved signals without involving computationally and memory extensive post-processing. This represents an important advantage over other known approaches operating in the image domain [31].

2. Materials and Methods

2.1. Pre-Reconstruction Motion Rejection Approach

The algorithm suggested in this work aims at motion rejection in OAT systems based on a multi-frame acquisition of time-resolved pressure signals with transducer arrays. Figure 1a schematically depicts two examples of transducer array configurations for 2D and 3D imaging, which are described in more detail in the following sections. The acquired signals are generally arranged into so-called sinograms, where every sinogram represents a single frame (Figure 1b). At a fixed transducer position, k frames (sinograms) are acquired. These frames consist of matrices with rows representing the m time-samples of each signal and columns corresponding to the n transducer elements (channels) of the array. Step 1 of the algorithm consists in rearranging the k frames of the sequence into columns of a 2D matrix containing m x n rows and k columns, which represent the entire sequence of frames at a fixed transducer position (Figure 1c). In the experiments performed, the number of frames acquired at each array position were chosen to adequately capture a complete breathing cycle. Step 2 of the algorithm consists in calculating the autocorrelation matrix of all pairs of frames (MATLAB (Mathworks Inc, Natick, USA) function 'corrcoef'). An example of the calculated correlation coefficients is displayed in Figure 1d. At a fixed transducer position, time decorrelation is expected to be chiefly affected by respiratory motion. Clustering of frames is subsequently done in Step 3 by applying the second order k-means method to the correlation coefficients matrix (Figure 1e, MATLAB function 'kmeans'). In Step 4, the k frames are then divided into two sets based on predetermined knowledge of the characteristic physiology of the animal under specific anesthesia. As a rule, motion frames are typically fewer than static frames. Notably, when scanning at multiple transducer positions, Steps 1–4 are to be repeated for each transducer position. As an example, Figure 1f displays a comparison of the

3D views of a reconstructed image from a single position of the spherical array, as obtained from the averaged selected-frames and from the averaged rejected-frames.
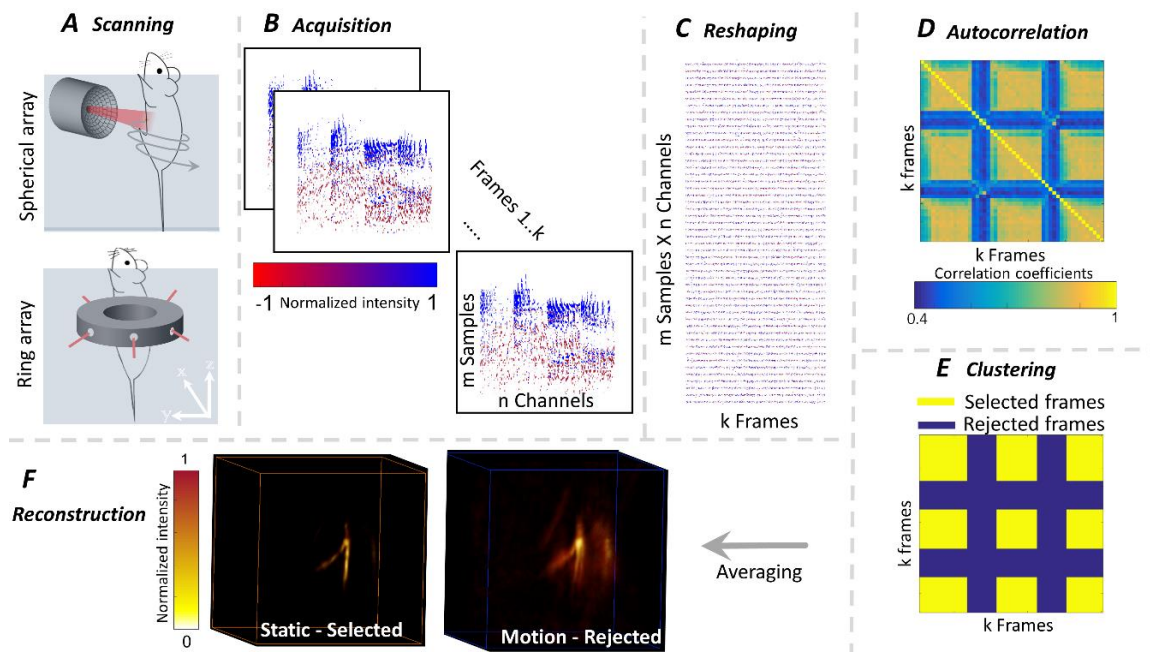

Figure 1. A schematic diagram of the steps involved in the motion rejection algorithm. (**A**) Two- and three-dimensional scanning systems, (top) spiral volumetric optoacoustic tomography (SVOT) based on a spherical array of transducers and (bottom) cross-sectional optoacoustic tomography based on a full-ring array of cylindrically focused transducers. (**B**) Sequence of frames (sinograms) acquired at a single position of the scanner. (**C**) Rearrangement of the data corresponding to the entire sequence into a single matrix. (**D**) Correlation coefficients of the autocorrelation matrix of the columns in (**C**). (**E**) K-means clustering of the correlation coefficients matrix into two groups, namely, selected (static) frames and rejected (motion) frames. (**F**) Volumetric image of a blood vessel reconstructed with data from the selected versus the rejected-frames.

2.2. Spiral Volumetric Optoacoustic Tomography

The spiral volumetric optoacoustic tomography (SVOT) scanner is schematically depicted in Figure 1a (top). A detailed description of the system is available elsewhere [32]. Briefly, a spherical ultrasound array of piezocomposite elements (Imasonics SaS, Voray, France) is mounted on motorized rotating and translating stages and scanned around the animal following a spiral trajectory. The array consists of 256 elements with a central frequency of 4 MHz and −6 dB bandwidth of ~100%, arranged in a hemispherical surface with angular coverage of 90°. The excitation light beam is guided via a fiber bundle (CeramOptec GmbH, Bonn, Germany) through a cylindrical aperture in the center of the sphere. SVOT enables imaging of the entire mouse with a nearly isotropic 3D spatial resolution in the 200 μm range [31]. In the experiments, light excitation was provided with a short-pulsed laser (<10 ns duration pulses with 25 mJ per-pulse energy and up to 100 Hz pulse repetition frequency) based on an optical parametric oscillator (OPO) crystal (Innolas GmbH, Krailling, Germany). The pulse repetition frequency of the laser was set to 25 Hz and the wavelength was maintained at 800 nm, corresponding to the isosbestic point of hemoglobin. The array was scanned for 17 angular positions separated by 15° (total angular coverage in the azimuthal direction of 240°) and for 30 vertical positions separated by 2 mm (total scanning length of 58 mm, a full-body scan requires approximately 10 min). 50 frames were captured for each position of the array, for which all signals were simultaneously digitized at 40 megasamples per second with a custom-made data acquisition system (DAQ, Falkenstein

Mikrosysteme GmbH, Taufkirchen, Germany) triggered with the Q-switch output of the laser. The acquired data was eventually transmitted to a PC via Ethernet.

2.3. Cross-Sectional Optoacoustic Tomography with a Ring Array

The system layout is depicted in Figure 1a (bottom) while its detailed description is available in [33]. Briefly, the ultrasound array (Imasonics SaS, Voray, France) consists of an 80 mm diameter ring having 512 ultrasound individual detection elements with 5 MHz central frequency and −6 dB bandwidth of ~80%. Each element is cylindrically focused at a distance of 38 mm to selectively capture signals from the imaged cross-section. In the experiments, light excitation was provided by a short-pulsed (<10 ns duration pulses at a wavelength of 1064 nm with ~100 mJ per-pulse energy and 15 Hz pulse repetition frequency) Nd:YAG laser (Spectra Physics, Santa Clara, California). The laser beam was guided with a fiber bundle (CeramOptec GmbH, Bonn, Germany) having 12 output arms placed around the circumference of the ring transducer with an angular separation of 60° between the arms. Much like the SVOT system, signals detected by all the array elements were simultaneously digitized at 40 megasamples per second using custom-made DAQ (Falkenstein Mikrosysteme GmbH, Taufkirchen, Germany), triggered with the Q-switch output of the laser. The data was transmitted to a PC via Ethernet. In total, 100 frames were recorded with the array positioned at two distinct regions of the mouse.

2.4. Image Reconstruction and Processing

In both scanning systems, the acquired signals were band-pass filtered (cut-off frequencies 0.25–6 MHz for SVOT and 0.5–8 MHz for cross-sectional OAT) and deconvolved with the impulse response of the array elements before reconstruction. For SVOT, tomographic reconstructions of single volumes ($15 \times 15 \times 15$ mm^3) for each scanning position of the spherical array transducer were done using a 3D back-projection-based algorithm [34,35]. Volumetric images reconstructed at every transducer position were stitched together to render images from a larger field of view (whole-body scale). For cross-sectional OAT, the same back-projection algorithm was modified to account for the heterogeneous distribution of the speed of sound in the mouse versus the coupling medium (water) [36]. For this, an initial image was first reconstructed by considering a uniform speed of sound corresponding to the speed of sound in water (determined from the measured water temperature). The animal's surface was then manually segmented, and the reconstruction was fine-tuned by assigning a different speed of sound to the segmented tissue volume in order to optimize image quality. The processing was executed with a self-developed MATLAB code. Universal image quality index (QI) was calculated for the resulting images. QI is an objective image quality index that combines three models: loss of correlation, luminance distortion and contrast distortion—a detailed description and efficient MATLAB implementation was reported in [37].

2.5. Mouse Experiments

All *in-vivo* animal experiments were performed in full compliance with the institutional guidelines of the Helmholtz Center Munich and with approval by the Government District of Upper Bavaria. Hairless NOD.SCID mice (Envigo, Rossdorf, Germany) were anesthetized with isoflurane. For both imaging systems, a custom-made holder was used to vertically fix the mice in a stationary position with fore and hind paws attached to the holder during the experiments. The mice were immersed inside the water tank with the animal head being kept above water. The temperature of the water tank was maintained at 34 °C with a feedback controlled heating stick. A breathing mask with a mouth clamp was used to fix the head in an upright position and to supply anesthesia and oxygen. During measurement, the anesthesia level was kept at ~2% isoflurane.

3. Results

3.1. Spiral Volumetric Optoacoustic Tomography

A whole-body (neck to hind paws) SVOT image, reconstructed using the frames selected with the proposed motion rejection approach, is displayed in Figure 2a. In these experiments, an average of 32% of frames were rejected per transducer position. The effectiveness of the motion rejection approach is demonstrated by analyzing three specific regions (dashed squares in Figure 2a). Specifically, we compare the image combining all the frames, with the one obtained by averaging the selected (static) frames as well as the image obtained by averaging the rejected (motion) frames. Note that the red square partially captures the thoracic region. It can be observed that a small vessel, clearly visible in the image rendered from the selected frames (Figure 2b, red arrow), cannot be resolved in the image reconstructed using all the frames. Furthermore, the former image features a clear motion artifact in the form of a 'double vessel' (red arrow), thus concealing the small vessel. The green square captures the region around the liver. A vertical vessel appears regular and complete in the selected-frames image (red arrow), whereas the same vessel appears disrupted in the all-frames image. Also here, the rejected-frames image discloses an artifact responsible for distorting the all-frames image. Finally, the blue square captures part of the abdomen. Clearly, small vessels are better resolved in the selected-frames image (red arrows). Notably, different structures appear to be blurred (yellow arrows) in the rejected-frames images with respect to the selected-frames images. A comparison between amplitude profiles of structures labeled by dashed yellow lines in Figure 2b further emphasizes the effectiveness of the motion rejection algorithm (Figure 2c) with the signal amplitude typically improved by 10% to 30% in the selected-frames images. Likewise, fine details appear more prominent in the selected-frames images, which is evinced by additional, fine peaks in the amplitudes profiles.
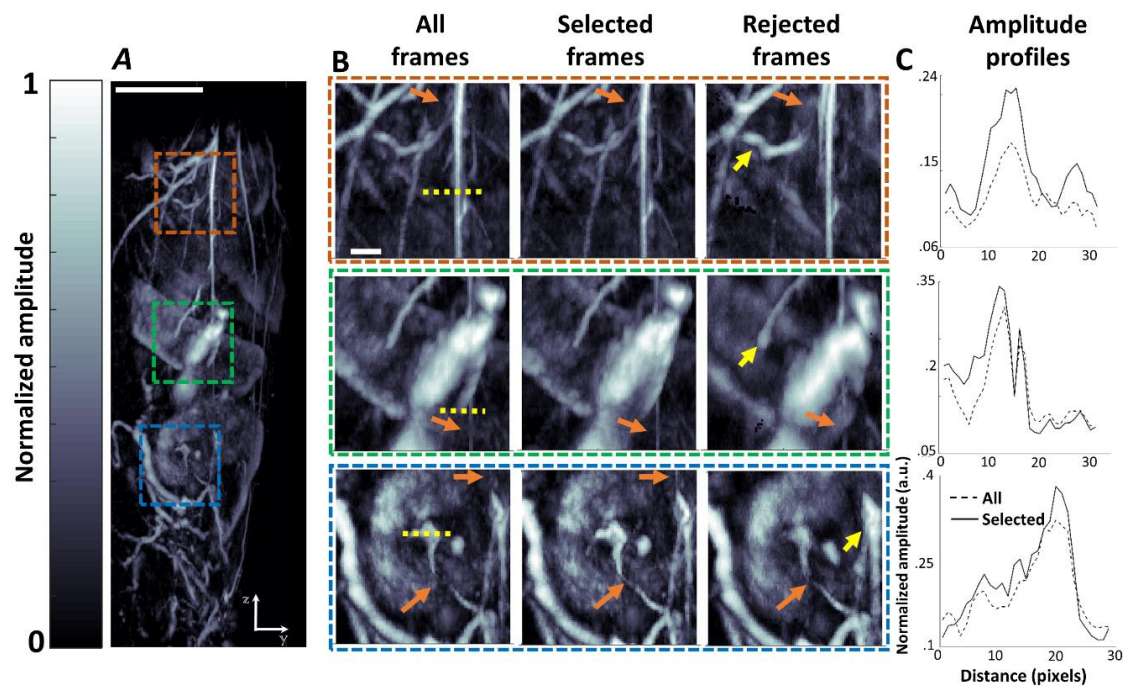
Figure 2. Motion rejection results for spiral volumetric optoacoustic tomography (SVOT). (**A**) Sagittal maximal intensity projection (MIP) of a volumetric image of the mouse reconstructed with the selected-frames (scale bar—1 cm). (**B**) Zoom-in of three regions marked in red, green, blue, respectively, in (**A**). Each image is reconstructed with (left) all-frames, (center) the selected (static) frames (right) the rejected (motion) frames (scale bar—1 mm). Structural differences are marked (yellow and red arrows). (**C**) Amplitude profiles marked in b (yellow dashed lines) for images reconstructed from all the frames (dashed lines) versus selected frames (solid lines).

3.2. Cross-Sectional Optoacoustic Tomography

Effectiveness of the algorithm in cross-sectional OAT was tested by comparing the selected- and rejected-frames images taken from two distinct regions of the animal (Figure 3a). Between 20% and 31% of the frames were rejected in the top and bottom cross-sections, respectively. The rejected-frames images reveal smearing artifacts caused by a breathing motion that are evident across the entire mouse cross-section. Fine structures (red arrows) within the abdominal space appear blurred in the rejected-frames image. Moreover, some superficial structures seem to be artificially 'doubled' (yellow arrows) in the rejected-frames images. Minor differences were observed in the all-frames images (data not shown) with respect to the selected-frames images. Likewise, amplitude profiles from selected structures (dashed yellow line in Figure 3a) are increased by ~10% in the selected-frames images (Figure 3b). The calculated QI clearly reveals distortions at the boundaries of major structures, located mostly superficially (Figure 3c).
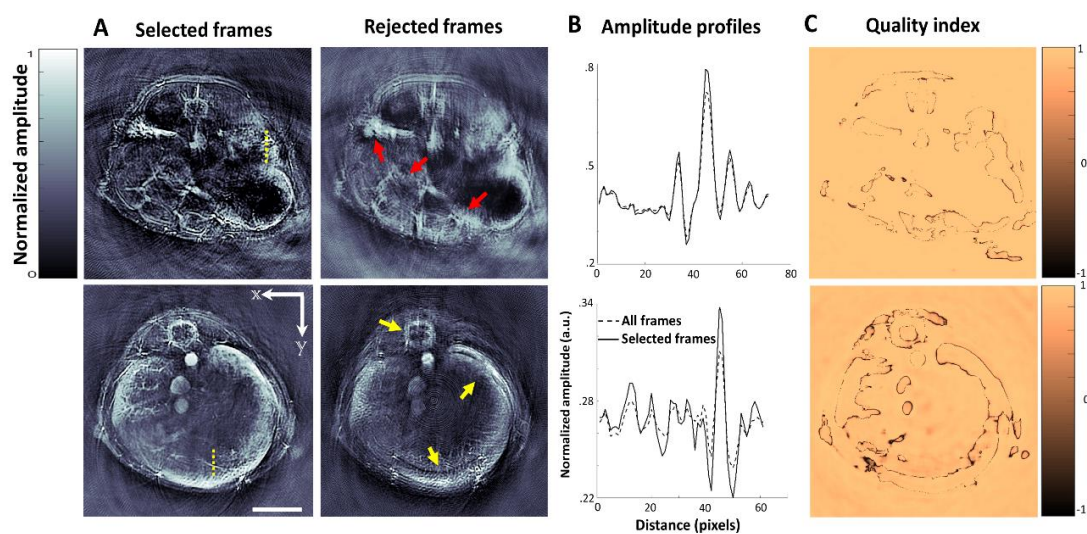

Figure 3. Motion rejection results for cross-sectional imaging with the ring array system. (**A**) Reconstructed transverse slices of a mouse for two different locations rendered by considering the selected (left) versus rejected (right) frames (scale bar—1 cm). Distorted structures are marked (red and yellow arrows). (**B**) Amplitude profiles (of yellow dashed lines in (**A**)) for the images rendered with all (dashed line) versus selected (solid line) frames. (**C**) Distortion-based QI of the difference between the selected- and all-frames images (1 = high similarity; −1 = low similarity).

4. Discussion

The presented results demonstrate that motion rejection in OAT can effectively be accomplished prior to image reconstruction. This represents a significant advantage with respect to previously reported motion rejection approaches based on auto-correlation of a sequence of reconstructed images [31], which are afflicted with excessive memory and post-processing requirements. The suggested method was successfully validated with data acquired by two- and three-dimensional imaging systems. However, motion rejection was more effective in the case of volumetric SVOT scans. In particular, it benefited from both amplitude increase of 10% to 30% and improvement in the visibility of fine details, whereas images from the cross-sectional imaging system yielded a lower amplitude increase (~10%) and minor improvement in the visibility of structures. The reason behind the reduced performance of motion rejection in cross-sectional imaging may be ascribed to the fact that breathing-associated movements are not limited to a single plane, while in-plane motion is mainly detected in the signals. Yet, although the differences between selected- and all-frames cross-sectional images were minor, it was possible to quantify them by utilizing a QI based distortion measures. Notably, such distortion artifacts affect almost exclusively the edges of large structures. In spite of the fact that standard frame averaging in

cross-sectional imaging may yield qualitatively comparable results, reliable rejection of 20% to 31% motion-affected frames by the algorithm may turn crucial for quantitative analyses of high resolution data, e.g., involving spectral unmixing of fine structures.

It is also important to take into account that breathing characteristics may differ from one animal to another due to age, health, size, sex or strain. All these factors affect the resilience of the animal to the experimental setup, the feasible depth of anesthesia and the overall duration of the experiment [38]. It was previously reported that mice under 2% isoflurane anesthesia have an average respiratory rate of 44 ± 9 breaths/min [39], where the breathing rhythm is characterized by pauses between breaths longer than the breaths themselves. As a result, the majority of the frames are static, i.e., not affected by motion. Herein, we relied on such prior knowledge of the characteristic respiratory rate and breathing rhythm to establish a rejection criterion for the clustered motion (rejected) frames. Likewise, other criteria independent of these factors may alternatively be implemented.

In conclusion, the developed motion rejection methodology can benefit numerous optoacoustic imaging methods relying on multi-frame image analysis, such as scanning-based tomography or spectroscopic imaging systems like the MSOT. It may also find applicability in handheld clinical imaging [40,41], where motion can hinder accurate signal quantification and interpretation of longitudinal and spectroscopic data.

Author Contributions: Conceptualization, A.R., X.L.D.-B. and D.R.; methodology, A.R.; software, A.R.; validation, A.R. and N.D.; formal analysis, A.R.; investigation, A.R.; resources, D.R.; data curation, A.R. and X.L.D.-B.; writing—original draft preparation, A.R., X.L.D.-B. and D.R.; writing—review and editing, A.R., X.L.D.-B. and D.R.; visualization, A.R.; supervision, D.R.; project administration, D.R.; funding acquisition, D.R.

Conflicts of Interest: The authors declare no conflict of interest.

References

1. Nehmeh, S.A.; Erdi, Y.E. Effect of respiratory gating on quantifying PET images of lung cancer. *J. Nucl. Med.* **2002**, *43*, 876–881.
2. Chi, P.-C.M.; Mawlawi, O. Effects of respiration-averaged computed tomography on positron emission tomography/computed tomography quantification and its potential impact on gross tumor volume delineation. *Int. J. Radiat. Oncol. Biol. Phys.* **2008**, *71*, 890–899. [CrossRef] [PubMed]
3. Liu, C.; Pierce, L.A. II The impact of respiratory motion on tumor quantification and delineation in static PET/CT imaging. *Phys. Med. Biol.* **2009**, *54*, 7345. [CrossRef] [PubMed]
4. Nehrke, K.; Bornert, P. Free-breathing cardiac MR imaging: Study of implications of respiratory motion—Initial results. *Radiology* **2001**, *220*, 810–815. [CrossRef] [PubMed]
5. Heijman, E.; de Graaf, W. Comparison between prospective and retrospective triggering for mouse cardiac MRI. *NMR Biomed.* **2007**, *20*, 439–447. [CrossRef] [PubMed]
6. Zaitsev, M.; Maclaren, J. Motion artifacts in MRI: A complex problem with many partial solutions. *J. Magn. Reson. Imaging* **2015**, *42*, 887–901. [CrossRef] [PubMed]
7. Sureshbabu, W.; Mawlawi, O. PET/CT imaging artifacts. *J. Nucl. Med. Technol.* **2005**, *33*, 156–161.
8. Nehmeh, S.A.; Erdi, Y.E. *Respiratory Motion in Positron Emission Tomography/Computed Tomography: A Review*; Elsevier: Amsterdam, The Netherlands, 2008; pp. 167–176.
9. Maclaren, J.; Herbst, M. Prospective motion correction in brain imaging: A review. *Magn. Reson. Med.* **2013**, *69*, 621–636. [CrossRef]
10. McClelland, J.R.; Hawkes, D.J. Respiratory motion models: A review. *Med. Image Anal.* **2013**, *17*, 19–42. [CrossRef]
11. Deán-Ben, X.; Gottschalk, S. Advanced optoacoustic methods for multiscale imaging of in vivo dynamics. *Chem. Soc. Rev.* **2017**, *46*, 2158–2198. [CrossRef]

12. Lin, H.-C.A.; Déan-Ben, X.L. Characterization of Cardiac Dynamics in an Acute Myocardial Infarction Model by Four-Dimensional Optoacoustic and Magnetic Resonance Imaging. *Theranostics* **2017**, *7*, 4470. [CrossRef] [PubMed]

13. Gottschalk, S.; Degtyaruk, O. Rapid volumetric optoacoustic imaging of neural dynamics across the mouse brain. *Nat. Biomed. Eng.* **2019**, *3*, 392–401. [CrossRef] [PubMed]

14. Ron, A.; Déan-Ben, X.L. Volumetric optoacoustic imaging unveils high-resolution patterns of acute and cyclic hypoxia in a murine model of breast cancer. *Cancer Res.* **2019**. [CrossRef] [PubMed]

15. Özbek, A.; Déan-Ben, X.L. Optoacoustic imaging at kilohertz volumetric frame rates. *Optica* **2018**, *5*, 857–863. [CrossRef]

16. Neuschmelting, V.; Burton, N.C. Performance of a multispectral optoacoustic tomography (MSOT) system equipped with 2D vs. 3D handheld probes for potential clinical translation. *Photoacoustics* **2016**, *4*, 1–10. [CrossRef] [PubMed]

17. Déan-Ben, X.L.; López-Schier, H. Optoacoustic micro-tomography at 100 volumes per second. *Sci. Rep.* **2017**, *7*, 6850. [CrossRef] [PubMed]

18. Ron, A.; Déan-Ben, X.L. Characterization of Brown Adipose Tissue in a Diabetic Mouse Model with Spiral Volumetric Optoacoustic Tomography. *Mol. Imaging Biol.* **2018**. [CrossRef] [PubMed]

19. Taruttis, A.; Ntziachristos, V. Advances in real-time multispectral optoacoustic imaging and its applications. *Nat. Photonics* **2015**, *9*, 219. [CrossRef]

20. Déan-Ben, X.L.; Stiel, A.C. Light fluence normalization in turbid tissues via temporally unmixed multispectral optoacoustic tomography. *Opt. Lett.* **2015**, *40*, 4691–4694. [CrossRef]

21. Yao, J.; Kaberniuk, A.A. Multiscale photoacoustic tomography using reversibly switchable bacterial phytochrome as a near-infrared photochromic probe. *Nat. Methods* **2016**, *13*, 67. [CrossRef]

22. Wang, L.; Maslov, K.I. Video-rate functional photoacoustic microscopy at depths. *J. Biomed. Opt.* **2012**, *17*, 106007. [CrossRef] [PubMed]

23. Taruttis, A.; Claussen, J. Motion clustering for deblurring multispectral optoacoustic tomography images of the mouse heart. *J. Biomed. Opt.* **2012**, *17*, 016009. [CrossRef] [PubMed]

24. Xia, J.; Chen, W. Retrospective respiration-gated whole-body photoacoustic computed tomography of mice. *J. Biomed. Opt.* **2014**, *19*, 016003. [CrossRef] [PubMed]

25. Gottschalk, S.; Fehm, T.F. Correlation between volumetric oxygenation responses and electrophysiology identifies deep thalamocortical activity during epileptic seizures. *Neurophotonics* **2016**, *4*, 011007. [CrossRef]

26. Toi, M.; Asao, Y. Visualization of tumor-related blood vessels in human breast by photoacoustic imaging system with a hemispherical detector array. *Sci. Rep.* **2017**, *7*, 41970. [CrossRef] [PubMed]

27. Schwarz, M.; Garzorz-Stark, N. Motion correction in optoacoustic mesoscopy. *Sci. Rep.* **2017**, *7*, 10386. [CrossRef] [PubMed]

28. Chung, J.; Nguyen, L. Motion estimation and correction in photoacoustic tomographic reconstruction. *SIAM J. Imaging Sci.* **2017**, *10*, 216–242. [CrossRef]

29. Déan-Ben, X.L.; Bay, E. Functional optoacoustic imaging of moving objects using microsecond-delay acquisition of multispectral three-dimensional tomographic data. *Sci. Rep.* **2014**, *4*, 5878. [CrossRef]

30. Märk, J.; Wagener, A. Photoacoustic pump-probe tomography of fluorophores in vivo using interleaved image acquisition for motion suppression. *Sci. Rep.* **2017**, *7*, 40496. [CrossRef]

31. Fehm, T.F.; Déan-Ben, X.L. In vivo whole-body optoacoustic scanner with real-time volumetric imaging capacity. *Optica* **2016**, *3*, 1153–1159. [CrossRef]

32. Déan-Ben, X.L.; Fehm, T.F. Spiral volumetric optoacoustic tomography visualizes multi-scale dynamics in mice. *Light Sci. Appl.* **2017**, *6*, e16247. [CrossRef] [PubMed]

33. Merčep, E.; Herraiz, J.L. Transmission–reflection optoacoustic ultrasound (TROPUS) computed tomography of small animals. *Light Sci. Appl.* **2019**, *8*, 18. [CrossRef] [PubMed]

34. Xu, M.; Wang, L.V. Universal back-projection algorithm for photoacoustic computed tomography. *Phys. Rev. E* **2005**, *71*, 016706. [CrossRef] [PubMed]

35. Ozbek, A.; Déan-Ben, X. *Realtime Parallel Back-Projection Algorithm for Three-Dimensional Optoacoustic Imaging Devices*; Optical Society of America: Washington, DC, USA, 2013; p. 88000I.

36. Déan-Ben, X.L.; Özbek, A. Accounting for speed of sound variations in volumetric hand-held optoacoustic imaging. *Front. Optoelectron.* **2017**, *10*, 280–286. [CrossRef]

37. Wang, Z.; Bovik, A.C. A universal image quality index. *IEEE Signal Process. Lett.* **2002**, *9*, 81–84. [CrossRef]
38. Gargiulo, S.; Greco, A. Mice anesthesia, analgesia, and care, Part II: Anesthetic considerations in preclinical imaging studies. *ILAR J.* **2012**, *53*, E70–E81. [CrossRef]
39. Kober, F.; Iltis, I. Cine-MRI assessment of cardiac function in mice anesthetized with ketamine/xylazine and isoflurane. *Magn. Reson. Mater. Phys. Biol. Med.* **2004**, *17*, 157–161. [CrossRef]
40. Diot, G.; Metz, S. Multi-Spectral Optoacoustic Tomography (MSOT) of human breast cancer. *Clin. Cancer Res.* **2017**, *23*, 6912–6922. [CrossRef]
41. Reber, J.; Willershäuser, M. Non-invasive Measurement of Brown Fat Metabolism Based on Optoacoustic Imaging of Hemoglobin Gradients. *Cell Metab.* **2018**, *27*, 689–701. [CrossRef]

6. Characterization of brown adipose tissue in a diabetic mouse model with spiral volumetric optoacoustic tomography

6.1. Summary and Author Contribution

The motivation of this study was to exploit the high hemoglobin sensitivity and volumetric nature of the spherical detector, to advance the level of visualization and quantification of metabolism related anatomy and physiological parameters with optoacoustic. This work is based on previous studies, suggesting multispectral optoacoustic tomography as a new tool capable of differentiating healthy and diabetic BAT by observing hemoglobin gradients and microvasculature density in cross-sectional (2D) views. Subsequently, this work demonstrated improved characterization of BAT, with superior visualization in 3D and better quantification of hemodynamic parameters, which result in improved separation between healthy and diabetic mice.

My contribution to the presented manuscript was the following:

Conception and design: I designed the experiment together with Dr. Dean-Ben (DB), Dr. Reber and Dr. Razansky.

Development of methodology: I modified the scanning system (setting up motors and controllers, writing the scanning code, designing designated animal holders, optimizing optics (e.g. laser alignment, fiber polishing)) together with DB.

Acquisition of data: I executed the animals imaging with the support of a lab technician Mr. Reiss.

Analysis and interpretation of data: I engineered the BP reconstruction code together with DB. I designed and implemented the complete post analysis code and statistical analysis. I designed and implemented the segmentation algorithm. I implemented the visualization tools.

Writing, review and revision of the manuscript: I drafted the manuscript and collaboratively revised it with all the participants. The same goes for the revisions.

BRIEF ARTICLE

Characterization of Brown Adipose Tissue in a Diabetic Mouse Model with Spiral Volumetric Optoacoustic Tomography

Avihai Ron, Xosé Luís Deán-Ben, Josephine Reber, Vasilis Ntziachristos, Daniel Razansky

Institute for Biological and Medical Imaging, Technical University of Munich and Helmholtz Center Munich, Munich, Germany

Abstract

Purpose: Diabetes is associated with a deterioration of the microvasculature in brown adipose tissue (BAT) and with a decrease in its metabolic activity. Multispectral optoacoustic tomography has been recently proposed as a new tool capable of differentiating healthy and diabetic BAT by observing hemoglobin gradients and microvasculature density in cross-sectional (2D) views. We report on the use of spiral volumetric optoacoustic tomography (SVOT) for an improved characterization of BAT.

Procedures: A streptozotocin-induced diabetes model and control mice were scanned with SVOT. Volumetric oxygen saturation (sO_2) as well as total blood volume (TBV) in the subcutaneous interscapular BAT (iBAT) was quantified. Segmentation further enabled separating feeding and draining vessels from the BAT anatomical structure.

Results: Scanning revealed a 46 % decrease in TBV and a 25 % decrease in sO_2 in the diabetic iBAT with respect to the healthy control.

Conclusions: These results suggest that SVOT may serve as an effective tool for studying the effects of diabetes on BAT. The volumetric optoacoustic imaging probe used for the SVOT scans can be operated in a handheld mode, thus potentially providing a clinical translation route for BAT-related studies with this imaging technology.

Key words: Optoacoustic, Brown fat, Metabolism, Hemoglobin, Oxygen saturation, Adipose tissue, Angiopathy

Introduction

Brown adipose tissue (BAT) appears to provide a self-defense mechanism against diabetes and has been shown to offer therapeutic potential against this widespread disease [1]. BAT has long been recognized to play a role in temperature control in newborns. Yet, recent evidence suggests that it is also present and active in adults [2], primarily located behind the muscles of the lower neck and collarbone [3]. In diabetic patients, a decrease in the metabolic activity of BAT has been observed [4], which appears to correlate with angiopathy [5]. Mouse models have shown promise in facilitating studies into the BAT metabolism [6], further supported by wide availability of the diabetes models [7, 8]. In mice, BAT is spread across several locations, primarily in the cervical-thoracic region, known as the subcutaneous interscapular BAT (iBAT).

Accurate non-invasive characterization of BAT and its metabolic activity may greatly facilitate development of novel strategies to treat diabetes. The presence of BAT and

its metabolism can be characterized by glucose uptake rate as measured by 2-deoxy-2-[^{18}F]fluoro -D-glucose [9–11], translocator proteins [12], or cannabinoid receptor-1 [13] tracers in positron emission tomography. The use of ionizing radiation however impedes longitudinal clinical studies while further involving introduction of exogenous agents. On the other hand, tissue blood flow can be estimated by contrast-enhanced ultrasound [14] and near-infrared fluorescent imaging [15], thus providing an indirect measure of metabolic activity. Another potential indicator of such activity is elevated tissue temperature, which can only be measured superficially with infrared imaging [16]. The limitations of existing imaging approaches urge therefore for the development of new approaches for the characterization of BAT and its metabolic activity.

Multispectral optoacoustic tomography (MSOT) has previously shown promise for non-invasive label-free measurements of iBAT metabolism and differentiation between its diabetic and healthy states by imaging of hemoglobin gradients and blood volume [17]. MSOT-based detection of development of beige adipocytes during adrenergic stimulation was further demonstrated using expression of near-infrared fluorescence protein iRFP720 [18]. Spiral volumetric optoacoustic tomography (SVOT) has recently offered unprecedented capabilities for three-dimensional (3D) characterization of microvascular structures and oxygen saturation (sO$_2$) quantification in whole mice [19]. Here, we investigate the SVOT capabilities for the 3D visualization and characterization of entire iBAT depots in healthy and diabetic mice.

Materials and Methods

The SVOT Imaging System

A schematic representation of the SVOT scanning procedure is provided in Fig. 1a with a more detailed description available elsewhere [19]. Briefly, a spherical ultrasound array of piezocomposite elements is mounted on motorized rotating and translating stages and scanned around the mouse following a helical (spiral) trajectory. The array consists of 256 elements with a central frequency of 4 MHz and – 6 dB bandwidth of ~ 100 % distributed on a spherical surface with 40 mm radius and 90° angular coverage. Optical excitation is provided by short-pulsed laser light (10 ns duration pulses with 25 mJ per-pulse energy and up to 100 Hz pulse repetition frequency) tunable in the near-infrared range (700–900 nm). Light is guided via a fiber bundle through a central aperture of the array. SVOT enables imaging the entire mouse with a nearly isotropic 3D spatial resolution in the 300 μm range [20].

In vivo Experiments

Male BALB/c mice (6–8 weeks old, Envigo Laboratories, Germany) were kept at 24 ± 1 °C on a 12:12-h light-dark cycle and fed with standard rodent diet (Altromin 1314, Altromin Spezialfutter GmbH & Co, Germany) with free access to water. Diabetes was induced with a single intraperitoneal injection of streptozotocin (Sigma, Germany) at 150 mg/kg body weight after 4–6 h fasting. Blood glucose levels (350–500 mg/dl) were measured on the same day when the SVOT scanning was performed, 7–14 days after induction of diabetes. Prior to in vivo imaging, the mice were anesthetized with isoflurane, placed in a custom-made animal holder, and immersed in a water tank (water temperature 33 °C) to facilitate efficient propagation and detection of the optoacoustically generated pressure waves. The head of the animals was kept above water, and a mask was placed over the mouth and nose for the administration of anesthesia and oxygen. All in vivo mouse experiments were performed in full compliance with the institutional guidelines of the Helmholtz Center Munich and with approval from the Government District of Upper Bavaria.

Data Analysis

SVOT imaging of mice was performed in a localized region surrounding the iBAT. The tomographic optoacoustic data was acquired at four wavelengths, namely, 730, 760, 800, and 850 nm. Tomographic reconstructions of single volumes ($15 \times 15 \times 15$ mm^3) for each scanning position of the spherical array transducer were done using a 3D back-projection-based algorithm [21, 22] implemented in MATLAB (MathWorks, USA). Volumetric image frames associated with breathing motion were identified and removed for an enhanced imaging performance, as previously reported [20]. All remaining frames were subsequently averaged and the resulting images were corrected for exponential light attenuation with depth according to $e^{-\sqrt{3\mu_a(\lambda)(\mu_a(\lambda)+\mu'_s(\lambda))}z}$, where average values for the wavelength-dependent reduced scattering $\mu'_s(\lambda)$ and absorption $\mu_a(\lambda)$ coefficients in adipose tissue were taken from literature [23]. All individual reconstructions were then combined based on the known positions of the ultrasound array during the SVOT scan [20]. Microvasculature density was estimated from the total blood volume (TBV) in the iBAT region, which was calculated from the voxel intensity values of the reconstructed images at 800 nm excitation (isosbestic point of hemoglobin). A standard linear spectral unmixing algorithm [24] was applied to the multispectral data on a voxel-by-voxel basis to retrieve the bio-distribution of HbO$_2$ and Hb. The blood oxygen saturation (sO$_2$) was then calculated as the ratio between the HbO$_2$ and the sum of the HbO$_2$ and Hb signals. A Mann-Whitney test was used for statistical comparisons between the groups. All processing procedures were performed in MATLAB and the final 3D images were exported into Amira (Thermo Fisher Scientific, USA) for better visualization.
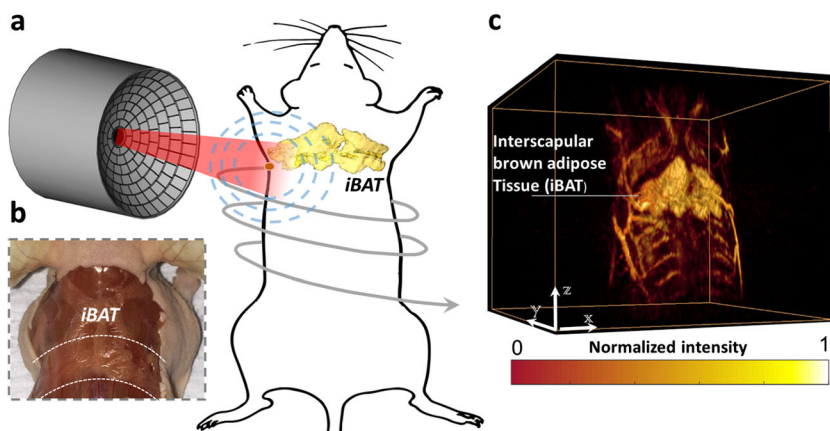
Fig. 1.   **a** Schematics of the SVOT system. Light is emitted from the center of the spherical transducer array, which detects the optoacoustic signal. The transducer array rotates in a spiral motion around the animal. **b** A photo of the skin of the lower neck region removed, exposing the iBAT. **c** A 3D representation of a SVOT scan of the lower neck region, clearly showing the iBAT in a mouse.

Data Availability

The datasets used and/or analyzed during the current study are available from the corresponding author on reasonable request.

Results

The anatomical position of iBAT can be clearly discerned within the interscapular region (Fig. 1b) in the whole-body SVOT images taken at 800 nm (Fig. 1c). This large-area scan was performed with 10 angular positions (10° step) and 8 translational positions (2 mm step) of the array, resulting in a highly detailed (200 μm spatial resolution) 3D image of the entire thoracic region of the mouse. The high contrast generated by the system from the iBAT is primarily associated with the rich and dense microvasculature of this tissue [25].

The iBAT regions of the healthy ($n = 3$) and the streptozotocin-induced, diabetic mice ($n = 3$) were then scanned multispectrally. The iBAT can be easily spotted anatomically in the images taken at the isosbestic hemoglobin wavelength of 800 nm, effectively representing the total blood volume (TBV) distribution (Fig. 2a). The main draining vein from the iBAT, the so-called Sulzer vein (SV), is also visible. The expected deterioration of the microvasculature density in the diabetic iBAT is consistent with the observed 46 % lower TBV value as compared to the healthy control (Fig. 2b).

Spectral unmixing of the multiwavelength image data further revealed the sO_2 distribution in the iBAT (Fig. 3.a). To quantify the TBV and sO_2 values in the iBAT independently from the large vessels, a global threshold for the sO_2 map was set automatically by using the Otsu's method [26]. This threshold value of 60 % sO_2 was applied to the sO_2 map in order to set iBAT apart from the surrounding large vessels (Fig. 3.b). When comparing with

average oxygenation levels of the healthy iBAT ($sO_2 = 36$ %), the decreased metabolic activity in the diabetic iBAT results in reduced sO_2 levels of $sO_2 = 27$ % (Fig. 3.c). The separation between the mean sO_2 values for the healthy and diabetic groups is also evident based on individual animal data (Suppl. Fig. S1). The large vessels, on the other hand, show slightly decreased average oxygenation levels in diabetic mice ($sO_2 = 75$ %) as compared to the healthy controls ($sO_2 = 78$ %).

Discussion

We performed a straightforward quantification of sO_2 in the entire iBAT depots. The results support the MSOT measurements of metabolic activity [17], both in terms of the sO_2 trends and decrease of TBV in diabetic mice. Yet, the SVOT images enable better visualization of the depots and arguably more quantitative measurements due to the full 3D tomographic angular coverage and nearly isotropic resolution in all three dimensions [19]. Vascular structures can be clearly identified in the SVOT scans, which may facilitate the registration of images taken at different time points in longitudinal studies of the effects of diabetes on BAT.

The decrease in sO_2 of iBAT observed in diabetic mice is consistent with the expected decrease in metabolic activity in this tissue. The SVOT method is uniquely endowed with the capacity for longitudinal tracking of deep tissue oxygen metabolism without the need for extrinsic labeling. Its high sensitivity to hemoglobin allows for high-contrast visualization of the iBAT depots containing dense microvasculature networks. The measured reduced TBV values in the diabetic iBAT imply a decrease in the vasculature density with respect to the healthy tissue. Such deficiency is generally expected due to angiopathy-related vasculature deterioration. The sO_2 quantification can be significantly hampered if the iBAT cannot be clearly separated from the surrounding vessels, which was readily achieved here based on large differences in their underlying sO_2 levels.
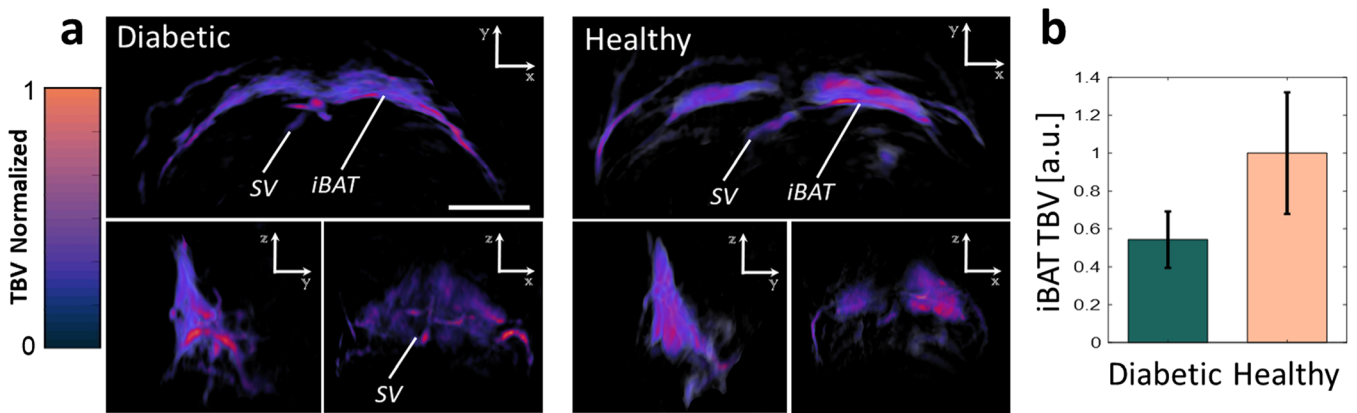
Fig. 2. **a** Three maximal intensity projections of the TBV distribution in the iBAT region of a diabetic mouse and a healthy mouse. The Sulzer vein (SV) position is also marked. **b** Comparison of TBV distribution in the diabetic and healthy iBAT ($p < 0.01$).

It has been previously shown that SVOT allows for visualizing biological processes at temporal scales ranging from a few milliseconds to several days [19]. Hence, apart from longitudinal studies on diabetes, it might further be possible to image dynamics in the iBAT depots, *e.g.*, associated with the induced activation of BAT [17]. The true volumetric nature of SVOT offers several advantages

with respect to other commonly employed cross-sectional optoacoustic imaging approaches [27, 28]. Indeed, the large solid angular coverage provided by the spherical array transducer enables accurate three-dimensional reconstructions not afflicted by the so-called limited-view effects [29]. This facilitates enhanced visibility of the three-dimensional tissue morphology and more quantitative readings of the

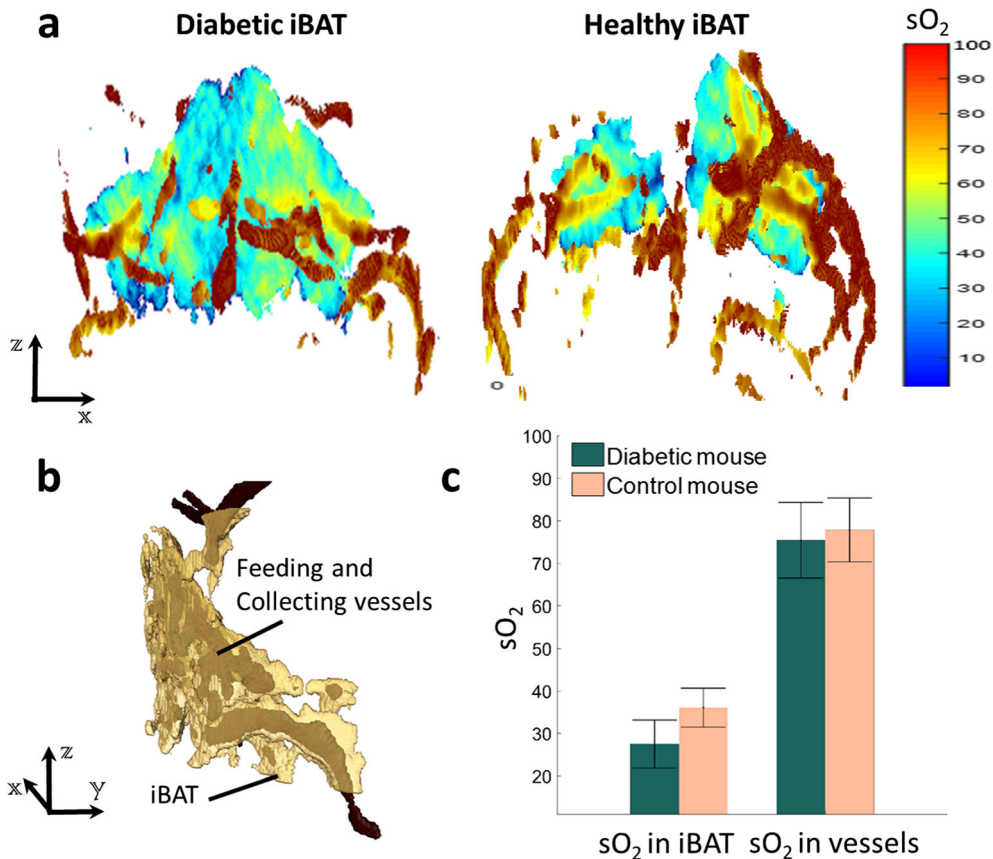**Fig. 3.** **a** Coronal projection of the sO_2 distribution map of the iBAT region of a diabetic mouse and a healthy mouse. **b** An illustration of the segmented iBAT in semi-transparent yellow, exposing feeding and collecting vessels in red, interwoven between and around the iBAT. **c** Comparison of sO_2 distribution between healthy and diabetic iBAT ($p < 0.01$) and between their major vessels.

tissue biochromes. Spatial resolution of the SVOT observations can also be enhanced by employing a spherical array with a larger detection bandwidth, as has recently been showcased with the optoacoustic microtomography (OMT) method [30]. At the near-infrared wavelengths, structures at a depth of at least 1 cm in living tissues can be imaged by SVOT, although this limitation is less significant in our measurements owing to the superficial location and high vascularization of the iBAT.

Conclusions

This work illustrates capabilities of the SVOT technique in diabetic research. Our results corroborate and complement recently reported measurements of metabolic activity where oxy and deoxy-hemoglobin gradients measured by a cross-sectional MSOT technique were used to differentiate between healthy and diabetic iBAT in mice [17]. Finally, the volumetric optoacoustic imaging probe used for the SVOT scans can be seamlessly operated in a handheld mode [31]. Since cervical BAT is located relatively superficially in humans, it is expected to be readily accessible with a handheld optoacoustic system based on a spherical matrix array. This may potentially serve as a viable clinical translation route for BAT-related studies with this 3D imaging technology. All in all, the volumetric and dynamic imaging capabilities of SVOT have the potential to reveal new insights into the BAT metabolism and improve its characterization in diabetes research.

Compliance with Ethical Standards

Ethics Approval and Consent to Participate

Not applicable.

Consent for Publication

Not applicable.

Conflict of Interest

The authors declare that they have no conflict of interest.

References

1. Owens B (2014) The changing colour of fat. Nature 508(7496):S52–S53
2. Nedergaard J, Bengtsson T, Cannon B (2007) Unexpected evidence for active brown adipose tissue in adult humans. Am J Physiol-Endoc Metab 293:E444–E452
3. Enerbäck S (2010) Human brown adipose tissue. Cell Metab 11:248–252
4. Orava J, Nuutila P, Lidell Martin E et al (2011) Different metabolic responses of human brown adipose tissue to activation by cold and insulin. Cell Metab 14:272–279
5. Xu L, Kanasaki K, Kitada M, Koya D (2012) Diabetic angiopathy and angiogenic defects. Fibrogen Tissue Rep 5: https://doi.org/10.1186/1755-1536-5-13
6. Cinti S (2012) The adipose organ at a glance. Dise Model Mech 5:588–594
7. Lenzen S (2008) The mechanisms of alloxan- and streptozotocin-induced diabetes. Diabetologia 51:216–226
8. Tekabe Y, Johnson LL, Rodriquez K, Li Q, Backer M, Backer JM (2018) Selective imaging of vascular endothelial growth factor receptor-1 and receptor-2 in atherosclerotic lesions in diabetic and non-diabetic apoe−/− mice. Mol Imaging Biol 20:85–93
9. Mirbolooki MR, Constantinescu CC, Pan M-L, Mukherjee J (2011) Quantitative assessment of brown adipose tissue metabolic activity and volume using ^{18}F-FDG PET/CT and β3-adrenergic receptor activation. EJNMMI Res 1:30. https://doi.org/10.1186/2191-219X-1-30
10. Lindholm H, Brolin F, Jonsson C, Jacobsson H (2014) Effects on the FDG distribution by a high uptake of brown adipose tissue at PET examination. EJNMMI Res 4:72. https://doi.org/10.1186/s13550-014-0072-0
11. de Boer SA, Spoor DS, Slart RHJA, et al. (2018) Performance evaluation of a semi-automated method for [^{18}F]FDG uptake in abdominal visceral adipose tissue. Mol Imaging Biol https://doi.org/10.1007/s11307-018-1211-1
12. Ran C, Albrecht DS, Bredella MA, et al. (2017) PET imaging of human brown adipose tissue with the TSPO tracer [^{11}C]PBR28. Mol Imaging Biol https://doi.org/10.1007/s11307-017-1129-z
13. Eriksson O, Mikkola K, Espes D, Tuominen L, Virtanen K, Forsback S, Haaparanta-Solin M, Hietala J, Solin O, Nuutila P (2015) The cannabinoid receptor-1 is an imaging biomarker of brown adipose tissue. J Nucl Med 56:1937–1941
14. Clerte M, Baron DM, Brouckaert P et al (2013) Brown adipose tissue blood flow and mass in obesity: a contrast ultrasound study in mice. J Am Soc Echocardiog 26:1465–1473
15. Nakayama A, Bianco AC, Zhang C-Y, et al. (2003) Quantitation of brown adipose tissue perfusion in transgenic mice using near-infrared fluorescence imaging. Mol imaging. 2: https://doi.org/10.1162/15353500200303103
16. Crane JD, Mottillo EP, Farncombe TH, Morrison KM, Steinberg GR (2014) A standardized infrared imaging technique that specifically detects ucp1-mediated thermogenesis in vivo. Mol Metab 3:490–494
17. Reber J, Willershäuser M, Karlas A, Paul-Yuan K, Diot G, Franz D, Fromme T, Ovsepian SV, Bézière N, Dubikovskaya E, Karampinos DC, Holzapfel C, Hauner H, Klingenspor M, Ntziachristos V (2018) Non-invasive measurement of brown fat metabolism based on optoacoustic imaging of hemoglobin gradients. Cell Metab 27:689–701
18. Chan XHD, Balasundaram G, Attia ABE, Goggi JL, Ramasamy B, Han W, Olivo M, Sugii S (2018) Multimodal imaging approach to monitor browning of adipose tissue in vivo. J Lipid Res 59:1071–1078
19. Deán-Ben XL, Fehm TF, Ford SJ, Gottschalk S, Razansky D (2017) Spiral volumetric optoacoustic tomography visualizes multi-scale dynamics in mice. Light: Sci App 6:e16247
20. Fehm TF, Deán-Ben XL, Ford SJ, Razansky D (2016) In vivo whole-body optoacoustic scanner with real-time volumetric imaging capacity. Optica 3:1153–1159
21. Xu M, Wang LV (2005) Universal back-projection algorithm for photoacoustic computed tomography. Phys Rev E 71:016706
22. Dean-Ben XL, Ozbek A, Razansky D (2013) Volumetric real-time tracking of peripheral human vasculature with GPU-accelerated three-dimensional optoacoustic tomography. IEEE Trans Med Imaging 32:2050–2055
23. Jacques SL (2013) Optical properties of biological tissues: a review. Phys Med Biol 58:R37–R61
24. Razansky D (2012) Multispectral optoacoustic tomography—volumetric color hearing in real time. IEEE J Sel Topics Quant 18:1234–1243
25. Nnodim JO, Lever JD (1988) Neural and vascular provisions of rat interscapular brown adipose tissue. Am J Anat 182:283–293

26. Otsu N (1979) A threshold selection method from gray-level histograms. IEEE Trans Syst Man Cyb 9:62–66
27. Deán-Ben XL, Razansky D (2013) Portable spherical array probe for volumetric real-time optoacoustic imaging at centimeter-scale depths. Opt Express 21:28062–28071
28. Deán-Ben XL, Razansky D (2014) Adding fifth dimension to optoacoustic imaging: volumetric time-resolved spectrally enriched tomography. Light Sci Appl 3:e137
29. Deán-Ben XL, Razansky D (2016) On the link between the speckle free nature of optoacoustics and visibility of structures in limited-view tomography. Photo-Dermatology 4:133–140
30. Deán-Ben XL, López-Schier H, Razansky D (2017) Optoacoustic micro-tomography at 100 volumes per second. Sci Rep 7:6850
31. Deán-Ben X, Fehm TF, Razansky D (2014) Universal hand-held three-dimensional optoacoustic imaging probe for deep tissue human angiography and functional preclinical studies in real time. J Vis Exper: JoVE 93:51864

7. Volumetric optoacoustic imaging unveils high-resolution patterns of acute and cyclic hypoxia in a murine model of breast cancer

7.1. Summary and Author Contribution

The motivation for this work was to demonstrate multiscale imaging at high-resolution. Resolution increase was achieved by employing a newly designed transducers array. The imaging scale was exchanged between large FOV – slow scan time, and small FOV at video rate. In both cases, multispectral imaging was employed to extract oxygenation maps. The aim of this work is to demonstrate the unique capabilities of this system by investigating tumor oxygenation. Firstly, to draw a large FOV oxygenation map of the tumor microenvironment in a true volumetric presentation, at spatial resolution which is unusual for scanning OAT systems. A few technical and methodological challenges had to be overcome, chiefly because the design of the high-resolution detector impedes the use of previous scanning geometries and physical tolerances. Also, from a biological point of view, the correct animal/tumor model had to be investigated such that it would provide a well-vascularized model which is subcutaneous and not too deep, such that the limited working distance of the detector would be sufficient. Subsequently, the detailed tumor reconstruction was chosen to appear on the cover of 'Cancer Research'. Secondly, observing temporal oxygen delivery phenomena, by covering a large volume of the tumor from a fixed detector's position while imaging at video rate. A major challenge here was to find a biological application that would benefit from this tool. I started by promoting existing research direction pertaining the measurement of tumor oxygen delivery using MRI methods of oxygen manipulations. Here, thanks to the superior sensitivity to hemoglobin contrast, higher resolution and volumetric quantification, I was able to demonstrate a new analysis method for tumor segmentation into functional regions. While analyzing this data, I accidently noticed a periodical phenomenon of hypoxic–reoxygenation periods, which appeared to be of key interest to the cancer research community (although with almost no existing imaging solutions, as I learned through an extensive literature review). By suggesting new approaches of

frequency and dynamic analyses in tumors, I was able to quantify and localize this phenomenon, and promote OAT as a promising modality for this application. This work was highlighted and received commentary in the same journal. It received the best poster award in EMIM conference 2019. The reviewers of this manuscript managed to identify the novelty of the periodical observations and pushed to extend and support the data by further experiments and analyses.

My contribution to the presented manuscript was the following:

Conception and design: I designed the experiment together with Dr. Dean-Ben (DB), Dr. Gottschalk and Dr. Razansky.

Development of methodology: I engineered the scanning system (installing new detectors, editing the scanning code, designing designated animal holders (together with Ms. Periyasamy), designed the laser operating scheme) together with DB.

Acquisition of data: I executed the animals imaging with the support of a lab technician Mr. Reiss.

Analysis and interpretation of data: I reconstructed the data. I designed and implemented new analysis algorithms. I designed and implemented new segmentation algorithm. I implemented the visualization tools. I implemented the statistical analysis (together with Ms. Silman).

Writing, review and revision of the manuscript: I drafted the manuscript and collaboratively revised it with all the participants. The same goes for the revisions.

Volumetric Optoacoustic Imaging Unveils High-Resolution Patterns of Acute and Cyclic Hypoxia in a Murine Model of Breast Cancer

Avihai Ron[1,2], Xosé Luís Deán-Ben[1,3,4], Sven Gottschalk[1], and Daniel Razansky[1,2,3,4]

Abstract

Mapping tumor heterogeneity and hypoxia within a living intact organism is essential for understanding the processes involved in cancer progression and assessing long-term responses to therapies. Efficient investigations into tumor hypoxia mechanisms have been hindered by the lack of intravital imaging tools capable of multiparametric probing of entire solid tumors with high spatial and temporal resolution. Here, we exploit volumetric multispectral optoacoustic tomography (vMSOT) for accurate, label-free delineation of tumor heterogeneity and dynamic oxygenation behavior. Mice bearing orthotopic MDA-MB-231 breast cancer xenografts were imaged noninvasively during rest and oxygen stress challenge, attaining time-lapse three-dimensional oxygenation maps across entire tumors with 100 μm spatial resolution. Volumetric quantification of the hypoxic fraction rendered values of

Volumetric multispectral optoacoustic tomography (vMSOT) enables label-free delineation of tumor heterogeneity and dynamic oxygenation behavior in mice bearing breast tumors.

3.9% to 21.2%, whereas the oxygen saturation (sO_2) rate declined at 1.7% to 2.3% per mm in all tumors when approaching their core. Three distinct functional areas (the rim, hypoxic, and normoxic cores) were clearly discernible based on spatial sO_2 profiles and responses to oxygen challenge. Notably, although sO_2 readings were responsive to the challenge, deoxyhemoglobin (HbR) trends exhibited little to no variations in all mice. Dynamic analysis further revealed the presence of cyclic hypoxia patterns with a 21% average discrepancy between cyclic fractions assessed via sO_2 (42.2% ± 17.3%) and HbR fluctuations (63% ± 14.1%) within the hypoxic core. These findings corroborate the strong potential of vMSOT for advancing preclinical imaging of cancer and informing clinical decisions on therapeutic interventions.
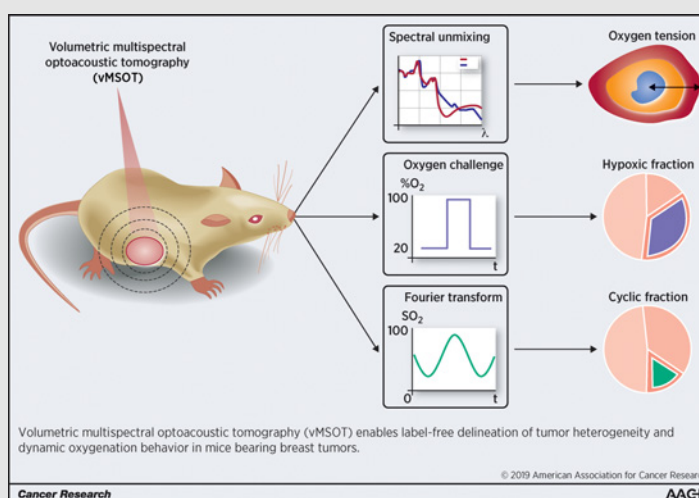
Significance: vMSOT provides quantitative measures of volumetric hypoxic fraction and cyclic hypoxia in a label-free and noninvasive manner, providing new readouts to aid tumor staging and treatment decision making.

Graphical Abstract: http://cancerres.aacrjournals.org/content/canres/79/18/4767/F1.large.jpg.

See related commentary by Klibanov and Hu, p. 4577

[1]Institute for Biological and Medical Imaging, Helmholtz Center Munich, Neuherberg, Germany. [2]Faculty of Medicine, Technical University of Munich, Munich, Germany. [3]Faculty of Medicine and Institute of Pharmacology and Toxicology, University of Zurich, Zurich, Switzerland. [4]Department of Information Technology and Electrical Engineering, Institute for Biomedical Engineering ETH Zurich, Zurich, Switzerland.

Note: Supplementary data for this article are available at Cancer Research Online (http://cancerres.aacrjournals.org/).

Corresponding Author: Daniel Razansky, Institute of Biomedical Engineering, University and ETH Zurich, Wolfgang-Pauli-Str. 27, 8093 Switzerland. Phone: 41-44-633-3429; E-mail: daniel.razansky@uzh.ch

Introduction

Mapping tumor heterogeneity is a key approach for assessing the long-term responses to therapy (1). The physiologic microenvironment of neoplastic lesions is dictated by abnormal metabolism and neovascularization, differing substantially from healthy tissues. A particularly important alteration is the presence of hypoxia, a condition of reduced level of oxygen partial pressure (pO_2) during which cells undertake key biological pathways associated to tumor growth. It appears that tumors exhibit highly heterogeneous and dynamic oxygenation patterns, ranging from normoxia to hypoxia. Disorders in oxygen distribution can further results in significant variations in perfusion to neighboring regions (2). This apparently chaotic behavior of cancerous tissues represents a major obstacle for understanding the disease (3).

Tumor hypoxia is also closely associated with resistance to chemotherapy and radiation therapy (4).

To this end, the spatial distribution of pO_2 within the tumor has been profiled via invasive methods, such as CT-guided pO_2 sensors. This enabled assessing the pO_2 drop between the viable rim and the core in just a few isolated locations (5). Imaging with ^{19}F-magnetic resonance oximetry (6) and ^{18}F-fluoromisonidazole PET (7) may provide higher spatial resolution but relies on exogenous oxygenation-sensitive agents. Furthermore, those methods mainly reveal static oxygenation profiles, only comprising a partial picture of the complex tumor microenvironment, while studying the transient spatiotemporal characteristics is essential for advancing the knowledge (8). For this, dynamic oxygen challenge has been suggested as a method for studying the oxygen stress response in tumors (9), aiming at characterizing the low perfusion efficiency of neovasculature by assessing responses to rapid respiratory challenges in different tumor subregions. Those were prominently studied with MRI (10) by exploiting the sensitivity of R_1-based sequences to changes of dissolved O_2 in blood (11). The approach was however limited by a relatively low spatiotemporal resolution further representing an indirect oxygen tension measure. It has been now widely recognized that, in addition to chronic hypoxia, reduced perfusion in some regions of the tumor may lead to appearance of hypoxic–reoxygenation periods. These fluctuations between hypoxic and nonhypoxic states are referred to as cyclic (dynamic) hypoxia (8), which is associated with increased tumor aggressiveness, resistance to treatments, and metastasis (12, 13). Hence, the ability to map and characterize the dynamics of cyclic heterogeneities may eventually contribute to improving treatment outcomes (14). Almost exclusively, MR methods have been used for this purpose. Although pO_2 and deoxyhemoglobin (HbR) variations were detected in tumor-bearing mice with electron paramagnetic (15) and with $T2^*$-weighted (16) and R_2^*-weighted (17) MRI, low spatiotemporal resolution remains the main limitation of MR-based methods preventing effective analysis of cyclic patterns in whole tumors. Moreover, conventional MRI instruments are restricted to HbR-correlated measurements lacking the clinical relevance of pO_2 (18). New methods to probe the tumor microenvironment over different time scales, from perfusion dynamics to neovasculature development, are then required for a better understanding of the processes involved in cancer progression.

Multispectral optoacoustic tomography (MSOT) is increasingly used in cancer research due to its unique capability for label-free noninvasive monitoring of hemodynamic parameters (19). A number of specific contrast agents have been further devised to sense key cancer biomarkers (20). MSOT was used to follow tumor growth and vascular development (21), to image tumor heterogeneity and perfusion (22–25), and to assess anticancer therapy efficacy (26). Previous works were yet limited to cross-sectional (2D) investigations unsuitable for an accurate characterization of differential real-time responses of neighboring subregions across entire solid tumors. Here we used instead a volumetric multispectral optoacoustic tomography system (vMSOT) approach based on simultaneous optoacoustic signal detection by a spherical array (27), with the aim to noninvasively characterize dynamic high-resolution patterns of acute and cyclic hypoxia in murine breast cancer models.

Materials and Methods

vMSOT

The vMSOT system is based on a previously described real-time volumetric tomography technique (28). Briefly, ultrasound (pressure) signals are induced by short (<10 ns duration) pulses of light from an optical parametric oscillator laser tunable in the near-infrared (NIR) spectral range (680–950 nm). The optoacoustically-generated signals are simultaneously detected by a 512-element spherical array transducer having 10 MHz detection bandwidth (Fig. 1A). During the experiments, the light fluence at the mouse skin surface was maintained below 20 mJ/cm^2 for all wavelengths. The system renders an effective field of view (FOV) of $6 \times 6 \times 6$ mm^3 with nearly isotropic three-dimensional (3D) spatial resolution in the 80 to 150 µm range. For imaging, both the transducer and the mouse were immersed in a water tank to facilitate propagation of the optoacoustically-generated pressure waves. Reconstruction of individual volumetric image frames for each illumination wavelength was performed with a graphics processing unit (GPU) implementation of a back-projection formula (29).

In vivo animal handling

The mouse *in vivo* experiments were approved by the government of Upper Bavaria. All experiments were performed in full compliance with the institutional guidelines of the Helmholtz Center Munich. Orthotopic tumors were induced in 6 weeks old female immunodeficient SHrN hairless NOD-SCID mice (Envigo) by subcutaneous injection of 3 million MDA-MB-231 cells in a total volume of 80 µL of PBS and Matrigel (1:1, v/v) into the inguinal gland of the mammary fat pad. *In vivo* imaging experiments were performed 30 days after cell inoculation, when the tumor reached an approximate size of 8 mm. The MDA-MB-231 cells were supplied by ATCC in May 2015, providing cell line authentication by STR analysis. The cell type was mycoplasma tested by a mycoplasma detection kit (Lonza) in March, 2019. Cells were used at four passages from thawing from frozen stocks. During acquisition, the mice were anesthetized with isoflurane [3% (v/v) for induction; 1.5%–2.0% (v/v) during imaging] in 100% O_2. A custom-made holder was used to maintain the mice in a stationary position with their fore and hind paws attached to the holder during the experiments. The mice were then immersed inside the water tank with the head kept outside water. The temperature of the water tank was maintained at 34°C with a feedback controlled heating stick. A breathing mask with a mouth clamp was used to fix the head in an upright position and to supply anesthesia and oxygen.

Whole tumor imaging and analysis

Although the effective FOV of the spherical array already covers a major portion of the tumor volume, high-resolution imaging of entire tumors and their surrounding areas was achieved by raster-scanning the array in the lateral (x–z) plane (Fig. 1A). Signal acquisition at multiple wavelengths (420, 730, 760, 800, and 850 nm) was performed to allow for a high-quality anatomical and functional tumor profiling. At each position of the array, 100 volumetric frames per wavelength were averaged after applying a motion rejection algorithm that eliminated frames affected by breathing-related motion (30). The reconstructed volumes were combined into a large-scale image of the entire region of interest (Fig. 1A). Images acquired at multiple

Figure 1.
A, Simplified schematic of the imaging set-up. The volumetric multispectral optoacoustic data were recorded with a spherical matrix array transducer probe that was also translated to acquire images from larger field of view. A typical 3D image of the thorax and abdominal region acquired at 800 nm from a tumor-bearing mouse is shown on the right. **B,** A zoomed-in depth encoded image of the tumor area showing vessel recruitment toward the core (white arrows). **C,** Photo of the tumor and a volumetric optoacoustic image (maximum intensity projection along y-axis) acquired at 420 nm. Three separate layers of dermis, rim, and core are visible. **D,** Spectrally unmixed sO_2 image of the same tumor showing the presence of hypoxic core and its highly oxygenated feeding vessels. Scale bar, 1 mm. a.u., arbitrary unit; FV, femoral vessels; IN, intestine; IV, ischiatic vessels; TFV, tumor feeding vessels; TV, thoratic vessels.
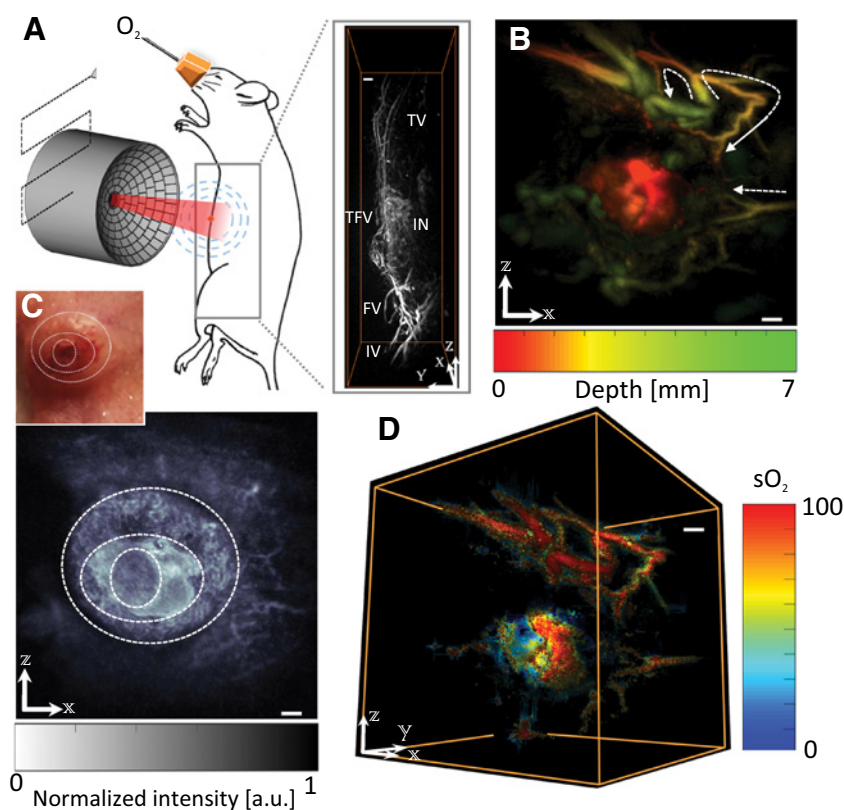
wavelengths were then processed with a standard linear unmixing method to estimate, on a voxel-per-voxel basis, the distribution of oxyhemoglobin (HbO), HbR, and total hemoglobin (THb) as well as the oxygen saturation (sO_2; ref. 31). 3D visualization of the optoacoustic images was done with Amira (Visual Sciences Group).

Segmentation into functional subregions

Tumors were segmented into 3 subregions, namely, the rim, normoxic, and hypoxic cores ($n = 6$ mice). The segmentation between the tumor rim and its core was done manually by estimating the boundary between the linear and parabolic-shape portions of the oxygen saturation profiles at 100% O_2 level, rendering boundary sO_2 values in the 50% to 62% range (Supplementary Fig. S1). The segmentation between the normoxic and hypoxic cores was based upon critical O_2 tension range of 10 to 20 mmHg pO_2 for which binding of hypoxia markers occurs (32). Note that the upper pO_2 threshold of 20 mmHg corresponds to a sO_2 value of 18% according to the Kelman and Severinghaus model (33) of the oxygen dissociation curve (where $pCO_2 = 40$ mmHg, pH 7, $T = 37°C$). Voxels with sO_2 values below 18% were thus regarded as hypoxic. The volumetric hypoxic fraction (vHF) measure was further calculated as the fraction of hypoxic voxels relative to the total voxel count in the tumor (voxels with insufficient signal-to-noise ratio were excluded).

Analysis of tumor dynamics

Dynamic tumor responses to breathing gas challenge were analyzed by recording time-lapse multispectral data with the spherical array remaining in a stationary position. The oxygen challenge experiments were performed by changing the percentage of oxygen in the breathing gas in the following order: 5 minutes of 20% O_2 (first baseline), 25 minutes of 100% O_2, and 15 minutes of 20% O_2 (second baseline). Prior to the challenge, the animals were given 15 minutes to stabilize at 20% O_2. To correct for respiratory motion artifacts, data were averaged over 2 seconds. Spatiotemporal volumetric sO_2 map was then calculated. Differential responses (ΔsO_2) to the oxygen stress were calculated on a per-voxel basis as signal difference between the averaged sO_2 during 100% O_2 breathing levels and the baselines, namely, each gas challenge yielded two differential responses for the first and second baselines. The ΔsO_2 voxels were grouped according to the 3 subregions, that is rim, normoxic core, and hypoxic core.

Cyclic hypoxia analysis

The second segment of the dynamic oxygen challenge corresponding to 25 minutes of 100% oxygen level was used for assessing cyclic hypoxia in the tumors of $n = 6$ mice. The analysis procedure is described elsewhere (34, 35). Briefly, the following processing steps were applied to the time profiles of each voxel: (i) linear detrending; (ii) calculation of the autocovariance; (iii) calculation of the power spectral density via fast Fourier transform (FFT); and (iv) thresholding according to a confidence interval, assuming that the signal is affected by Gaussian noise. Following these steps, the peak of the power spectrum for each voxel was identified. Voxels having a peak within frequency band of 0 to 0.005 Hz were regarded as cyclic voxels (3–18 cycles per hour is considered the relevant physiologic range; refs. 34, 36). The volumetric cyclic fraction (vCF) was calculated as the ratio

between the number of cyclic voxels and the total voxel count (excluding noisy voxels).

Statistical analysis

A total of $n = 6$ animals were evaluated contributing 12 independent ΔsO_2 measurements. For each subregion (rim, normoxic, or hypoxic core), approximately 100,000 voxels were evaluated. To represent the entire distribution for each subregion, pixels values were integrated using an average of all the pixels as well as the 25th percentile, median, and 75th percentile values. The differences in ΔsO_2 values across the subregions were compared using Friedman paired test followed by Dunn post hoc test. The differences between vCF values of the tumors ($n = 6$, calculated by either sO_2 or HbR analyses) were compared by an unpaired t test (*, $P < 0.05$; **, $P < 0.01$; ***, $P < 0.001$). Analyses were carried out using Matlab and SPSS 25.0 (SPSS Inc.).

Histologic validation

The mice were euthanized after being imaged with an overdose of ketamine (300 mg/kg) and directly stored at $-80°C$ until performing whole body cryo-slicing. For this, the frozen specimen were embedded in Tissue-Tek O.C.T. compound (Sakura Finetech Europe). Ten-μm thick sections covering the entire tumor volume were extracted. IHC was performed on the frozen sections using antibodies against CD31 (Dianova) or CAIX (Novus Biologicals). Antibody staining was visualized with Alexa Fluor 488 or Alexa Fluor 594 conjugated secondary antibodies (Life Technologies, Thermo Fisher Scientific). All slices were further costained with 4',6-diamidino-2-phenylindole (DAPI; Molecular Probes, Thermo Fisher Scientific) to visualize cell bodies. Fluorescence compound slice images were recorded using an Imager M2, microscope (Carl Zeiss AG). Image acquisition and analysis was done using the Zeiss Zen 2 microscope software.

Results

Multispectral 3D tumor imaging

Position of the tumor in the inguinal mammary gland is clearly visible in the compounded volume image of the entire region surrounding the tumor, which was acquired by a large area scan of the mouse abdomen at 800 nm (Fig. 1A). Because of the relatively low light attenuation at this wavelength, both tumor core and vast recruitment of neovascular networks from as deep as 7 mm are clearly visible (Fig. 1B). Note also the direction of arrows indicating some feeding vessels that branch from larger vessels and propagate toward the core. Image acquired at 420 nm reveals a different sort of anatomical information (Fig. 1C). For this wavelength, hemoglobin and melanin are highly absorbing, hence superior vascular contrast is achieved to the detriment of the maximal penetration depth of approximately 2 mm. Three distinct ring-type patterns can be observed across the tumor surface matching the photograph (Fig. 1C). An outer ring of epidermal and dermal layers is characterized by melanin absorption and fine vasculature patterns of the larger venules and arterioles (37). The middle ring with strong absorption signals is attributed to a highly oxygenated rim layer located close to the surface. Finally, the inner ring belongs to the tumor core that breaches the dermal layer and is characterized by reduced signal intensity. The sO_2 map retrieved from the multispectral data at

730, 760, 800, and 850 nm (Fig. 1D) suggests that the feeding vessels are well oxygenated whereas the core appears to be at an advanced hypoxic state with the highly perfused region at the edge, arguably belonging to the rim.

Analysis of the spatial sO_2 profiles

Spatial profiling of tumor oxygenation was performed by analyzing selected coronal slices at different depths (Fig. 2A). In this way, high-resolution sO_2 variations could be calculated as a function of distance from the center of the tumor (Fig. 2B). The corresponding sO_2 profiles (Fig. 2C; Supplementary Fig. S1) exhibit a substantial difference between the outer rim and the core with an average sO_2 drop of 1.7% to 2.3% per mm, as estimated by linear fitting. Segmentation of the rim and the core regions was based on thresholding the spatial sO_2 profiles, as shown for an exemplary slice in Fig. 2C. Comparison of the sO_2 map acquired at approximately 2 mm depth in vivo (Fig. 2D) with its corresponding ex vivo IHC showed that high sO_2-values colocalize with high expressions of CAIX (Fig. 2E) and CD31 (Fig. 2F), which may indicate that both proteins facilitate enhanced oxygen supply to the rim. Note, however, that both CAIX and CD31 can also be found in the tumor core, although with less confinement and lower density as compared with the rim.

Oxygen challenge responses

Owing to their disparate perfusion patterns, it is generally anticipated for the distinct tumor subregions to exhibit different responses to the dynamic oxygen challenge. As described in the previous section, the rim and core of each tumor were discerned by analyzing their corresponding spatial sO_2 profiles. Inside the core, a further segmentation into hypoxic and normoxic subregions was established via threshold-based approach by considering the critical O_2 tension for which binding of hypoxia markers occurs. Three distinct hypoxic foci are visible in a central sagittal slice showing the spatial architecture of neighboring hypoxic and normoxic subregions (Fig. 3A). A quantitative analysis of the relative volumes of the regions (Supplementary Table S1) allows for a more accurate assessment of hypoxia progression in the tumor. The relative volumetric fraction of the subregions was similar among all the imaged tumors, as well as the calculated vHFs (3.9–21.2%).

Additional insights on oxygen transport to the 3 subregions can be drawn by observing local sO_2 responses to the oxygen challenge (Fig. 3B; Supplementary Fig. S2) as well as the time-lapse video of the responses in single voxels (Supplementary Video S1). In all tumors, the rim and the normoxic core exhibit rapid response onset times of 1 to 2 minutes followed by a steady baseline. In contrast, hypoxic regions in the core exhibit moderate and unstable drops. These responses are not at all visible in the corresponding THb trends (Fig. 3C), which are characterized by a relative plateau in all tumors. The measured values of absolute sO_2 difference (ΔsO_2) between the baseline and 100% oxygen phase further show that each subregion presents a distinct response to the oxygen stress challenge (Fig. 3D; Supplementary Fig. S3), which held true for all the imaged tumors. Paired comparisons between the subregions of each tumor indicated that segregation between rim, normoxic core and hypoxic core is statistically significant across all the measurements ($P < 0.05$).
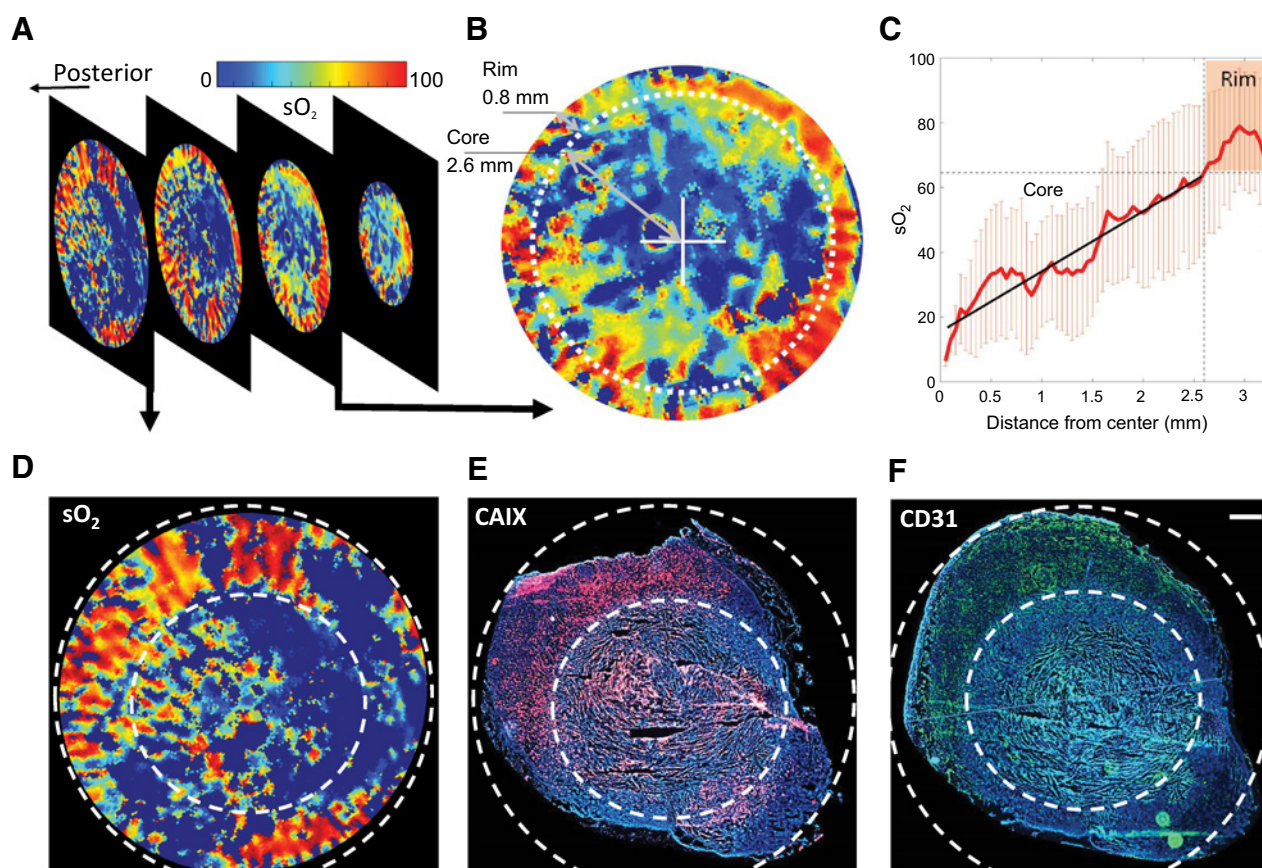
Figure 2.

A, A 3D stack of coronal slices extracted from the volumetric sO$_2$ map of the tumor. **B,** A representative slice showing the presence of two distinct tumor subregions. **C,** Radial sO$_2$ profile as a function of the distance from the tumor core ($R^2 = 0.78$). The calculated border between the rim and core is labeled by a dashed line. **D–F,** In vivo sO$_2$ map (**D**) of a different slice with its corresponding CAIX-DAPI histopathology (**E**) and CD31-DAPI staining (**F**) qualitatively matching the regions of enhanced oxygen supply and reduced oxygen supply. Scale bar, 1 mm.

Cyclic hypoxia

We subsequently exploited the unique rapid volumetric multispectral imaging capabilities of the vMSOT system in order to assess cyclic hypoxia patterns by comparing periodic variations of HbR and sO$_2$. HbR is of particular interest because it directly corresponds to the commonly measured BOLD MRI signals. The frequency spectrum of the HbR signal from a typical voxel in a central sagittal slice through a tumor exhibits a dominant frequency at 0.001 Hz (Fig. 4A). This value corresponds to 3 to 4 cycles per hour and was in fact predominantly manifested in majority of the tumor mass in all measurements, both in the unmixed HbR and sO$_2$ signal channels (Fig. 4A). The fluctuations of sO$_2$ and HbR have a characteristic amplitude variation of nearly 30% (Fig. 4B). We estimated the vCF values in all the imaged tumors to be in the 17% to 59% range (Supplementary Table S2), resembling the pO$_2$ ranges of 13% to 52% reported for ^{18}F-miso PET (38) and of 21 ± 6% to 41 ± 3% as measured by EPRI (15). An average discrepancy of 14% was observed between vCFs calculated from the HbR variations versus those based on the sO$_2$ (Fig. 4C). Notably, the hypoxic core subregion yielded the most significant difference ($P < 0.05$).

Discussion

Importance of mapping the spatial distribution of pO$_2$ in solid tumors has been acknowledged ever since hypoxia has been linked to treatment outcomes (1). Herein, we provided unique estimates of the 3D distribution of oxygenation patterns in murine breast cancer models with excellent spatial and temporal resolution owing to the new vMSOT approach. The imaging system provides sO$_2$ values by unmixing of multispectral data, from which the equivalent pO$_2$ can be calculated. We exploited the unique capabilities of vMSOT to gather otherwise unattainable information on the static, dynamic and cyclic sO$_2$ behavior in distinct tumor subregions. Experiments in mice implanted with MDA-MB-231 tumor cells indicated that sO$_2$ linearly increases by 1.7% to 2.3% sO$_2$ per mm when moving away from the center of the core. This constitutes a useful metric for accurate assessment of the tumor perfusion and matureness (23). Volumetric quantification of hypoxic fraction rendered a similar range of 12.2 ± 6.5% in all the studied tumors. This parameter was previously suggested for guiding clinical decisions pertaining optimization of tumor therapies (39). In this regard, the truly volumetric information provided by vMSOT is expected to

Ron et al.
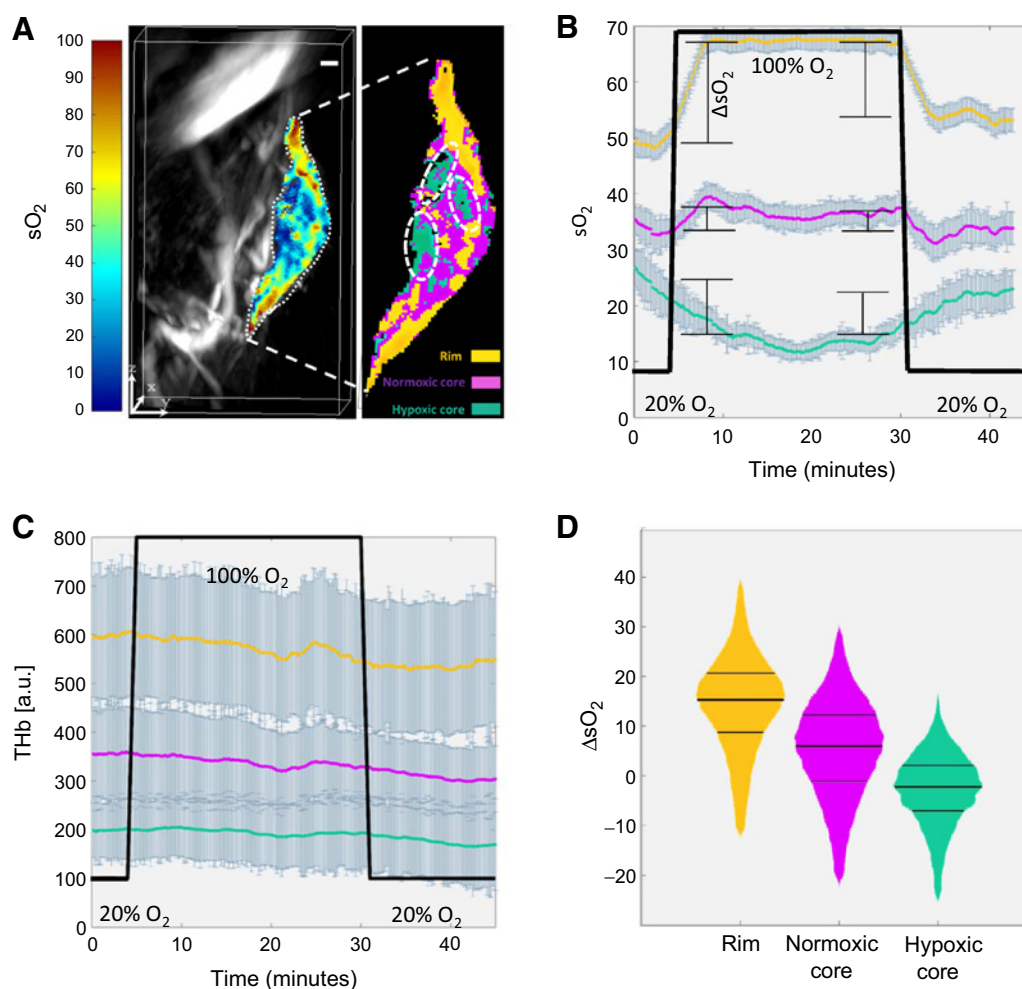
Figure 3.
A, sO_2 map of a sagittal slice of the tumor superimposed on an anatomical (single wavelength) optoacoustic image. Segmentation into three subregions (rim, normoxic core, and hypoxic core) is shown in the zoom-in. Scale bar, 1 mm. **B,** Average (with 1 SD) sO_2 response of each subregion to the dynamic oxygen challenge of a single animal (mouse #1). **C,** The corresponding THb signal exhibiting no significant variations in response to the oxygen challenge. **D,** The corresponding voxel distribution plot presenting the percentile differences between the oxygen saturation for 100% and 20% O_2 (center line represents the median, whereas the top and bottom thresholds represent the 25th and 75th quartiles). a.u., arbitrary unit.

significantly increase its accuracy with respect to 2D imaging approaches.

Here we were able to segment the tumor into 3 subregions, namely the rim, hypoxic, and normoxic cores. Although the rim area was subjectively differentiated by relying on its distinct features in the spatial sO_2 profiles, the core was segmented into hypoxic and normoxic subregions based on a theoretical threshold of critical pO_2 for which binding of hypoxia markers occurs. Note that translation between pO_2 and sO_2 according to the oxygen dissociation curves might be prone to errors due to variability in the temperature, pCO_2, or pH. The effectiveness of our segmentation methodology was further substantiated by demonstrating that oxygen saturation of the tumor subregions is significantly different. It is long known that chronic hypoxia in tumors is closely associated with limited perfusion (2). Thereby, we hypothesized that a dynamic oxygen challenge would corre-

spondingly reveal different local responses among the subregions. This was tested by exploiting the unique real-time 3D imaging capabilities of the vMSOT system. Notably, the ΔsO_2 analysis yields a good distinction ($P < 0.05$) between the subregions in all mice. It was shown that the rim and the normoxic subregions of the core exhibited significant variations in response to the oxygen stress, whereas the sO_2 in the hypoxic core decreased only mildly. Note that declining sO_2 trends during oxygen stress have been previously reported in prostate tumor cores (23). It is also worth mentioning that although sO_2 was responsive to the challenge, THb was barely altered in all mice. This indicates a clear advantage of the method with respect to alternative imaging modalities unable to differentiate between the oxygenated and deoxygenated states of hemoglobin. The dynamic ΔsO_2 analysis was thus exploited as a new robust method for direct segmentation of tumor subregions, which can be used to complement

Figure 4.
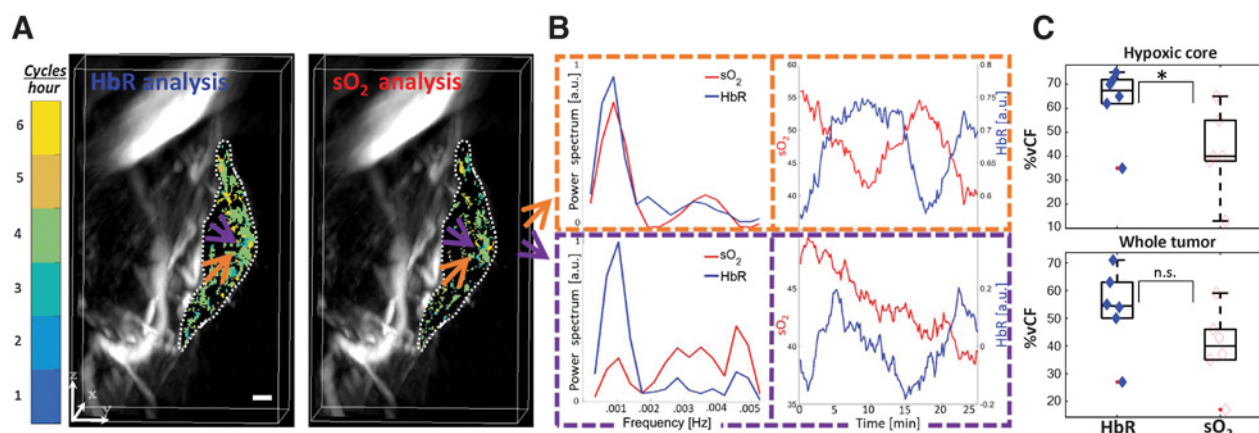**A,** Frequency map (single slice) of the hypoxic cycles in the tumor, as analyzed by HbR fluctuations and sO_2 fluctuations. The HbR-based maps exhibit higher density of cyclic voxels in comparison with the sO_2-based maps. Scale bar, 1 mm. **B,** Power spectrum and the corresponding amplitude fluctuations of two representative voxels. One voxel (orange arrow in **A**) exhibits cyclic behavior in both HbR and sO_2 channels, whereas the voxel labeled by a purple arrow only manifests cyclic behavior in the HbR channel. **C,** Distribution of vCF in all tumors reveals significant differences between the sO_2- and HbR-based analyses ($n = 6$). a.u., arbitrary unit; n.s., not significant. *, $P < 0.05$.

measurements done by other modalities that do not measure pO_2 or sO_2 directly but can only observe changes in trends (e.g., BOLD-MRI). Yet, it should be noted that the accuracy of sO_2 quantification by vMSOT might be affected by wavelength-dependent light attenuation in heterogeneous tissues (40, 41). For this reason, ΔsO_2 represents a more robust metric capable of eliminating common biases. The lack of variations in the THb profiles may be attributed to the limited vasoconstriction effects and the vascular tone within tumors (42, 43), which may further diminish due to the generally low levels of vessels functionality in MDA-MB-231 tumors (44).

Hemoglobin is an intrinsic contrast molecule for BOLD-MRI, which has been previously used for noninvasive characterization of cyclic hypoxia. The latter is known to have physiologic effects different from those of acute hypoxia (8). Our study is the first to detect the presence of cyclic hypoxia optoacoustically. We were able to analyze the cyclic oscillations of sO_2 and HbR simultaneously by solely relying on endogenous contrast. vMSOT provided a volumetric analysis of the entire tumor volume at high spatial and temporal resolution, which may contribute to an enhanced reliability of the cyclic fraction estimations. We observed discrepancy between the vCF values calculated via sO_2 versus HbR. On average, 14% of the tumor volume manifested cyclic hypoxia behavior in the HbR channel but not in the sO_2. Notably, the hypoxic core exhibited the highest vCF values. This is consistent with a previously reported observation that cyclic hypoxia is more likely to appear in tumor regions where oxygen saturation of the blood entering that region is relatively low (45). Moreover, the hypoxic core was also the region manifesting the most significant discrepancy of 21% between the sO_2 and HbR fluctuations. Because of the close relationship between sO_2 and pO_2, these results suggest an overestimation of cyclic fraction by the BOLD signal and other imaging methods solely using HbR-sensitive readouts for the cyclic analysis. Such a bias may have a clinical significance in treatment decisions that are based on the cyclic fraction values. MSOT has recently offered great prospects for

clinical translation in the field of metastatic lymph node detection (46) and breast cancer diagnostics (47–49). Therefore, preclinical studies with vMSOT may inform clinical decisions by, for example, providing error estimates of the vCF measurements for different tumor types. The new imaging capabilities demonstrated in this work further foster optoacoustic imaging as a valuable tool for the screening, diagnosis, treatment planning, and monitoring of cancer.

Disclosure of Potential Conflicts of Interest

Authors' Contributions

Conception and design: A. Ron, X.L. Deán-Ben, D. Razansky
Development of methodology: A. Ron, D. Razansky
Acquisition of data (provided animals, acquired and managed patients, provided facilities, etc.): A. Ron, X.L. Deán-Ben, S. Gottschalk, D. Razansky
Analysis and interpretation of data (e.g., statistical analysis, biostatistics, computational analysis): A. Ron, S. Gottschalk
Writing, review, and/or revision of the manuscript: A. Ron, X.L. Deán-Ben, S. Gottschalk, D. Razansky
Study supervision: D. Razansky

Acknowledgments

Ron et al.

References

1. Vaupel P, Mayer A. Hypoxia in cancer: significance and impact on clinical outcome. Cancer Metastasis Rev 2007;26:225–39.
2. Gillies RJ, Schomack PA, Secomb TW, Raghunand N. Causes and effects of heterogeneous perfusion in tumors. Neoplasia 1999;1:197–207.
3. Vaupel P, Schlenger K, Knoop C, Höckel M. Oxygenation of human tumors: evaluation of tissue oxygen distribution in breast cancers by computerized O2 tension measurements. Cancer Res 1991;51:3316–22.
4. Liu C, Lin Q, Yun Z. Cellular and molecular mechanisms underlying oxygen-dependent radiosensitivity. Radiat Res 2015;183:487–96.
5. Gatenby R, Coia L, Richter M, Katz H, Moldofsky P, Engstrom P, et al. Oxygen tension in human tumors: in vivo mapping using CT-guided probes. Radiology 1985;156:211–4.
6. Heerschap A, Simonetti AW, Rijken PF, Peters HP, Stüben G, van der Kogel AJ. Characterization and validation of noninvasive oxygen tension measurements in human glioma xenografts by 19F-MR relaxometry. Int J Radiat Oncol Biol Phys 1999;44:649–58.
7. O'Donoghue JA, Zanzonico P, Pugachev A, Wen B, Smith-Jones P, Cai S, et al. Assessment of regional tumor hypoxia using 18F-fluoromisonidazole and 64Cu (II)-diacetyl-bis (N4-methylthiosemicarbazone) positron emission tomography: comparative study featuring microPET imaging, Po2 probe measurement, autoradiography, and fluorescent microscopy in the R3327-AT and FaDu rat tumor models. Int J Radiat Oncol Biol Phys 2005; 61:1493–502.
8. Michiels C, Tellier C, Feron O. Cycling hypoxia: a key feature of the tumor microenvironment. Biochimica Biophys Acta 2016;1866:76–86.
9. Zhao D, Pacheco-Torres J, Hallac RR, White D, Peschke P, Cerdán S, et al. Dynamic oxygen challenge evaluated by NMR T1 and T2*–insights into tumor oxygenation. NMR Biomed 2015;28:937–47.
10. Zhao D, Constantinescu A, Hahn EW, Mason RP. Differential oxygen dynamics in two diverse Dunning prostate R3327 rat tumor sublines (MAT-Lu and HI) with respect to growth and respiratory challenge. Int J Radiat Oncol Biol Phys 2002;53:744–56.
11. O'Connor JP, Boult JK, Jamin Y, Babur M, Finegan KG, Williams KJ, et al. Oxygen enhanced MRI accurately identifies, quantifies, and maps hypoxia in preclinical cancer models. Cancer Res 2016;76:787–95.
12. Daneau G, Boidot R, Martinive P, Feron O. Identification of cyclooxygenase-2 as a major actor of the transcriptomic adaptation of endothelial and tumor cells to cyclic hypoxia: effect on angiogenesis and metastases. Clin Cancer Res 2010;16:410–9.
13. Moeller BJ, Cao Y, Li CY, Dewhirst MW. Radiation activates HIF-1 to regulate vascular radiosensitivity in tumors: role of reoxygenation, free radicals, and stress granules. Cancer Cell 2004;5:429–41.
14. Matsumoto S, Yasui H, Mitchell JB, Krishna MC. Imaging cycling tumor hypoxia. Cancer Res 2010;70:10019–23.
15. Yasui H, Matsumoto S, Devasahayam N, Munasinghe JP, Choudhuri R, Saito K, et al. Low-field magnetic resonance imaging to visualize chronic and cycling hypoxia in tumor-bearing mice. Cancer Res 2010;70: 6427–36.
16. Baudelet C, Cron GO, Ansiaux R, Crokart N, DeWever J, Feron O, et al. The role of vessel maturation and vessel functionality in spontaneous fluctuations of T2*-weighted GRE signal within tumors. NMR Biomed 2006;19:69–76.
17. Panek R, Welsh L, Baker LCJ, Schmidt MA, Wong KH, Riddell AM, et al. Noninvasive imaging of cycling hypoxia in head and neck cancer using intrinsic susceptibility MRI. Clin Cancer Res 2017;23:4233–41.
18. Baudelet C, Gallez B. How does blood oxygen leveldependent (BOLD) contrast correlate with oxygen partial pressure (pO2) inside tumors? Magn Reson Med 2002;48:980–6.
19. Deán-Ben X, Gottschalk S, Mc Larney B, Shoham S, Razansky D. Advanced optoacoustic methods for multiscale imaging of in vivo dynamics. Chem Soc Rev 2017;46:2158–98.
20. Levi J, Kothapalli SR, Bohndiek S, Yoon JK, Dragulescu-Andrasi A, Nielsen C, et al. Molecular photoacoustic imaging of follicular thyroid carcinoma. Clin Cancer Res 2013;19:1494–502.
21. Laufer JG, Zhang EZ, Treeby BE, Cox BT, Beard PC, Johnson P, et al. In vivo preclinical photoacoustic imaging of tumor vasculature development and therapy. J Biomed Opt 2012;17:056016.
22. Tomaszewski MR, Gehrung M, Joseph J, Quiros-Gonzalez I, Disselhorst JA, Bohndiek SE. Oxygen-enhanced and dynamic contrast-

23. enhanced optoacoustic tomography provide surrogate biomarkers of tumor vascular function, hypoxia, and necrosis. Cancer Res 2018;78: 5980–91.
23. Tomaszewski MR, Gonzalez IQ, O'Connor JP, Abeyakoon O, Parker GJ, Williams KJ, et al. Oxygen enhanced optoacoustic tomography (OE-OT) reveals vascular dynamics in murine models of prostate cancer. Theranostics 2017;7:2900.
24. Herzog E, Taruttis A, Beziere N, Lutich AA, Razansky D, Ntziachristos V. Optical imaging of cancer heterogeneity with multispectral optoacoustic tomography. Radiology 2012;263:461–8.
25. Ermolayev V, Dean-Ben XL, Mandal S, Ntziachristos V, Razansky D. Simultaneous visualization of tumour oxygenation, neovascularization and contrast agent perfusion by real-time three-dimensional optoacoustic tomography. Eur Radiol 2016;26:1843–51.
26. Xie B, Tomaszewski MR, Neves A, Ros S, Hu DE, McGuire S, et al. Optoacoustic detection of early therapy-induced tumor cell death using a targeted imaging agent. Clin Cancer Res 2017;23:6893–903.
27. Deán-Ben XL, Fehm TF, Ford SJ, Gottschalk S, Razansky D. Spiral volumetric optoacoustic tomography visualizes multi-scale dynamics in mice. Light Sci Appl 2017;6:e16247.
28. Deán-Ben XL, Sela G, Lauri A, Kneipp M, Ntziachristos V, Westmeyer GG, et al. Functional optoacoustic neuro-tomography for scalable whole-brain monitoring of calcium indicators. Light Sci Appl 2016;5:e16201.
29. Rosenthal A, Ntziachristos V, Razansky D. Acoustic inversion in optoacoustic tomography: a review. Curr Med Imaging Rev 2013;9:318–36.
30. Fehm TF, Deán-Ben XL, Ford SJ, Razansky D. In vivo whole-body optoacoustic scanner with real-time volumetric imaging capacity. Optica 2016;3: 1153–9.
31. Razansky D, Buehler A, Ntziachristos V. Volumetric real-time multispectral optoacoustic tomography of biomarkers. Nat Protoc 2011;6:1121.
32. Hockel M, Vaupel P. Tumor hypoxia: definitions and current clinical, biologic, and molecular aspects. J Natl Cancer Inst 2001;93:266–76.
33. Severinghaus JW. Simple, accurate equations for human blood O2 dissociation computations. J Appl Physiol 1979;46:599–602.
34. Baudelet C, Ansiaux R, Jordan BF, Havaux X, Macq B, Gallez B. Physiological noise in murine solid tumours using T2*-weighted gradient-echo imaging: a marker of tumour acute hypoxia? Phys Med Biol 2004;49:3389.
35. Baudelet C, Gallez B. Cluster analysis of BOLD fMRI time series in tumors to study the heterogeneity of hemodynamic response to treatment. Magn Reson Med 2003;49:985–90.
36. Gonçalves MR, Johnson SP, Ramasawmy R, Pedley RB, Lythgoe MF, Walker-Samuel S. Decomposition of spontaneous fluctuations in tumour oxygenation using BOLD MRI and independent component analysis. Br J Cancer 2015;113:1168.
37. Braverman IM. The cutaneous microcirculation: ultrastructure and micro-anatomical organization. Microcirculation 1997;4:329–40.
38. Wang K, Yorke E, Nehmeh SA, Humm JL, Ling CC. Modeling acute and chronic hypoxia using serial images of PET. Med Phys 2009;36:4400–8.
39. Wilson WR, Hay MP. Targeting hypoxia in cancer therapy. Nat Rev Cancer 2011;11:393.
40. Olefir I, Tzoumas S, Yang H, Ntziachristos V. A Bayesian approach to eigenspectra optoacoustic tomography. IEEE Trans Med Imaging 2018;37: 2070–9.
41. Tzoumas S, Nunes A, Olefir I, Stangl S, Symvoulidis P, Glasl S, et al. Eigenspectra optoacoustic tomography achieves quantitative blood oxygenation imaging deep in tissues. Nat Commun 2016;7:2121.
42. Carpenter CM, Rakow-Penner R, Jiang S, Daniel BL, Pogue BW, Glover GH, et al. Inspired gas-induced vascular change in tumors with magnetic-resonance-guided near-infrared imaging: human breast pilot study. J Biomed Opt 2010;15:036026.
43. West JB. Respiratory physiology: the essentials. Baltimore, MD: Lippincott Williams & Wilkins; 2012.
44. Quiros-Gonzalez I, Tomaszewski MR, Aitken SJ, Ansel-Bollepalli L, McDuffus L-A, Gill M, et al. Optoacoustics delineates murine breast cancer models displaying angiogenesis and vascular mimicry. Br J Cancer 2018;118:1098.
45. Dewhirst MW. Relationships between cycling hypoxia, HIF-1, angiogenesis and oxidative stress. Radiat Res 2009;172:653–65.
46. Stoffels I, Morscher S, Helfrich I, Hillen U, Leyh J, Burton NC, et al. Metastatic status of sentinel lymph nodes in melanoma determined

noninvasively with multispectral optoacoustic imaging. Sci Transl Med 2015;7:317ra199.

47. Lin L, Hu P, Shi J, Appleton CM, Maslov K, Li L, et al. Single-breath-hold photoacoustic computed tomography of the breast. Nat Commun 2018;9: 2352.

48. Abeyakoon O, Morscher S, Dalhaus N, Ford SJ, Mendichovszky IA, Manavaki R, et al. Optoacoustic imaging detects hormone-related physiological changes of breast parenchyma. Ultraschall Med 2018 Jun 7 [Epub ahead of print].

49. Heijblom M, Piras D, van den Engh FM, van der Schaaf M, Klaase JM, Steenbergen W, et al. The state of the art in breast imaging using the Twente Photoacoustic Mammoscope: results from 31 measurements on malignancies. Eur Radiol 2016;26: 3874–87.

Volumetric Optoacoustic Imaging Unveils High-Resolution Patterns of Acute and Cyclic Hypoxia in a Murine Model of Breast Cancer

Avihai Ron, Xosé Luís Deán-Ben, Sven Gottschalk, et al.

Updated version	Access the most recent version of this article at: doi:10.1158/0008-5472.CAN-18-3769
Supplementary Material	Access the most recent supplemental material at: http://cancerres.aacrjournals.org/content/suppl/2019/05/16/0008-5472.CAN-18-3769.DC1

Visual Overview	**A diagrammatic summary of the major findings and biological implications:** http://cancerres.aacrjournals.org/content/79/18/4767/F1.large.jpg

Cited articles	This article cites 44 articles, 9 of which you can access for free at: http://cancerres.aacrjournals.org/content/79/18/4767.full#ref-list-1

E-mail alerts	Sign up to receive free email-alerts related to this article or journal.
Reprints and Subscriptions	To order reprints of this article or to subscribe to the journal, contact the AACR Publications Department at pubs@aacr.org.
Permissions	To request permission to re-use all or part of this article, use this link http://cancerres.aacrjournals.org/content/79/18/4767. Click on "Request Permissions" which will take you to the Copyright Clearance Center's (CCC) Rightslink site.

8. Conclusion and outlook

This work advances OAT one step further towards a complete and mature small-animal research technology. The new FlashOT system grants volumetric functional and molecular imaging at organ or whole-body scales, at exceptionally short scanning times. Such characteristics are unique not only to OAT (where the output is normally restricted to cross-sectional images), but also in comparison to established technologies such as micro-PET and micro-CT. In fact, the FlashOT system opens a window for "PET-like" molecular imaging, combining spatiotemporal qualities that are approaching CT merits. Yet, although OAT offers key technological advantages over PET (e.g. sensitivity to endogenous chromophores, non-ionizing radiation, anatomical context, higher resolution, scanning time), OAT's applicability, standardization and successful market penetration, are held back by the limited number of practical molecular agents in the NIR regime for quantitative metabolic analyses (e.g. tumor uptake) and for drugs labeling in pharmacokinetics.

From a functional imaging point of view, the volumetric quantification over hemodynamics parameters that I demonstrate in tumors, specifically concerning the mapping of cyclic hypoxia for treatment monitoring, may be directly translated into in-human applications. This may be realized by hand-held transducers (also based on spherical transducer array) that could be readily employed to inspect accessible tumors (e.g. skin or breast, with the limitation of depth of penetration) and serve as a promising alternative to the cumbersome and expensive fMRI exams.

Further technical work on the FlashOT system concerns the matter of reduced in-plane image quality, in comparison for instance, to "ring array" systems. This could result from light fluence heterogeneity for different scanner positions, which may promote inaccuracies in the process of reconstruction. It could be improved by modeling and correcting the light fluence distribution for this specific system. From a commercialization point of view, a major challenge would be to design the scanner such that it eliminates the need of a massive tank where the animal and the transducer are fully immersed in water (this would also ease the process of degassing a high volume of deionized water, which is essential for eliminating microbubbles and reducing corresponding image artifacts). From a usability perspective, the current design of the animal holder possesses difficult mounting of the animal. Also, the positioning of the animal in a vertical orientation may seem unconventional and have physiological implications.

The respiratory motion correction algorithm that I designed is designated for "stop and go" scanning schemes and cannot be implemented during continuous scanning. Hence, a different solution for motion correction should be adapted for FlashOT. This could be readily solved by standard gating methods (which would require additional sensors for reading physiological signals) or more advanced prospective methods.

References

1   Dima, A., Burton, N. C. & Ntziachristos, V. Multispectral optoacoustic tomography at 64, 128, and 256 channels. *Journal of biomedical optics* **19**, 036021 (2014).

2   Li, L. *et al.* Single-impulse panoramic photoacoustic computed tomography of small-animal whole-body dynamics at high spatiotemporal resolution. *Nature biomedical engineering* **1**, 1-11 (2017).

3   Merčep, E., Herraiz, J. L., Deán-Ben, X. L. & Razansky, D. Transmission–reflection optoacoustic ultrasound (TROPUS) computed tomography of small animals. *Light: Science & Applications* **8**, 1-12 (2019).

4   Davoudi, N., Deán-Ben, X. L. & Razansky, D. Deep learning optoacoustic tomography with sparse data. *Nature Machine Intelligence* **1**, 453-460 (2019).

5   Basak, K., Deán-Ben, X. L., Gottschalk, S., Reiss, M. & Razansky, D. Non-invasive determination of murine placental and foetal functional parameters with multispectral optoacoustic tomography. *Light: Science & Applications* **8**, 1-10 (2019).

6   Manohar, S. & Dantuma, M. Current and future trends in photoacoustic breast imaging. *Photoacoustics* (2019).

7   Brecht, H.-P. F. *et al.* Whole-body three-dimensional optoacoustic tomography system for small animals. *Journal of biomedical optics* **14**, 064007 (2009).

8   Xia, J., Chen, W., Maslov, K. I., Anastasio, M. A. & Wang, L. V. Retrospective respiration-gated whole-body photoacoustic computed tomography of mice. *Journal of biomedical optics* **19**, 016003 (2014).

9   Zaitsev, M., Maclaren, J. & Herbst, M. Motion artifacts in MRI: A complex problem with many partial solutions. *Journal of Magnetic Resonance Imaging* **42**, 887-901 (2015).

10   Maclaren, J., Herbst, M., Speck, O. & Zaitsev, M. Prospective motion correction in brain imaging: a review. *Magnetic resonance in medicine* **69**, 621-636 (2013).

11   Foster, D. O. & Frydman, M. L. Tissue distribution of cold-induced thermogenesis in conscious warm-or cold-acclimated rats reevaluated from changes in tissue blood flow: the dominant role of brown adipose tissue in the replacement of shivering by nonshivering thermogenesis. *Canadian journal of physiology and pharmacology* **57**, 257-270 (1979).

12   Gottschalk, S., Felix Fehm, T., Luís Deán-Ben, X. & Razansky, D. Noninvasive real-time visualization of multiple cerebral hemodynamic parameters in whole mouse brains using five-dimensional optoacoustic tomography. *Journal of Cerebral Blood Flow & Metabolism* **35**, 531-535 (2015).

13   Ntziachristos, V., Pleitez, M. A., Aime, S. & Brindle, K. M. Emerging technologies to image tissue metabolism. *Cell metabolism* **29**, 518-538 (2019).

14   Diot, G., Dima, A. & Ntziachristos, V. Multispectral opto-acoustic tomography of exercised muscle oxygenation. *Optics letters* **40**, 1496-1499 (2015).

15   Regensburger, A. P. *et al.* Detection of collagens by multispectral optoacoustic tomography as an imaging biomarker for Duchenne muscular dystrophy. *Nature Medicine* **25**, 1905-1915 (2019).

16   Aguirre, J. *et al.* Precision assessment of label-free psoriasis biomarkers with ultra-broadband optoacoustic mesoscopy. *Nature Biomedical Engineering* **1**, 0068 (2017).

17   Schwarz, M., Buehler, A., Aguirre, J. & Ntziachristos, V. Three-dimensional multispectral optoacoustic mesoscopy reveals melanin and blood oxygenation in human skin in vivo. *Journal of biophotonics* **9**, 55-60 (2016).

18   Pleitez, M. A. *et al.* Label-free metabolic imaging by mid-infrared optoacoustic microscopy in living cells. *Nature Biotechnology*, 1-4 (2019).

19   Cinti, S. The adipose organ at a glance. *Disease Models & Mechanisms* **5**, 588-594, doi:10.1242/dmm.009662 (2012).

20   Owens, B. The changing colour of fat. *Nature* **508**, S52 (2014).

21   Enerbäck, S. Human Brown Adipose Tissue. *Cell Metabolism* **11**, 248-252, doi:https://doi.org/10.1016/j.cmet.2010.03.008 (2010).

22   Lundbaek, K. *et al.* Diabetes, diabetic angiopathy, and growth hormone. *The Lancet* **296**, 131-133 (1970).

23   Reber, J. *et al.* Non-invasive Measurement of Brown Fat Metabolism Based on Optoacoustic Imaging of Hemoglobin Gradients. *Cell metabolism* **27**, 689-701. e684 (2018).

24   Cannon, B. & Nedergaard, J. Nonshivering thermogenesis and its adequate measurement in metabolic studies. *Journal of Experimental Biology* **214**, 242-253 (2011).

25   Cherry, S. R. *et al.* MicroPET: a high resolution PET scanner for imaging small animals. *Ieee transactions on nuclear science* **44**, 1161-1166 (1997).

26   Del Guerra, A. & Belcari, N. State-of-the-art of PET, SPECT and CT for small animal imaging. *Nuclear Instruments and Methods in Physics Research Section A: Accelerators, Spectrometers, Detectors and Associated Equipment* **583**, 119-124 (2007).

27   Lee, M. S., Kim, K. Y., Ko, G. B. & Lee, J. S. Prototype pre-clinical PET scanner with depth-of-interaction measurements using single-layer crystal array and single-ended readout. *Physics in Medicine & Biology* **62**, 3983 (2017).

28   Cherry, S. R. in *Seminars in nuclear medicine.* 348-353 (Elsevier).

29   Deroose, C. M. *et al.* Multimodality imaging of tumor xenografts and metastases in mice with combined small-animal PET, small-animal CT, and bioluminescence imaging. *Journal of Nuclear Medicine* **48**, 295-303 (2007).

30   Kurz, C. *et al.* Investigating the limits of PET/CT imaging at very low true count rates and high random fractions in ion-beam therapy monitoring. *Medical physics* **42**, 3979-3991 (2015).

31   Molinos, C. *et al.* Low-dose imaging in a new preclinical total-body PET/CT scanner. *Frontiers in medicine* **6** (2019).

32   Baker, M. Whole-animal imaging: The whole picture. *Nature* **463**, 977 (2010).

33   Nedergaard, J., Bengtsson, T. & Cannon, B. Unexpected evidence for active brown adipose tissue in adult humans. *American Journal of Physiology-Endocrinology and Metabolism* **293**, E444-E452 (2007).

34   Karlas, A., Reber, J., Liapis, E., Paul-Yuan, K. & Ntziachristos, V. in *Brown Adipose Tissue* 325-336 (Springer, 2018).

35   Willmann, J. K., Van Bruggen, N., Dinkelborg, L. M. & Gambhir, S. S. Molecular imaging in drug development. *Nature reviews Drug discovery* **7**, 591 (2008).

36   Hensley, C. T. *et al.* Metabolic heterogeneity in human lung tumors. *Cell* **164**, 681-694 (2016).

37   Eo, J. S. & Jeong, J. M. in *Seminars in nuclear medicine.* 419-427 (Elsevier).

38   Gerstner, E. R. *et al.* ACRIN 6684: assessment of tumor hypoxia in newly diagnosed glioblastoma using 18F-FMISO PET and MRI. *Clinical Cancer Research* **22**, 5079-5086 (2016).

39   Laufer, J. G. *et al.* In vivo preclinical photoacoustic imaging of tumor vasculature development and therapy. *Journal of biomedical optics* **17**, 056016 (2012).

40   Lao, Y., Xing, D., Yang, S. & Xiang, L. Noninvasive photoacoustic imaging of the developing vasculature during early tumor growth. *Physics in Medicine & Biology* **53**, 4203 (2008).

41   Siphanto, R. *et al.* Serial noninvasive photoacoustic imaging of neovascularization in tumor angiogenesis. *Optics express* **13**, 89-95 (2005).

42   Tomaszewski, M. R. *et al.* Oxygen-Enhanced and Dynamic Contrast-Enhanced Optoacoustic Tomography Provide Surrogate Biomarkers of Tumor Vascular Function, Hypoxia, and Necrosis. *Cancer research* **78**, 5980-5991 (2018).

43   Tomaszewski, M. R. *et al.* Oxygen enhanced optoacoustic tomography (OE-OT) reveals vascular dynamics in murine models of prostate cancer. *Theranostics* **7**, 2900 (2017).

44   Herzog, E. *et al.* Optical imaging of cancer heterogeneity with multispectral optoacoustic tomography. *Radiology* **263**, 461-468 (2012).

45   Ermolayev, V., Dean-Ben, X. L., Mandal, S., Ntziachristos, V. & Razansky, D. Simultaneous visualization of tumour oxygenation, neovascularization and contrast agent perfusion by real-time three-dimensional optoacoustic tomography. *European radiology* **26**, 1843-1851 (2016).

46   Kelman, G. R. Digital computer subroutine for the conversion of oxygen tension into saturation. *Journal of applied physiology* **21**, 1375-1376 (1966).

47   Levi, J. *et al.* Molecular photoacoustic imaging of follicular thyroid carcinoma. *Clinical Cancer Research* **19**, 1494-1502 (2013).

48   Wilson, K. E., Wang, T. Y. & Willmann, J. K. Acoustic and photoacoustic molecular imaging of cancer. *Journal of Nuclear Medicine* **54**, 1851-1854 (2013).

49   Weber, J., Beard, P. C. & Bohndiek, S. E. Contrast agents for molecular photoacoustic imaging. *Nature methods* **13**, 639 (2016).

50   Barth, M. & Moser, E. Proton NMR relaxation times of human blood samples at 1.5 T and implications for functional MRI. *Cellular and molecular biology* **43**, 783-791 (1997).

51   Wagenseil, J. E., Johansson, L. O. & Lorenz, C. H. Characterization of T1 relaxation and blood-myocardial contrast enhancement of NC100150 injection in cardiac MRI. *Journal of Magnetic Resonance Imaging: An Official Journal of the International Society for Magnetic Resonance in Medicine* **10**, 784-789 (1999).

52   Prasad, P. V., Edelman, R. R. & Epstein, F. H. Noninvasive evaluation of intrarenal oxygenation with BOLD MRI. *Circulation* **94**, 3271-3275 (1996).

53   Taylor, N. J. *et al.* BOLD MRI of human tumor oxygenation during carbogen breathing. *Journal of Magnetic Resonance Imaging: An Official Journal of the International Society for Magnetic Resonance in Medicine* **14**, 156-163 (2001).

54   Liao, L.-D. *et al.* Transcranial imaging of functional cerebral hemodynamic changes in single blood vessels using in vivo photoacoustic microscopy. *Journal of Cerebral Blood Flow & Metabolism* **32**, 938-951 (2012).

55   O'Connor, J. P. *et al.* Oxygen-enhanced MRI accurately identifies, quantifies, and maps tumor hypoxia in preclinical cancer models. *Cancer research* **76**, 787-795 (2016).

56   Monahan, K. *et al.* Pulmonary transit time from contrast echocardiography and cardiac magnetic resonance imaging: Comparison between modalities and the impact of region of interest characteristics. *Echocardiography* **36**, 119-124 (2019).

57   Breen, E. C., Scadeng, M., Lai, N. C., Murray, F. & Bigby, T. D. Functional magnetic resonance imaging for in vivo quantification of pulmonary hypertension in the Sugen 5416/hypoxia mouse. *Experimental physiology* **102**, 347-353 (2017).

58   Lin, H.-C. A. *et al.* Characterization of cardiac dynamics in an acute myocardial infarction model by four-dimensional optoacoustic and magnetic resonance imaging. *Theranostics* **7**, 4470 (2017).

59   Ivankovic, I. *et al.* Volumetric optoacoustic tomography enables non-invasive in vivo characterization of impaired heart function in hypoxic conditions. *Scientific reports* **9**, 8369 (2019).

60   Beard, P. Biomedical photoacoustic imaging. *Interface focus* **1**, 602-631 (2011).

61   Wang, L. V. Tutorial on photoacoustic microscopy and computed tomography. *IEEE Journal of Selected Topics in Quantum Electronics* **14**, 171-179 (2008).

62   Smith, A. M., Mancini, M. C. & Nie, S. Bioimaging: second window for in vivo imaging. *Nature nanotechnology* **4**, 710 (2009).

63   Dreaden, E. C., Alkilany, A. M., Huang, X., Murphy, C. J. & El-Sayed, M. A. The golden age: gold nanoparticles for biomedicine. *Chemical Society Reviews* **41**, 2740-2779 (2012).

64   Chen, Y.-S. *et al.* Silica-coated gold nanorods as photoacoustic signal nanoamplifiers. *Nano letters* **11**, 348-354 (2011).

65   Chen, Y.-S., Zhao, Y., Yoon, S. J., Gambhir, S. S. & Emelianov, S. Miniature gold nanorods for photoacoustic molecular imaging in the second near-infrared optical window. *Nature nanotechnology* **14**, 465 (2019).

66   Homan, K. *et al.* Prospects of molecular photoacoustic imaging at 1064 nm wavelength. *Optics letters* **35**, 2663-2665 (2010).

67   Ding, L. *et al.* Constrained Inversion and Spectral Unmixing in Multispectral Optoacoustic Tomography. *IEEE transactions on medical imaging* **36**, 1676-1685 (2017).

68   Knauer, N., Deán-Ben, X. L. & Razansky, D. Spatial Compounding of Volumetric Data Enables Freehand Optoacoustic Angiography of Large-Scale Vascular Networks. *IEEE Transactions on Medical Imaging* (2019).

69   Nitkunanantharajah, S., Hennersperger, C., Dean-Ben, X. L., Razansky, D. & Navab, N. Trackerless panoramic optoacoustic imaging: a first feasibility evaluation. *International journal of computer assisted radiology and surgery* **13**, 703-711 (2018).

70   Deán-Ben, X. L. & Razansky, D. Functional optoacoustic human angiography with handheld video rate three dimensional scanner. *Photoacoustics* **1**, 68-73 (2013).

71   Deán-Ben, X. L., Fehm, T. F., Gostic, M. & Razansky, D. Volumetric hand-held optoacoustic angiography as a tool for real-time screening of dense breast. *Journal of biophotonics* **9**, 253-259 (2016).

72   Deán-Ben, X. L., Ozbek, A. & Razansky, D. Volumetric real-time tracking of peripheral human vasculature with GPU-accelerated three-dimensional optoacoustic tomography. *IEEE transactions on medical imaging* **32**, 2050-2055 (2013).

73   Kotsianos, D. *et al.* 3D imaging with an isocentric mobile C-arm. *European radiology* **14**, 1590-1595 (2004).

74   Heiland, M., Schulze, D., Blake, F. & Schmelzle, R. Intraoperative imaging of zygomaticomaxillary complex fractures using a 3D C-arm system. *International journal of oral and maxillofacial surgery* **34**, 369-375 (2005).

75   Townsend, D. W. *et al.* in *IEEE Symposium Conference Record Nuclear Science 2004.* 2383-2387 (IEEE).

76   Brasse, D. *et al.* in *2002 IEEE Nuclear Science Symposium Conference Record.* 951-955 (IEEE).

77   Ritman, E. L. Micro-computed tomography—current status and developments. *Annu. Rev. Biomed. Eng.* **6**, 185-208 (2004).

78   Badea, C. T., Fubara, B., Hedlund, L. W. & Johnson, G. A. 4-D micro-CT of the mouse heart. *Molecular Imaging* **4**, 15353500200504187 (2005).

79   Willekens, I. *et al.* Evaluation of the radiation dose in micro-CT with optimization of the scan protocol. *Contrast media & molecular imaging* **5**, 201-207 (2010).

80   Zhang, P., Li, L., Lin, L., Shi, J. & Wang, L. V. In vivo superresolution photoacoustic computed tomography by localization of single dyed droplets. *Light: Science & Applications* **8**, 36 (2019).

81   Xu, M. & Wang, L. V. Universal back-projection algorithm for photoacoustic computed tomography. *Physical Review E* **71**, 016706 (2005).

82   Dean-Ben, X. L., Buehler, A., Ntziachristos, V. & Razansky, D. Accurate model-based reconstruction algorithm for three-dimensional optoacoustic tomography. *IEEE Transactions on Medical Imaging* **31**, 1922-1928 (2012).

83   Deán-Ben, X. L., Ma, R., Rosenthal, A., Ntziachristos, V. & Razansky, D. Weighted model-based optoacoustic reconstruction in acoustic scattering media. *Physics in Medicine & Biology* **58**, 5555 (2013).

84   Ding, L., Deán-Ben, X. L., Lutzweiler, C., Razansky, D. & Ntziachristos, V. Efficient non-negative constrained model-based inversion in optoacoustic tomography. *Physics in Medicine & Biology* **60**, 6733 (2015).

85   Ding, L., Deán-Ben, X. L. & Razansky, D. Efficient 3-D model-based reconstruction scheme for arbitrary optoacoustic acquisition geometries. *IEEE transactions on medical imaging* **36**, 1858-1867 (2017).

86   Merčep, E., Herraiz, J. L., Deán-Ben, X. L. & Razansky, D. Transmission–reflection optoacoustic ultrasound (TROPUS) computed tomography of small animals. *Light: Science & Applications* **8**, 18 (2019).

87   Goldman, L. W. Principles of CT and CT technology. *Journal of nuclear medicine technology* **35**, 115-128 (2007).

88   Fehm, T. F., Deán-Ben, X. L., Ford, S. J. & Razansky, D. In vivo whole-body optoacoustic scanner with real-time volumetric imaging capacity. *Optica* **3**, 1153-1159 (2016).

89   Saxena, K. & Jolly, M. K. Acute vs. chronic vs. cyclic hypoxia: Their differential dynamics, molecular mechanisms, and effects on tumor progression. *Biomolecules* **9**, 339 (2019).

90   Hong, B.-J. *et al.* Tumor hypoxia and reoxygenation: the yin and yang for radiotherapy. *Radiation oncology journal* **34**, 239 (2016).

91   Horsman, M. R. & Overgaard, J. The impact of hypoxia and its modification of the outcome of radiotherapy. *Journal of radiation research* **57**, i90-i98 (2016).

92   Daneau, G., Boidot, R., Martinive, P. & Feron, O. Identification of cyclooxygenase-2 as a major actor of the transcriptomic adaptation of endothelial and tumor cells to cyclic hypoxia: effect on angiogenesis and metastases. *Clinical Cancer Research* **16**, 410-419 (2010).

93   Moeller, B. J., Cao, Y., Li, C. Y. & Dewhirst, M. W. Radiation activates HIF-1 to regulate vascular radiosensitivity in tumors: role of reoxygenation, free radicals, and stress granules. *Cancer cell* **5**, 429-441 (2004).

94   Matsumoto, S., Yasui, H., Mitchell, J. B. & Krishna, M. C. Imaging cycling tumor hypoxia. *Cancer research* **70**, 10019-10023 (2010).

95   Weissleder, R. & Nahrendorf, M. Advancing biomedical imaging. *Proceedings of the National Academy of Sciences* **112**, 14424-14428 (2015).

96   Kagadis, G. C., Ford, N. L., Karnabatidis, D. N. & Loudos, G. K. *Handbook of Small Animal Imaging: Preclinical Imaging, Therapy, and Applications*. (CRC Press, 2016).

97   Vasquez, K. O., Casavant, C. & Peterson, J. D. Quantitative whole body biodistribution of fluorescent-labeled agents by non-invasive tomographic imaging. *PloS one* **6**, e20594 (2011).

98   Conway, J. R., Carragher, N. O. & Timpson, P. Developments in preclinical cancer imaging: innovating the discovery of therapeutics. *Nature Reviews Cancer* **14**, 314 (2014).

99   Rastinehad, A. R. *et al.* Gold nanoshell-localized photothermal ablation of prostate tumors in a clinical pilot device study. *Proceedings of the National Academy of Sciences* **116**, 18590-18596 (2019).

100   Abadeer, N. S. & Murphy, C. J. Recent progress in cancer thermal therapy using gold nanoparticles. *The Journal of Physical Chemistry C* **120**, 4691-4716 (2016).

101   Khlebtsov, N. & Dykman, L. Biodistribution and toxicity of engineered gold nanoparticles: a review of in vitro and in vivo studies. *Chemical Society Reviews* **40**, 1647-1671 (2011).

102   Aide, N., Desmonts, C., Briand, M., Meryet-Figuiere, M. & Poulain, L. High-throughput small animal PET imaging in cancer research: evaluation of the capability of the Inveon scanner to image four mice simultaneously. *Nuclear medicine communications* **31**, 851-858 (2010).

103   Deán-Ben, X., Gottschalk, S., Mc Larney, B., Shoham, S. & Razansky, D. Advanced optoacoustic methods for multiscale imaging of in vivo dynamics. *Chemical Society Reviews* **46**, 2158-2198 (2017).

104   Basak, K., Luís Deán-Ben, X., Gottschalk, S., Reiss, M. & Razansky, D. Non-invasive determination of murine placental and foetal functional parameters with multispectral optoacoustic tomography. *Light: Science & Applications* **8**, 71, doi:10.1038/s41377-019-0181-7 (2019).

105   Ntziachristos, V. & Razansky, D. Molecular imaging by means of multispectral optoacoustic tomography (MSOT). *Chemical reviews* **110**, 2783-2794 (2010).

106   Li, L. *et al.* Single-impulse panoramic photoacoustic computed tomography of small-animal whole-body dynamics at high spatiotemporal resolution. *Nature biomedical engineering* **1**, 0071 (2017).

107   Van de Sompel, D., Sasportas, L. S., Jokerst, J. V. & Gambhir, S. S. Comparison of deconvolution filters for photoacoustic tomography. *PloS one* **11**, e0152597 (2016).

108   Ermilov, S. *et al.* Three-dimensional optoacoustic and laser-induced ultrasound tomography system for preclinical research in mice: design and phantom validation. *Ultrasonic imaging* **38**, 77-95 (2016).

109   Deán-Ben, X. L., Fehm, T. F., Ford, S. J., Gottschalk, S. & Razansky, D. Spiral volumetric optoacoustic tomography visualizes multi-scale dynamics in mice. *Light: Science & Applications* **6**, e16247 (2017).

110   Deán-Ben, X. L. & Razansky, D. Portable spherical array probe for volumetric real-time optoacoustic imaging at centimeter-scale depths. *Optics express* **21**, 28062-28071 (2013).

111   Rosenthal, A., Ntziachristos, V. & Razansky, D. Acoustic inversion in optoacoustic tomography: A review. *Current medical imaging reviews* **9**, 318-336 (2013).

112   Schambach, S. J., Bag, S., Groden, C., Schilling, L. & Brockmann, M. A. Vascular imaging in small rodents using micro-CT. *Methods* **50**, 26-35 (2010).

113   Kiessling, F., Pichler, B. & Hauff, P. in *Small Animal Imaging*   155-161 (Springer, 2017).

114   Özbek, A., Deán-Ben, X. L. & Razansky, D. Optoacoustic imaging at kilohertz volumetric frame rates. *Optica* **5**, 857-863, doi:10.1364/OPTICA.5.000857 (2018).

115   Ron, A., Davoudi, N., Deán-Ben, X. L. & Razansky, D. Self-Gated Respiratory Motion Rejection for Optoacoustic Tomography. *Applied Sciences* **9**, 2737 (2019).

116   Ford, N. L. *et al.* Prospective respiratory-gated micro-CT of free breathing rodents. *Medical physics* **32**, 2888-2898 (2005).

117   Schambach, S. J., Bag, S., Schilling, L., Groden, C. & Brockmann, M. A. Application of micro-CT in small animal imaging. *Methods* **50**, 2-13 (2010).

118   Su, R., Ermilov, S. A., Liopo, A. & Oraevsky, A. A. Three-dimensional optoacoustic imaging as a new noninvasive technique to study long-term biodistribution of optical contrast agents in small animal models. *Journal of biomedical optics* **17**, 101506 (2012).

119   Wang, J. *et al.* In vivo pharmacokinetic features and biodistribution of star and rod shaped gold nanoparticles by multispectral optoacoustic tomography. *RSC Advances* **5**, 7529-7538 (2015).

120   Egusquiaguirre, S. P. *et al.* Optoacoustic imaging enabled biodistribution study of cationic polymeric biodegradable nanoparticles. *Contrast media & molecular imaging* **10**, 421-427 (2015).

121   Cheheltani, R. *et al.* Tunable, biodegradable gold nanoparticles as contrast agents for computed tomography and photoacoustic imaging. *Biomaterials* **102**, 87-97 (2016).

122   Song, W. *et al.* Comprehensive studies of pharmacokinetics and biodistribution of indocyanine green and liposomal indocyanine green by multispectral optoacoustic tomography. *RSC Advances* **5**, 3807-3813 (2015).

123   Ron, A., Deán-Ben, X. L., Reber, J., Ntziachristos, V. & Razansky, D. Characterization of Brown Adipose Tissue in a Diabetic Mouse Model with Spiral Volumetric Optoacoustic Tomography. *Molecular Imaging and Biology*, doi:10.1007/s11307-018-1291-y (2018).

124   Chen, Y.-S. *et al.* Enhanced thermal stability of silica-coated gold nanorods for photoacoustic imaging and image-guided therapy. *Optics express* **18**, 8867-8878 (2010).

Publishers' letters of approval

All articles published by MDPI are made immediately available worldwide under an open access license. This means:

![MDPI logo](/)

- everyone has free and unlimited access to the full-text of *all* articles published in MDPI journals;
- everyone is free to re-use the published material if proper accreditation/citation of the original publication is given;
- open access publication is supported by the authors' institutes or research funding agencies by payment of a comparatively low **Article Processing Charge (APC) (/about/apc)** for accepted articles.

Permissions

No special permission is required to reuse all or part of article published by MDPI, including figures and tables. For articles published under an open access Creative Common CC BY license, any part of the article may be reused without permission provided that the original article is clearly cited. Reuse of an article does not imply endorsement by the authors or MDPI.

External Open Access Resources

MDPI is a RoMEO **green publisher (http://www.sherpa.ac.uk/romeo/search.php?type=publisher&search=mdpi)** — RoMEO is a database of Publishers' copyright and self-archiving policies hosted by the **University of Nottingham (http://www.nottingham.ac.uk/)**

Those who are new to the concept of open access might find the following websites or 'Open Access 101' video informative:

Wikipedia article on 'Open Access' (https://en.wikipedia.org/wiki/Open_access_(publishing))
Peter Suber's 'Open Access Overview' (http://www.earlham.edu/~peters/fos/overview.htm)
Information Platform Open Access [in **English (http://open-access.net/de_en/)**, in **German (http://open-access.net/de/)**]
SHERPA's 'Authors and Open Access' (http://www.sherpa.ac.uk/guidance/authors.html)

Meaning of Open Access

In accordance with major definitions of open access in scientific literature (namely the Budapest, Berlin, and Bethesda declarations), MDPI defines *open access* by the following conditions:

- peer-reviewed literature is freely available without subscription or price barriers,

Open Access Explained!

Copyright Clearance Center

RightsLink®

Home

?
Help

Email Support

Avihai Ron ⌄

Characterization of Brown Adipose Tissue in a Diabetic Mouse Model with Spiral Volumetric Optoacoustic Tomography

SPRINGER NATURE

Author: Avihai Ron et al

Publication: Molecular Imaging and Biology

Publisher: Springer Nature

Date: Nov 1, 2018

Copyright © 2018, Springer Nature

Order Completed

Thank you for your order.

This Agreement between None -- Avihai Ron ("You") and Springer Nature ("Springer Nature") consists of your license details and the terms and conditions provided by Springer Nature and Copyright Clearance Center.

Your confirmation email will contain your order number for future reference.

License Number	4876481083989
License date	Jul 26, 2020

🖶 Printable Details

✔ Licensed Content

Licensed Content Publisher	Springer Nature
Licensed Content Publication	Molecular Imaging and Biology
Licensed Content Title	Characterization of Brown Adipose Tissue in a Diabetic Mouse Model with Spiral Volumetric Optoacoustic Tomography
Licensed Content Author	Avihai Ron et al
Licensed Content Date	Nov 1, 2018

📋 Order Details

Type of Use	Thesis/Dissertation
Requestor type	academic/university or research institute
Format	print and electronic
Portion	full article/chapter
Will you be translating?	no
Circulation/distribution	50000 or greater
Author of this Springer Nature content	yes

📄 About Your Work

Title	PhD candidate
Institution name	TUM
Expected presentation date	Aug 2020

📁 Additional Data

Requestor Location

Requestor Location
None
Sandstraße
49
Haus A
München, 80335
Germany
Attn: None

Tax Details

Price

Total   0.00 EUR

Total: 0.00 EUR

CLOSE WINDOW   ORDER MORE

Volumetric Optoacoustic Imaging Unveils High-Resolution Patterns of Acute and Cyclic Hypoxia in a Murine Model of Breast Cancer

Author: Avihai Ron,Xosé Luís Deán-Ben,Sven Gottschalk,Daniel Razansky

Publication: Cancer Research

Publisher: American Association for Cancer Research

Date: 2019-09-15

Copyright © 2019, American Association for Cancer Research

Permission Request

This reuse request is free of charge and you are not required to obtain a license.

BACK   CLOSE WINDOW